THE UNIVERSITY OF CHICAGO

PHYSICS AND MATERIAL SCIENCE OF ULTRA-HIGH QUALITY FACTOR SUPERCONDUCTING RESONATOR

A DISSERTATION SUBMITTED TO
THE FACULTY OF THE DIVISION OF THE PHYSICAL SCIENCES
IN CANDIDACY FOR THE DEGREE OF
DOCTOR OF PHILOSOPHY

DEPARTMENT OF PHYSICS

BY
ALEXANDER VOSTRIKOV

CHICAGO, ILLINOIS
AUGUST 2015

To my wife and my mother

CONTENTS

LIST OF FIGURES

LIST OF TABLES

ACKNOWLEDGMENTS

First of all, I would like to thank many people who helped me to complete this thesis work.

I am greatly indebted to my research adviser at Fermilab and a very good friend Dr. Alexander Romanenko who helped me to choose the direction of the research and guided through the complications and problems arose to the successful results. His invaluable support in resolving any issues during the work let me complete the thesis project.

I wish to express my sincere thanks to Prof. Young-Kee Kim, my academic advisor, for the support during completion the thesis project, for organizing the collaboration with Fermilab to provide with necessary access to the facilities for the research. Sharing her expertise and permanent attention to the progress of my research allowed me to perform the work in timely manner.

I thank Dr. Slava Yakovlev and Dr. Nikolay Solyak, scientists at Fermilab, for their positive influence on my entire scientific career path. Separately, I want to thank them for help and support of high order mode impact analysis research.

I would like to thank the members of my Ph.D. thesis committee: Prof. Steven Sibener, Prof. David Schuster and Prof. Emil Martinec for tracking the progress of my research during last two years and reading this document. I want to thank again my advisors Prof. Young-Kee Kin and Dr. Alexander Romanenko for providing a valuable feedback on my writing.

I want to thank Dr. Alexander Sukhanov and Andrei Lunin for the valuable discussions on some aspects of this work.

I thank SRF group at Fermilab including Dr. Alex Melnychuk, Dr. Anna Grassellino, Dr. Sam Posen, Mattia Checchin for training to test SRF cavities, help with day to day problems and continuous encouragement.

I thank Robert Schuessler for assistance with niobium sample preparation for the magnetometer measurements and for the technical support of the magnetometer. Margherita Merio who performed nitrogen doping on niobium samples.

I thank my friend Dr. Andrey Elagin for the permanent faith in my final success.

I thank my friend Dr. Mikhail Goykhman for his help with some theoretical aspects of this work.

I sincerely thank my wife and closest friend Olya for her patience and invaluable support during the whole time of my studying.

ABSTRACT

The nitrogen doping into niobium superconducting radio frequency cavity walls aiming to improve the fundamental mode quality factor is the subject of the research in the given work. Quantitative nitrogen diffusion into niobium model calculating the concentration profile was developed. The model estimations were confirmed with secondary ion mass spectrometry technique measurements. The model made controlled nitrogen doping recipe optimization possible. As a result the robust reproducible recipe for SRF cavity walls treatment with nitrogen doping was developed. The cavities produced with optimized recipe met LCLS–II requirements on quality factor of $2.7 \cdot 10^{10}$ at acceleration field of 16 MV/m.

The microscopic effects of nitrogen doping on superconducting niobium properties were studied with low energy muon spin rotation technique and magnetometer measurements. No significant effect of nitrogen on the following features was found: electron mean free path, magnetic field penetration depth, and upper and surface critical magnetic fields. It was detected that for nitrogen doped niobium samples magnetic flux starts to penetrate inside the superconductor at lower external magnetic field value compared to the low temperature baked niobium ones. This explains lower quench field of SRF cavities treated with nitrogen.

Quality factor improvement of fundamental mode forced to analyze the high order mode (HOM) impact on the particle beam dynamics. Both resonant and cumulative effects caused by monopole and dipole HOMs respectively are found to be negligible within the requirements for LCLS–II.

CHAPTER 1

INTRODUCTION

1.1 Importance of particle accelerators

1.1.1 Particle physics

Three "elementary" particles: the electron, the proton and the neutron — had been discovered in the beginning of twentieth century. It was assumed that all matter consists of these particles, and all effects in physics could be explained in terms of these constituents. Notwithstanding, the simple model including just these three particles was found unable to explain a number of effects within a few decades. By the middle of the century a myriad of new "elementary" particles were discovered that threatened to be very confusing. Being driven by a desire to find an underlying simplicity, researchers expended much effort to explain the multitude of particles in terms of even more fundamental "building blocks." This endeavor culminated in the development of the "Standard Model." According to this model, all matter consists of

- six "flavors" of quarks arranged in three generations of two,
- six leptons (also in three generations),
- an equal number of antiparticles,
- gauge bosons W^+, W^- and Z^0 mediating weak interaction,
- a photon which mediates electric interaction,
- gluons mediating strong interaction between quarks,
- a Higgs boson which explains why some particles have mass when, based on the symmetries controlling their interactions, they should be massless.

By combining quarks of different flavors, all mesons and baryons known to date can be explained.

It is impossible to overestimate the role of the particle accelerators in discovering the new particles. The standard way to produce a new particle is to collide two known particles. The higher the energy of the colliding particles the more variety of outcomes allowed in the final state. Particle accelerators are vital in this process as the only way to produce a directed particle beam of high energy.

Past and current particle accelerators have proved pivotal in providing the experimental evidence that vindicates the Standard Model, which now is accepted as one of this century's great successes. For example, in 1983, researchers at the European Organization for Nuclear Research (CERN) [21] proved the existence of the W^+, W^- and Z^0 particles, three of the four carriers of the electroweak force. The photon is the fourth carrier. In 1995 it was the postulated sixth quark (the "top") discovered at Fermilab [23], to complete the three generations of quarks. And only as recently as 2014 the Higgs boson responsible for the mass of the particles was discovered at Large Hadron Collider (LHC) [24] at CERN.

1.1.2 Light sources

Successful development of particle accelerators during last century led to their application to light sources. Accelerated high-energy electron beam of very good quality can be directed through special arrangements of magnets (undulators), such that charged particles move along a curved trajectory. In result the electrons emit radiation that is increasingly amplified until an extremely short and intense X-ray flash crated.

Proposed future accelerator facilities such as European X-ray Free Electrom Laser (XFEL) [22] and Linac Coherence Light Source II (LCLS–II) [6] will generate X-ray radiation with properties similar to laser light. Each of the facilities will have several light sources with different characteristics. LCLS–II is described in details in Section 1.2.3.

Both of the facilities are examples of a new generation of particle accelerators: European

XFEL is under construction in Germany, LCLS–II is going to be built at Stanford Linear Accelerator Center (SLAC) National Accelerator Laboratory in California, USA. For the scientific society to be able to build and operate these research facilities, it is necessary to understand the physics of accelerator components and the ways for their optimization.

1.2 Superconducting radio frequency cavities

The primary purpose of a particle accelerator is to transfer electric power into the energy of charged particles beam. Cavities are the devices used to provide energy to the particles that are crucial to an accelerator. Most commonly used are radio frequency (RF) cavities, an example of which is shown in Figure 1.1.

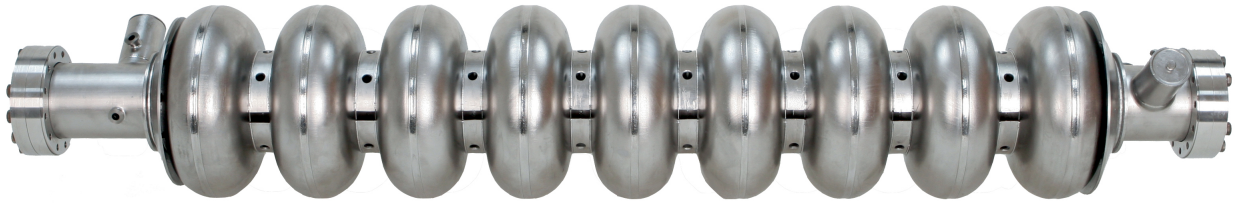

Figure 1.1: An image of an actual TESLA-type niobium superconducting radio frequency cavity. TESLA-type cavity consists of nine cells. Fundamental mode frequency is 1.3 GHz.

In the past, copper cavities were used for acceleration (e. g., at SLAC [25]). However, superconducting niobium and lead technology has proven itself over the last ten years as a promising alternative, being used in machines such as Hadron Elektron Ring Anlage (HERA) in Hamburg, Germany and Thomas Jefferson National Accelerator Facility (TJNAF) in Newport News, VA, USA. Continuous wave (CW) accelerating gradients of 10 MV/m have been achieved, exceeding levels that are possible with copper cavities. These days SRF cavity gradients can reach up to 40 MV/m. Many of the current and the future projects (among them KEK B-factory, the LHC, and the LCLS–II) are relying on superconducting cavities to achieve their design goals. Thus, superconductors will play a pioneering role at both the energy frontier and the high current frontier. In some very imaginative and novel designs (for example multi-TeV $\mu^+\mu^-$ colliders), SRF is completely indispensable,

illustrating that this technology holds the key for the next generation of particle accelerators and perhaps even beyond. Extensive research has therefore been performed to understand the performance limitations of superconducting cavities and to improve upon the achieved accelerating gradients. The work presented here is similarly motivated.

1.2.1 Advantages of superconducting cavities

Although not completely loss free above $T = 0$ K, as in the DC case, superconducting cavities dissipate orders of magnitude less power than normal conducting cavities. Niobium cavities, like those installed at TJNAF, routinely achieve quality (Q_0) factors 10^5 to 10^6 times that of copper cavities. The dramatically reduced resistivity translates into a number of very important advantages. They include:

1. Operating cost savings. Even when taking into account the cost of refrigerating superconducting cavities, their power demand in cw applications is more than two orders of magnitude less than that of equivalent copper cavities.

2. Capital cost savings. The reduced power requirements translate into capital cost savings, since fewer (and sometimes simpler) klystrons are needed.

3. High gradient. The reduced power consumption also enables superconducting cavities to operate at high cw gradients.

4. Reduced impedance. The aperture of superconducting cavities is large, thereby minimizing disruptive interactions of the cavity with the beam (characterized by the impedance). Higher currents can therefore be accelerated. This fact is the main motivation for using SRF technology in high current machines such as CESR.

1.2.2 Cavity performance limitations

A limit on the maximum accelerating gradient of superconducting cavities is imposed by the superheating magnetic field. At no point of the cavity surface may the magnetic field exceed the superheating field, otherwise the superconductor goes normal conducting ("quenches"). Niobium cavities of the shape used in our test are therefore limited to an accelerating gradient of about 50 MV/m.

For a number of reasons, though, such high accelerating gradients are never achieved in practical cavities. The most common limiting mechanisms are field emission, thermal breakdown, and, at times, multipacting.

Field emission is the primary mechanism that limits present day cavities to accelerating gradients below 45 MV/m. In the presence of a high surface electric field, RF power is lost to electrons that tunnel out of the cavity wall at very localized points. The emitted electrons are accelerated by the electromagnetic fields and, upon impact, heat the cavity wall and produce X-rays. Field emission scales exponentially with the electric field and is capable of consuming inordinate amounts of power.

Thermal breakdown generally results when a highly resistive defect on the RF surface causes a large fraction of the cavity to quench. An abrupt reduction of the cavity quality results. Thermal breakdown can also be initiated by the heat from bombarding field emission electrons.

Multipacting is a resonant process, in which a large number of electrons build up an avalanche by repeated impact with the cavity walls. Again, the heat deposited by these impacts can lead to thermal breakdown. In the absence of thermal breakdown, the absorption of RF power by multipacting electrons can still make it impossible to raise the cavity fields.

Even at low field levels (below an accelerating gradient of a few MV/m) all cavities display losses higher than theoretically expected. The anomalous losses are attributed to a temperature independent residual resistance. The dominant sources for this resistance are impurities on the RF surface, adsorbed gases, and residual magnetic flux that is trapped in

the superconductor as it is cooled through the transition temperature. In some cases the precipitation of niobium hydride at the RF surface due to hydrogen stored in the wall may also contribute to the residual resistance. This phenomenon is known as the "Q-virus", and it can be avoided by driving out the hydrogen during a vacuum bake of the cavity at 800°.

1.2.3 Linac Coherence Light Source II

The Linac Coherent Light Source (LCLS) [5] is the most powerful X-ray laser in the world built in SLAC National Accelerator Laboratory [25]. LCLS–II [6] is a proposed upgrade, which will add two new X-ray laser beams. When complete, LCLS-II will provide soft coherent X-ray radiation for a broad spectrum of basic research applications. Multiple free electron laser (FEL) sections will be powered by CW SRF electron linac. The linac design is based on the technology developed for International Linear Collider (ILC) [4]. It represents standard ILC structure (TESLA-type 9-cell 1.3 GHz cavities grouped in cryomodules) with modified high order mode (HOM) coupler to reduce heating because of the fundamental mode. A schematic layout of LCLS–II injector, linac, bunch compressor and beam transport with key parameters listed for CW operation with 100 pC per bunch is shown in Figure 1.2.

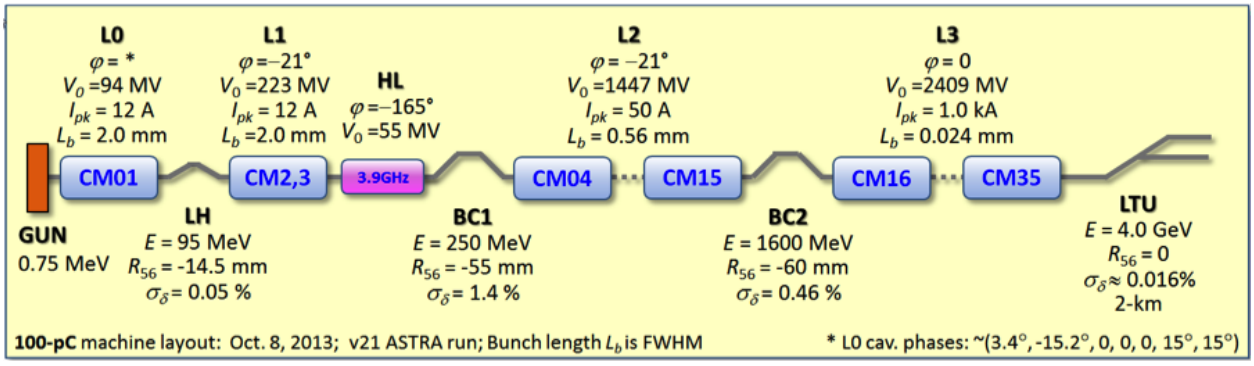

Figure 1.2: Schematic layout of LCLS–II injector, linac, bunch compressors and beam transport with key parameters listed for CW operation with 100 pC per bunch.

A superconducting radio frequency (SRF) cavity is a chamber made of a superconducting metal with electromagnetic field inside. The most common fabrication material for modern SRF cavities is high purity niobium. The choice of material is determined by niobium rigid

properties and relatively high critical temperature (T_c = 9.25 K). Rigidity of niobium is required to minimize cavity deformation due to its own weight. Critical temperature of 9.25 K allows niobium to function nicely in a liquid helium bath of 4.2 K and lower.

The primary purpose of SRF cavities is to accelerate charged particles. To do so specific electromagnetic field needs to be created inside the cavity. RF power generator supplies the electromagnetic field. The design of SRF cavity assumes specific shape and size, so that electromagnetic waves become resonant and build up inside the cavity. The frequencies of resonant electromagnetic waves are eigenmodes of the cavity. Each cavity in an accelerator is tuned to oscillate at specific frequency, i. e. only one specific mode is intentionally excited in each cavity. This mode and its frequency is called fundamental. SRF niobium 9-cell TESLA-type cavities described in Section 2.2.2 are considered in the present research.

1.3 Organization of the dissertation

SRF cavity fundamentals and basics of superconductivity are summarized in Chapter 2. Nitrogen doping optimization towards achieving ultra-high quality factor is discussed in Chapter 3. The measurements of microscopic superconducting properties of niobium treated with nitrogen doping using low energy muon spectroscopy and magnetometer are presented in Chapters 4 and 5 correspondingly. High order mode impact on the particle beam dynamics in LCLS–II analysis can be found in Chapter 6. Interpretation of the results is discussed in Chapter 7. The summary of the thesis is presented in Chapter 8.

CHAPTER 2

CAVITY FUNDAMENTALS

2.1 Introduction

In this chapter a summary of SRF cavities focusing on niobium ones is presented. At the beginning the electrodynamics of radio frequency (RF) cavities is discussed, the power dissipation is described. The information presented in this section is valid for both normal conducting and superconducting cavities.

In the second section the first principles of superconductivity are introduced. The fundamental limitation on magnetic field of SRF cavities is explained. In addition, it is demonstrated why the power dissipation in SRF cavities exists in spite of superconductors can carry DC currents without losses.

This chapter should not be considered as a complete overview of SRF cavity theory, but primary principles important for understanding of the dissertation are covered. In depth review of the superconductivity and SRF cavity theory in particular can be found in the following texts: [13, 28, 29, 32].

2.2 Electrodynamics

2.2.1 Cavity electromagnetic fields

Electromagnetic field excited in an RF cavity satisfies the wave equations derived from the combination of Maxwell's equations [13]:

$$\begin{aligned} \nabla^2 \vec{E} &= \frac{1}{c^2} \frac{\partial^2 \vec{E}}{\partial t}, \\ \nabla^2 \vec{H} &= \frac{1}{c^2} \frac{\partial^2 \vec{H}}{\partial t}, \end{aligned} \tag{2.1}$$

where $\vec{E}$ is the electric field vector and $\vec{H}$ is the magnetic field vector. The following boundary conditions at the surface of the cavity walls should be taken into account:

$$\begin{aligned} \vec{n} \times \vec{E} &= \vec{0}, \\ \vec{n} \cdot \vec{H} &= 0. \end{aligned} \tag{2.2}$$

Vector $\vec{n}$ is normal to the surface of the cavity and $|\vec{n}| = 1$.

There are two types of modes (solutions of Equation (2.1)) for the cavities with axial symmetry: transverse electric (TE) and transverse magnetic (TM) modes. For these types of modes corresponding field is transverse to the cavity axis. Particle acceleration happens due to TM modes as their electric component is directed along the beam axis, which leads to acceleration of charged particles. TM modes are also called monopole modes, while TE modes are called dipole modes.

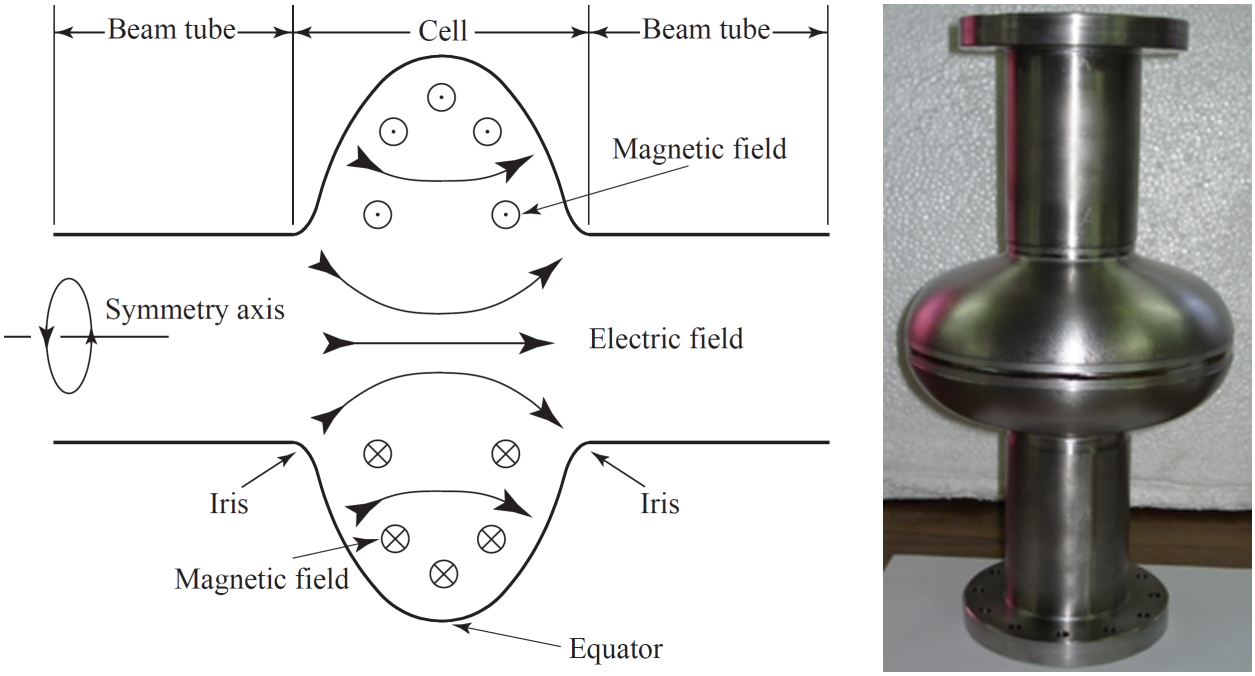

(a) (b)

Figure 2.1: Elliptical shaped one-cell SRF cavity. The schematic plot is shown in Figure 2.1a. An image of an actual niobium cavity is shown in Figure 2.1b.

TM modes can be classified as TM_{mnp}, where m, n and p are integer numbers. These numbers represent the number of longitudinal component of electric field E_z sign changes in the angular (ϕ), radial (r) and longitudinal (z) directions. TE modes are classified the same way. Only TM modes with $m = 0$ have a non-vanishing longitudinal electric field component on the cavity axis, that is why TM_{010} mode is usually used for the particle acceleration and called accelerating or fundamental mode. This mode is intentionally excited in the cavity to transfer energy to the beam, while excitation of other modes should be avoided or minimized.

Elliptical shaped SRF cavities are used instead of a regular pillbox shape due to practical reasons [29]. A schematic example of a one-cell SRF cavity is shown in Figure 2.1a. An image of an actual niobium cavity is shown in Figure 2.1b. The electric field of the fundamental mode concentrated at the irises and near the axis, while the magnetic field concentration is larger at the equator of the cavity. An example of electric and magnetic fields distribution in one-cell cavity is shown in Figure 2.2. Due to complexity of the cavity shape only numerical calculations of the fields are possible. For example, codes SuperLANS [17], SuperLANS2 [18], CLANS [17], CLANS2 [19] or CST Microwave Studio [20] can be used for such calculations.

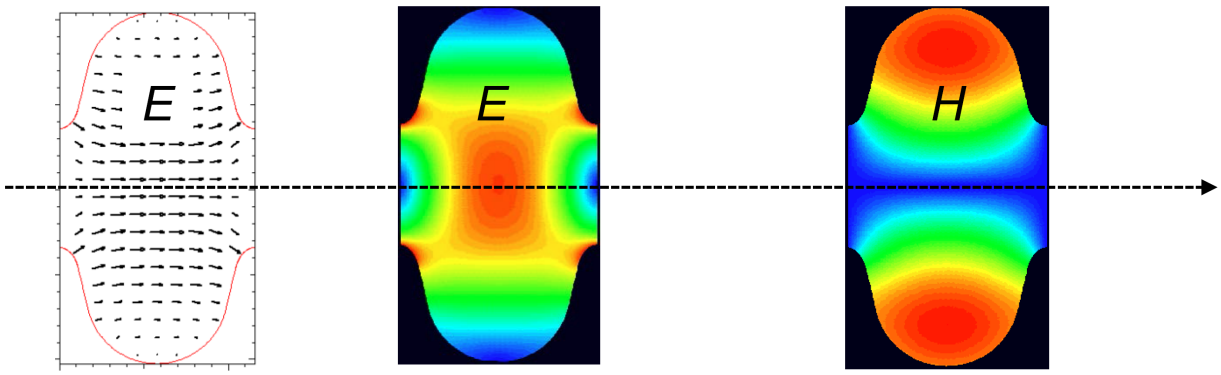

Figure 2.2: An example of electric and magnetic field distribution for one-cell elliptical SRF cavity.

2.2.2 TESLA cavity design

SRF cavity design developed by the TESLA (Tera–Electronvolt Energy Superconducting Linear Accelerator) Technology Collaboration [27] is widely used these days (see Figure 1.1). The cavity is made of bulk niobium with grain size of about 50 μm and residual resistivity ratio (RRR) of about 300. It is operating in TM_{010} mode. The frequency of the fundamental mode is about 1.3 GHz. The elliptical cavity geometry is shown in Figure 2.3. Geometry parameters are listed in Table 2.1). This type of cavity has nine cells, each consists of two half-cells (18 half-cells total). All 16 inner half-cells are identical and called regular half-cells. Left and right half-cells are different from the regular half-cells and each other. That makes the cavity asymmetric.

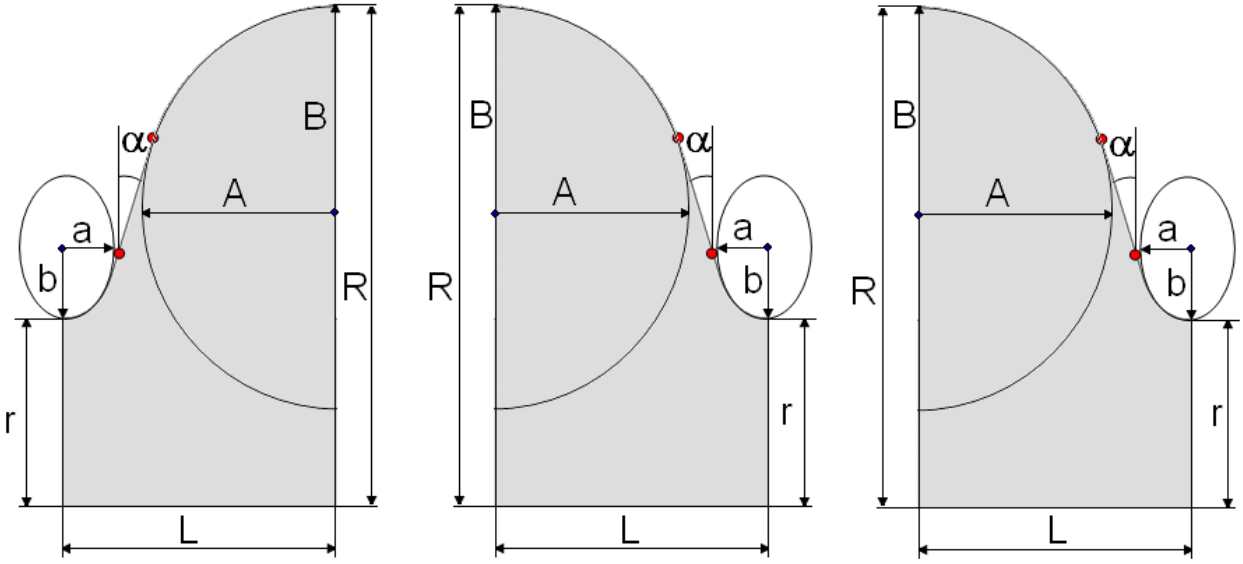

Figure 2.3: TESLA 9-cell 1.3 GHz elliptical cavity geometry. The cavity is asymmetric. It consists of identical intrinsic half-cells, but left and right half-cells are different. Left cell geometry is shown on the left, right cell geometry is shown on the right, regular cell geometry is shown in the middle. Geometry parameters can be found in Table 2.1.

Table 2.1: Geometry parameters for TESLA 9-cell 1.3 GHz elliptical cavity (see Figure 2.3).

Dimension	Left half-cell	Regular half-cell	Right half-cell
r, mm	39	35	39
R, mm	103.3	103.3	103.3
L, mm	55.7	57.692	56.84
A, mm	40.34	42	42
B, mm	40.34	42	42
a, mm	10	12	9
b, mm	13.5	19	12.8
α, deg	16.0	13.3	17.4

2.2.3 Multi-cell SRF cavities

Typically multi-cell cavities are used in actual particle accelerators. TELSA-type SRF cavity design is described in Section 2.2.2. In a multi-cell cavity the spectrum of the modes (both TM and TE) splits by the number of cells. Thus each mode in the spectrum of a cell of a TESLA-type cavity corresponds to a passband of nine modes in the spectrum of whole cavity. The examples of electric field distributions of two monopole modes from the same passband inside the cavity are shown on Figures 2.4 and 2.5 [37].

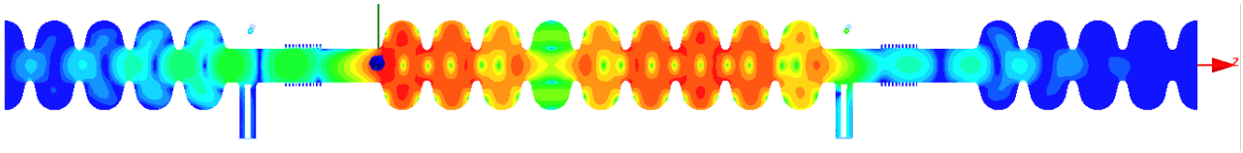

Figure 2.4: Electric field distribution for the mode #8 in the second monopole passband of the 1.3 GHz TESLA-type cavity. Mode frequency is 2.452 GHz, effective impedance R/Q is 136 Ω.

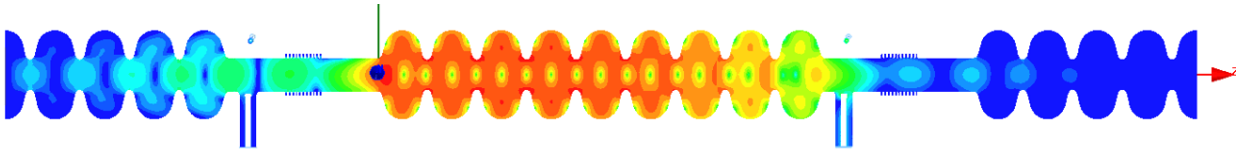

Figure 2.5: Electric field distribution for the mode #9 in the second monopole passband of the 1.3 GHz TESLA-type cavity. Mode frequency is 2.458 GHz, effective impedance R/Q is 157 Ω.

2.2.4 Accelerating field

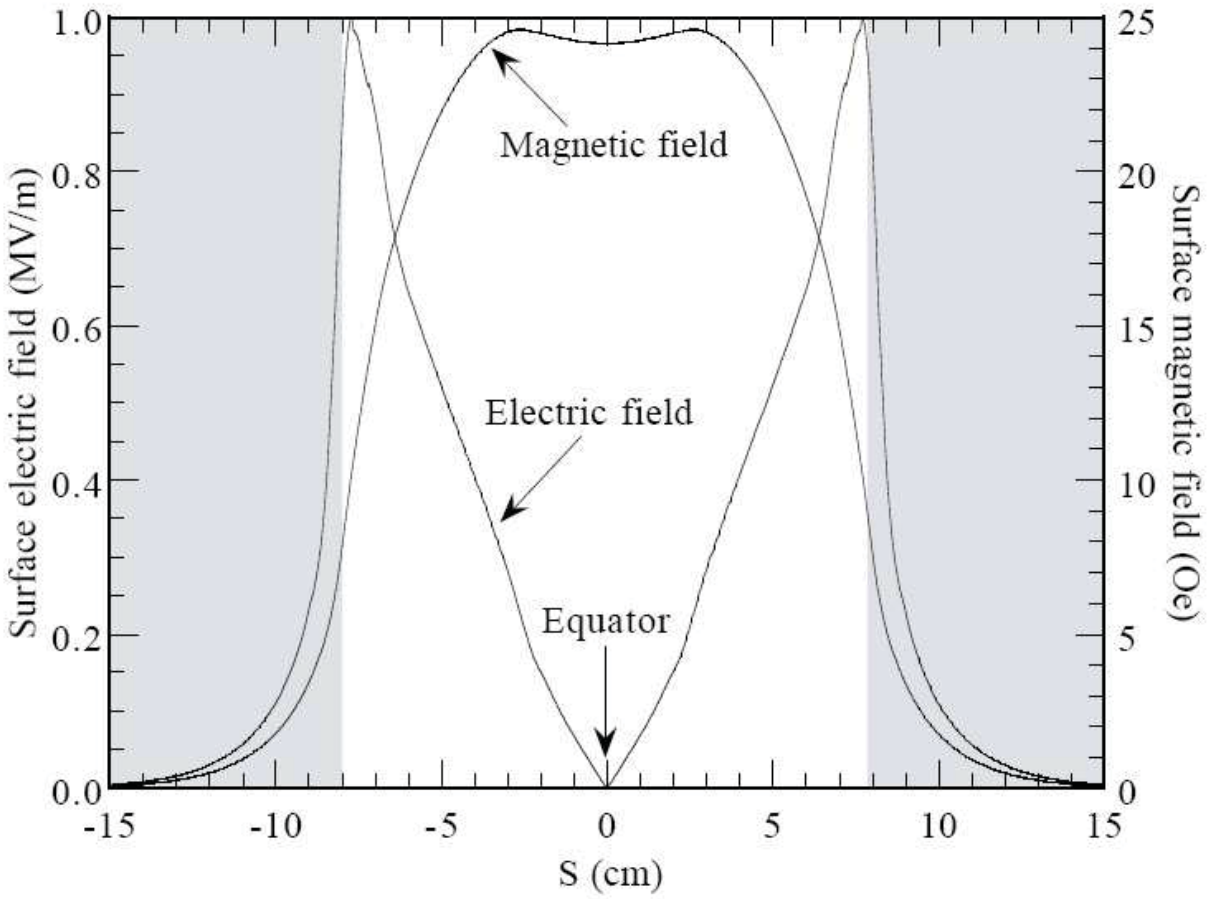

Figure 2.6: Surface electric and magnetic field distribution along the length of the cell of TESLA-type SRF 1.3 GHz cavity.

By definition the accelerating voltage V_{acc} of a cavity is the ration of the maximum energy gain possible during the transit of a charged particle through the cavity along its axis over the charge of the particle. For the case when particles move with a speed close to the speed of light through the cavity, the acceleration voltage can be given by the following equation:

$$V_{\mathrm{acc}} = \left| \int_0^L E_z(r=0,z) e^{i\omega_0 z/c} \mathrm{d}z \right|, \tag{2.3}$$

where L is cavity length and ω_0 is angular frequency of the fundamental mode. More often, to describe the cavity performance the accelerating field E_{acc} is used instead of the accelerating

voltage:

$$E_{\text{acc}} = \frac{V_{\text{acc}}}{d}. \tag{2.4}$$

For given cavity geometry surface magnetic field is close to its peak value B_{peak} on the majority of the cavity surface. Magnetic field peak value is proportional to the accelerating gradient E_{acc} and for this geometry

$$\frac{B_{\text{peak}}}{E_{\text{acc}}} = 4.26 \ \frac{\text{mT}}{\text{MV/m}}. \tag{2.5}$$

2.2.5 Dissipation power

The surface resistance R_S of a cavity is defined as measure of the dissipated power per unit area such as

$$\frac{\mathrm{d}P}{\mathrm{d}S} = \frac{1}{2} R_S \left|\vec{H}\right|^2, \tag{2.6}$$

where $\vec{H}$ is surface magnetic field. When there is electromagnetic field inside the cavity, currents flow in the cavity walls. Typically the dissipated power is characterized by the quality factor Q_0, which is proportional to the ratio of the energy stored in the cavity W over the dissipated power:

$$Q_0 = \frac{\omega_0 W}{P}. \tag{2.7}$$

Q_0 represents 2π times the number of RF cycles necessary to dissipate all stored energy.

The energy stored in the cavity can be determined as the following integral over the volume of the cavity:

$$W = \frac{\mu_0}{2} \int_V |\vec{H}|^2 \mathrm{d}V. \tag{2.8}$$

Equation (2.6) allows us to calculate the dissipation power as an integral over the interior surface of the cavity:

$$P = \frac{1}{2} \int_S R_S |\vec{H}|^2 \mathrm{d}S. \tag{2.9}$$

Applying the Equations (2.8) and (2.9) to the definition of the quality factor (2.7), the

quality factor of the cavity can be calculated as

$$Q_0 = \frac{\mu_0 \omega_0 \int_V |\vec{H}|^2 \mathrm{d}V}{\int_S R_S |\vec{H}|^2 \mathrm{d}S}. \tag{2.10}$$

The ratio

$$G = \frac{\mu_0 \omega_0 \int_V |\vec{H}|^2 \mathrm{d}V}{\int_S |\vec{H}|^2 \mathrm{d}S} \tag{2.11}$$

depends on the cavity material and shape only, that is why it is called a geometry factor. Introducing the average surface resistance as

$$\bar{R}_S = \frac{\int_S R_S |\vec{H}|^2 \mathrm{d}S}{\int_S |\vec{H}|^2 \mathrm{d}S} \tag{2.12}$$

the quality factor can be expressed as

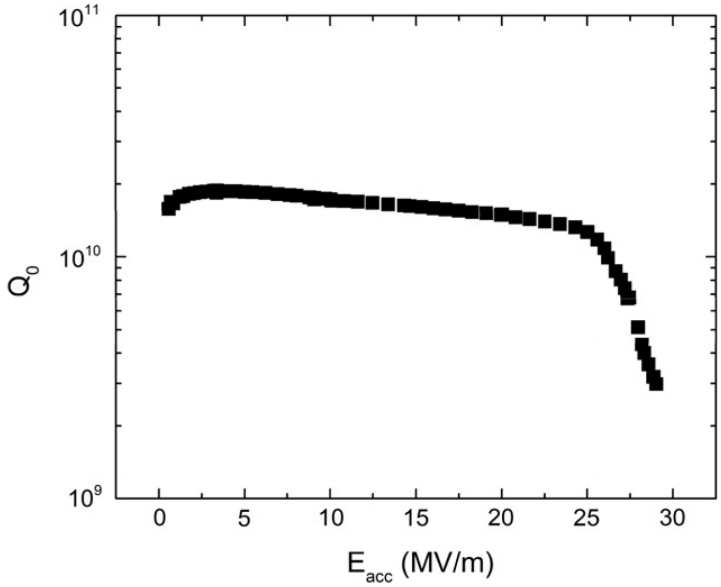

Figure 2.7: An example of excitation curve (Q_0 versus E_{acc}) for SRF cavity. This curve is used to describe the performance of SRF cavity.

$$Q_0 = \frac{G}{\bar{R}_S}. \tag{2.13}$$

The quality factor and the accelerating voltage are important figures of merit describing the performance of the cavity. Overall performance of the cavity is typically described with the excitation curve (for example, see Figure 2.7). Target performance for the LCLS–II is $Q_0 = 2.7 \cdot 10^{10}$ at $E_{\mathrm{acc}} = 16$ MV/m and temperature of 2 K. Traditional state of art technology of cavity preparation allows to reach the quality factor of $1 - 2 \cdot 10^{10}$ at given conditions. This is extremely large value, one of the largest quality factor in the nature, but current needs in experimental physics requires to push the limits even further. Geometry

factor for the nine-cell TESLA-type cavity (Figures 1.1 and 2.3) is 270 Ω, which means that systematic SRF cavity production with surface resistance below 10 nΩ is needed to meet LCLS–II requirements.

2.3 Superconductivity

The discussion so far applies equally well to both normal and superconducting cavities. However, to understand the behavior of superconducting cavities some knowledge of superconductivity is required. Numerous texts have been written about this subject as applied to SRF cavities [28], [29]. We will therefore concentrate on the salient aspects that pertain to the experimental results reported here.

2.3.1 Theory of superconductivity

It is well known that superconductors lose their dc resistivity completely below a critical temperature T_c. Of all the elements, niobium has the highest critical temperature with $T_c = 9.25$ K. The mechanism responsible for this fascinating behavior is complex but was successfully explained by Bardeen, Cooper, and Schrieffer (BCS) in 1957 [1].

According to the BCS theory, it is energetically favorable for electrons in superconductors to pair off as so-called "Cooper pairs" to yield a bosonic pseudo–particle. This pairing process is assisted by phonons. Each pair consists of two electrons of opposite momentum and spin. The temperature dependent pairing energy $\Delta(T)$ (per electron) is responsible for creating an energy gap in the electronic spectrum between the bosonic ground state and the energy levels of the unpaired fermionic electrons. $\Delta(T = 0)$ is fairly small, on the order of a few meV.

Although the paired state is energetically favorable below T_c, not all electrons are in the bosonic ground state when $0 < T < T_c$, because there is a finite probability that some pairs are split by thermal excitations. The probability is governed by the Boltzmann factor

$\exp[-\Delta(T)/(k_B T)]$, k_B being the Boltzmann constant. Below $T = T_c/2$ the Cooper pair density $n_s(T)$ is close to $n_s(T = 0)$, and the number of unpaired electrons is given by

$$n_e \approx 2n_s(T = 0) \exp\left[-\frac{\Delta(T)}{k_B T}\right]. \tag{2.14}$$

In this temperature range the energy gap $\Delta(T)$ is also close to its zero temperature value. The BCS theory predicts that $\Delta(T = 0) = \alpha k_B T_c$, $\alpha \approx 1.76$. Hence,

$$n_e \approx 2n_s(T = 0) \exp\left(-\alpha \frac{T_c}{T}\right). \tag{2.15}$$

2.3.2 Superconductor surface resistance

Although superconductors do not exhibit any DC resistivity, there are small losses for RF currents. This fact can be explained by a model of inter-penetrating normal conducting electrons and superconducting Cooper pairs when $T > 0$ (two fluid model). Collisions between Cooper pairs and lattice defects, impurities, or phonons are insufficient to split the pairs and scatter them out of the ground state. Hence, any current carried by these pairs flows without resistance. On the other hand, the unpaired electrons can be scattered and dissipate energy. Nevertheless, the dc resistivity of a superconductor is zero because the lossless Cooper pair current "shorts out" any fields in the superconductor. The normal conducting electrons never see an electric field and do not contribute to the current flow.

In the RF case the situation is different. Although Cooper pairs cannot be scattered, they do possess inertia. At microwave frequencies, they no longer screen externally applied fields completely and normal conducting electrons are accelerated. This component of the electron fluid then causes power dissipation. By (2.15) the number of unpaired electrons declines exponentially with temperature and one observes a corresponding decline in the surface resistance of the superconductor.

A simple application of the two fluid model yields a surface resistance

$$R_S \propto \omega^2 \exp\left(-\alpha \frac{T_c}{T}\right) \tag{2.16}$$

that drops exponentially to zero at $T = 0$. Measurements on real superconductors show that the surface resistance is in fact given by

$$R_S = A_S \frac{\omega^2}{T} \exp\left(-\alpha \frac{T_c}{T}\right) + R_0 = R_{\mathrm{BCS}} + R_0. \tag{2.17}$$

Here A_S is a material dependent constant. The first term is the BCS resistance, which is similar to that given by (2.16). The second term in (2.17) is a temperature independent residual resistance. Its nature is not completely understood, but it has been established that it is affected by, for example, impurities, trapped flux, adsorbed gases, and microscopic particles.

The R_0 term always dominates R_S at low temperatures. For well prepared niobium R_0 of 5 nΩ is possible. It is therefore pointless to cool superconducting cavities to temperatures for which $R_{\mathrm{BCS}} \ll R_0$. At 1.5 GHz, for example, the residual resistance of niobium begins to dominate at $T < 1.8$ K.

2.3.3 Critical magnetic fields

One of the unique characteristics of superconductors is that they expel any externally applied dc magnetic field H_{ext} provided that H_{ext} is less than a critical field. This phenomenon is called the Meissner effect (see, for example, [40]). Two classes of (low temperature) superconductors exist, known as type I and type II. The superconducting mechanism is the same in both cases, but the surface energy for normal conducting–superconducting boundaries differs for the two types. As a result, type I and type II superconductors behave differently in a magnetic field.

In the case of type I superconductors, the surface energy is positive. This class remains

in the perfect Meissner state in applied dc fields up to a temperature dependent critical field H_c. However, by expelling the applied field the superconductor raises its energy. When $H_{\text{ext}} > H_c$ the magnetic energy exceeds the energy gained by producing Cooper pairs, and the sample goes normal conducting ("quenches"). The temperature dependence of H_c is given by [40]

$$H_c(T) = H_c(0)\left[1 - \left(\frac{T}{T_c}\right)^2\right]. \tag{2.18}$$

Type II superconductors (such as niobium [8] and Nb_3Sn) are different because the surface energy of a superconducting–normal conducting interface is negative, so that the creation of interfaces can be energetically favorable. Similar to type I materials, they too expel a dc magnetic field completely up to a lower critical field H_{c1}. Rather than quenching above this value, though, they enter what is known as the mixed state, where normal conducting cores of radius ξ_0 form in the superconductor. Each core carries a magnetic flux quantum $\Phi_0 = hc/(2e)$. The density of these flux tubes, or "fluxoids", increases with H_{ext} until the entire sample becomes normal conducting at an upper critical field H_{c2}.

Based on these observations with dc fields, one might believe that RF cavities can only operate effectively up to a field $H_{\text{peak}} = H_{c1}$ for type II or H_c for type I materials. However, in the RF case the situation is relaxed with respect to DC fields.

It takes a normal conducting region a finite amount of time to nucleate in a superconductor when H_{ext} exceeds H_c (H_{c1} in type II materials). The nucleation time is on the order of 10^{-6} seconds [7] which is long compared to an rf period at microwave frequencies. Theory predicts, that the complete Meissner state persists up to a superheating critical field H_{sh} where $H_{\text{sh}} > H_c$ (type I), $H_{\text{sh}} > H_{c1}$ (type II) [15]. For niobium, the superheating critical field expected from theory is approximately 2200–2400 Oe [30]. The corresponding peak electric field for a typical cavity shape is about $E_{\text{peak}} = 100$ MV/m. An exact value of H_{sh} still needs to be measured, but experiments have indeed confirmed that niobium cavities can operate at $H_{\text{peak}} > H_{c1}$ [12].

CHAPTER 3

NITROGEN DIFFUSION INTO NIOBIUM EFFECT ON QUALITY FACTOR OF SRF CAVITY

3.1 Introduction

SRF cavities are the key technology for present and future particle accelerators, for high energy physics, nuclear physics, light sources, and accelerator-driven subcritical reactors. The invention and development of the particle accelerator structures made of superconducting niobium operating at low temperatures of 2–4.2 K revolutionized the accelerators. Required operation power is significantly reduced compare to the normal conducting copper cavities. High accelerating fields of over 40 MV/m are systematically achieved. Operation at duty factor of 100% becomes possible.

Several decades of SRF R&D at laboratories and universities worldwide have lead to the successful realization of niobium cavities that reliably achieve very high gradients and quality factors. Typical cavity surface processing for achieving state-of-art RF performance includes a combination of chemical treatments like electro-polishing (EP), buffered chemical polishing (BCP) and heat treatments. However, these structures suffer from a systematic effect of decreasing efficiency for increasing accelerating voltages (see Figure 2.7).

Superconductor surface resistance R_S (see definition in Equation (2.6)) attracted a lot of attention recently due to its important effect on SRF cavity performance. Temperature dependence of surface resistance is explained by quasi-particle concentration and follows Bardeen–Cooper–Schrieffer (BCS) predictions. Typically a good approximation of R_S is provided by the following equation (see Equation (2.17)):

$$R_S(T) = A \cdot \frac{\omega^2}{T} \cdot \exp\left(-\frac{\Delta}{kT}\right) + R_{\text{res}}, \tag{3.1}$$

where A is a constant depending on superconductor parameters, Δ is the superconducting

gap, and R_{res} is residual resistance. Weakly couples BCS theory describes temperature dependence, but the magnetic field dependence of surface resistance is much less understood. As follows from the Equation (2.13), surface resistance is directly related to the quality factor of the cavity. The geometry of the cavity determines the ratio between magnetic field and the accelerating field.

3.2 Nitrogen doping as a mechanism to modify surface resistance of superconducting niobium

These days SRF cavities are usually made of bulk niobium. Three distinct regions of the excitation curve are typically observed in niobium: low, medium and high field Q-slopes (Figure 2.7). It was demonstrated that the high field Q-slope can be removed by mild vacuum baking at 120°C for 48 hours. There is no developed procedure to control low field Q-slope, however as it was discovered at Fermilab in 2012 that nitrogen doping of the surface of SRF niobium cavity may lead not only to improvement of medium field Q-slope, but even to anti-Q-slope (see Figure 3.1). The discovery was made on single-cells (Figure 2.1b) treated with nitrogen in high temperature vacuum furnace (described in Section 3.3). During the first two years SRF Science Group at Fermilab focused on understanding the root of the improvement and making the process controllable and reproducible on single cells. Presented work is a part of the effort made in the last two years towards an optimized cavity processing recipe for LCLS–II and future particle accelerators.

As it was demonstrated in [10] certain concentration of nitrogen in the surface of cavity walls increase quality factor significantly. To explain the reason for anti-Q-slope deconvolution of surface resistance is required, i. e. surface resistance has to be presented as a sum of BCS and residual components according to the Equation (3.1). Standard phase-lock techniques were used to measure the excitation curve at variety of temperature values from 1.5 to 2.0 K. As quality factor is directly related to the surface resistance, measured data points

can be fitted with Equation (3.1) assuming R_S to be a function of temperature T at each value of accelerating field. Fitting parameters allow to distinguish temperature dependent R_{BCS} and residual R_{res}. The results for different cavity treatments are shown in Figure 3.2.

A variety of cavity surface treatments are presented: BCP and EP, with and without low temperature bake. In addition electro-polished cavities with nitrogen doping are tested. Both residual and BCS components of the surface resistance are smaller for the nitrogen treated cavities, especially for higher field. Anti-Q-slope emerges from the BCS surface resistance decreasing with field.

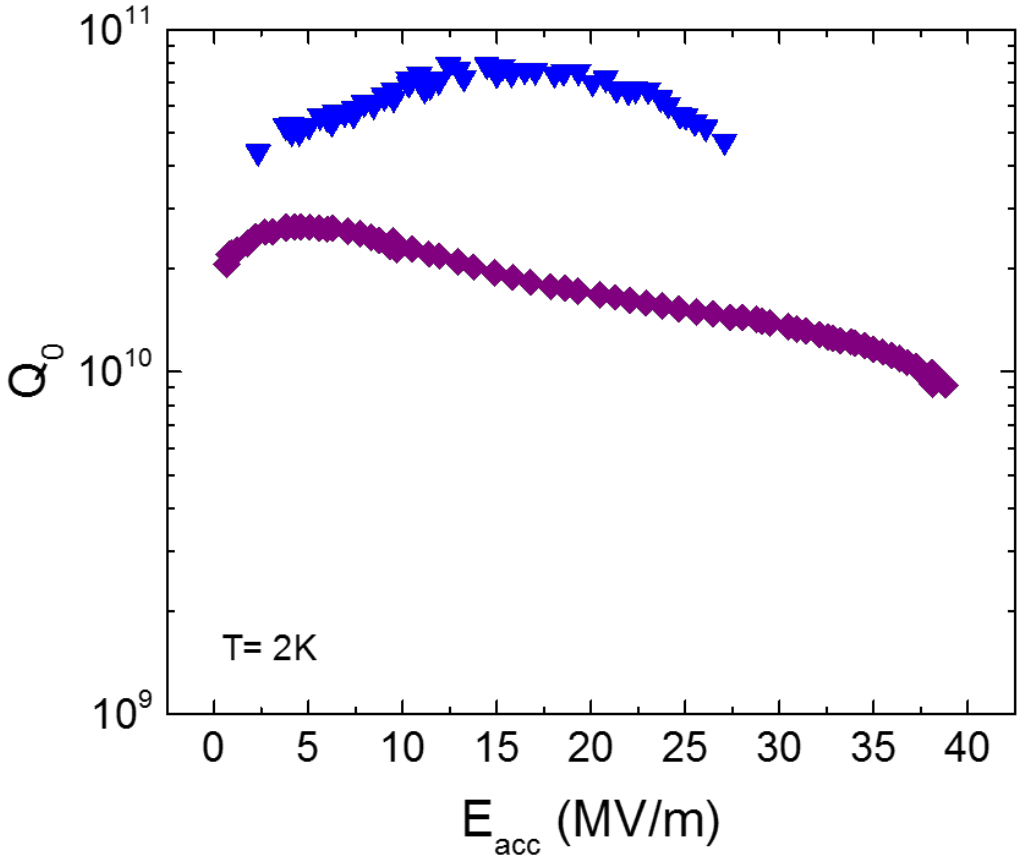

Figure 3.1: Excitation curves (Q_0 versus E_{acc}) for single-cell SRF niobium cavities. Performance of the cavity undergone the standard surface treatment with additional low temperature 120°C bake for 48 hours is shown in purple. Nitrogen doped cavity performance is shown in blue. The measurements are done at 2 K. The quality factor of nitrogen treated cavity is four times higher compare to the standard treatment at 16 MV/m.

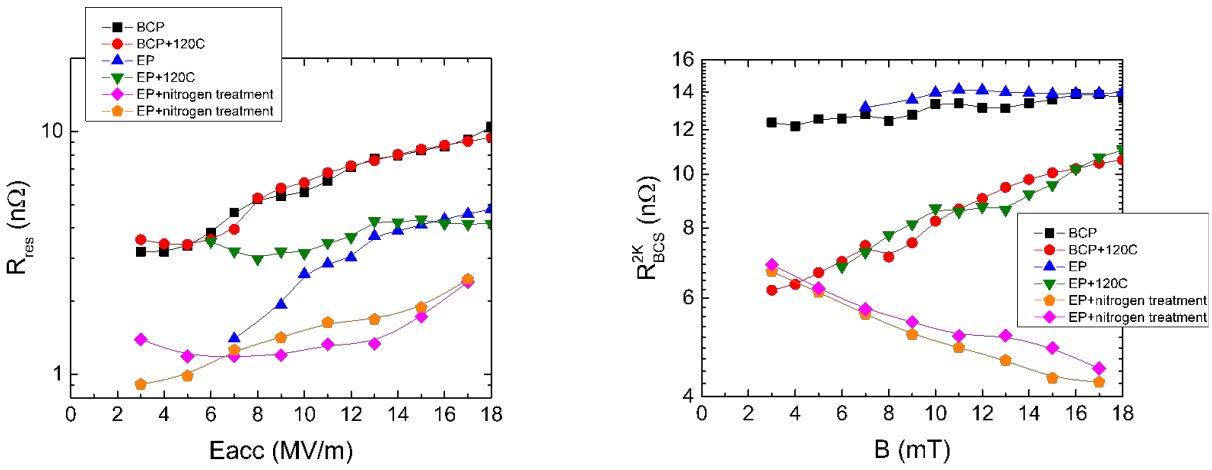

(a) Residual component.

(b) BCS component.

Figure 3.2: Residual and BCS components of the surface resistance of SRF cavity as functions of accelerating field. A variety of cavity surface treatments are presented. BCS component is calculated at 2 K.

An effort to improve SRF cavity performance using the standard surface treatment was done to meet ILC requirements. Multiple 9-cell TESLA-type fine-grain niobium cavity excitation curves were measured since 2008. The results are shown in Figure 3.3a. Excitation curves were measured at 1.8 and 2.0 K. All demonstrated cavities satisfy the ILC requirements, but none of them meet the LCLS–II one. Leaping ahead, one can compare the results from standard treated cavities with an example of nitrogen doped cavity excitation curve shown in Figure 3.3b.

3.3 Nitrogen doping procedure

The purpose of nitrogen doping into niobium SRF cavity walls is to add atoms of nitrogen into the surface layer of the walls. Compositions of nitrogen and niobium should be avoided as they are not superconductors. Nitrogen atoms transfered to the cavity walls via diffusion process. To perform the process, SRF cavity is placed inside a vacuum furnace (see Figure 3.4). The furnace is used for high temperature bake of the cavity, but also allows to perform nitrogen doping. To stimulate the diffusion of nitrogen into the cavity walls, the

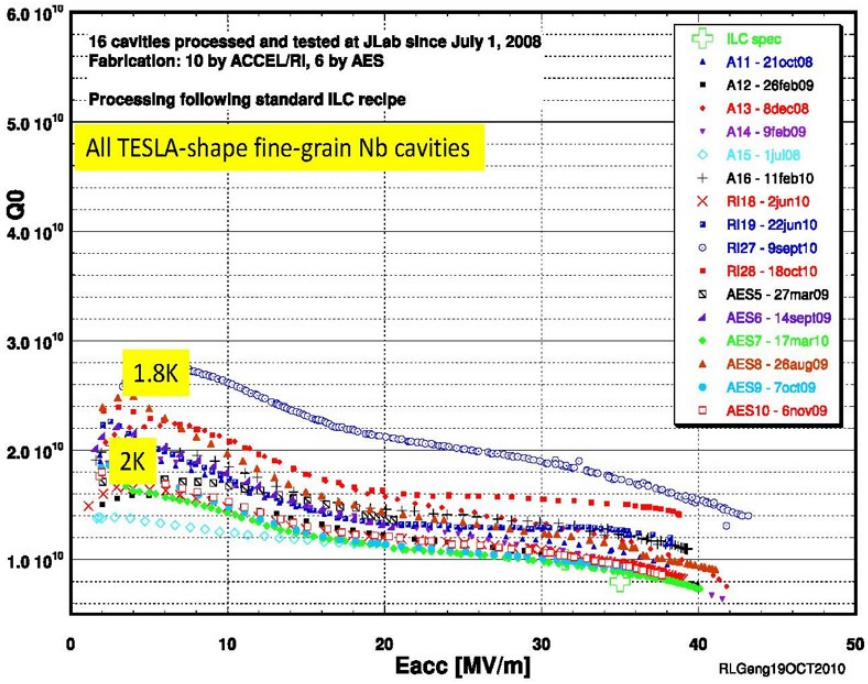

(a) Standard treatment.

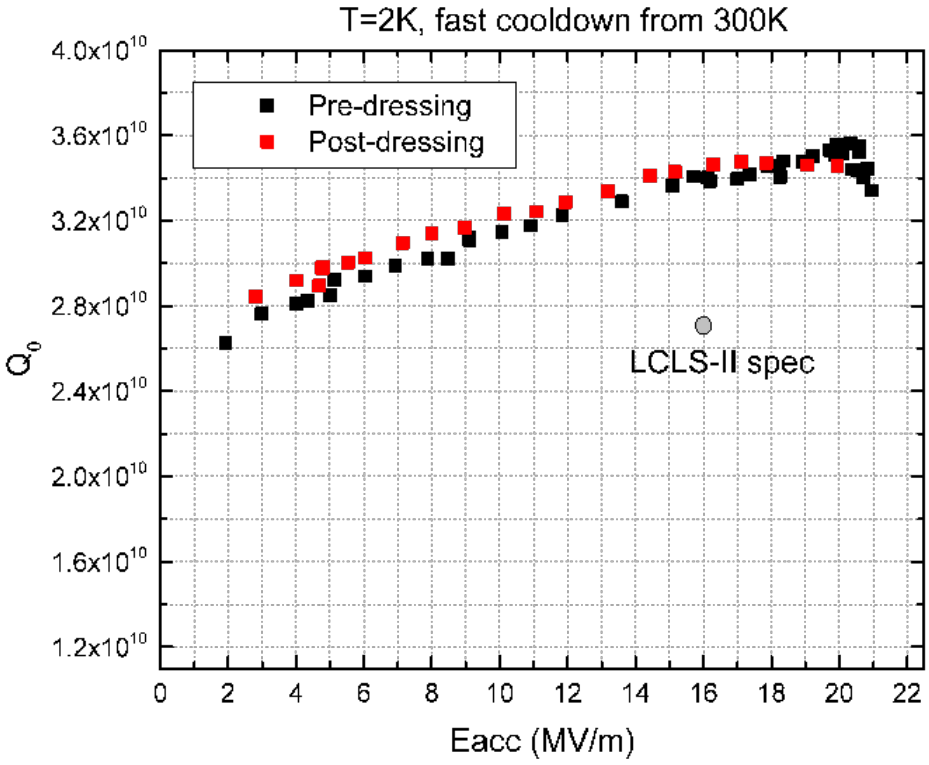

(b) Nitrogen doping.

Figure 3.3: The results of excitation curves measurements for SRF cavities with standard surface treatment (a) and nitrogen doping (b).

cavity needs to heat up and certain pressure of nitrogen gas needs to be created inside the cavity.

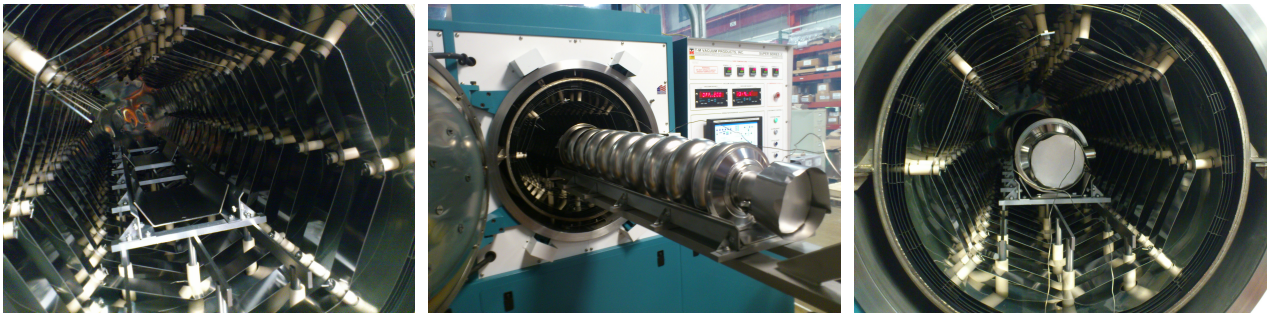

(a) (b) (c)

Figure 3.4: The photographs of nitrogen doping treatment of niobium SRF cavity at Fermilab. The vacuum furnace is shown on Figure 3.4a. An SRF cavity made from ultra-pure high-RRR niobium (see Figure 3.4b) is placed inside the furnace (see Figure 3.4c). The furnace allows to keep the cavity at high vacuum and high temperature. Instead of vacuum state, it is possible to create a certain pressure of nitrogen inside the furnace and the cavity.

The treatment starts with heating up the cavity from room temperature to 800°C. Temperature of the cavity and nitrogen pressure inside the cavity as a function of time during the treatment is shown on Figure 3.5. Then the cavity is baked for 3 hours at constant temperature in the vacuum. To reach a reasonable rate of diffusion, nitrogen doping of niobium SRF cavity performed at high temperature of 800°C. Nitrogen gas introduced to the atmosphere of the cavity to reach certain pressure. The gas stays inside the cavity for time t_1. During this time nitrogen diffuses into the surface of the cavity walls. After time t_1 nitrogen is pumped down from the furnace atmosphere, and after that the cavity is kept at 800°C for time t_2. At this stage more nitrogen does not penetrate the cavity walls, but the concentration profile of nitrogen in niobium changes. After that the furnace is cooled down back to room temperature. During the cool down, nitrogen concentration profile slightly changes again.

At this temperature niobium nitride formation happens. As a result after the doping there are nitrides at the surface of the cavity walls (see Figure 3.6). Fortunately, these nitrides are formed at the very surface of niobium, and surface removal of 2 μm with electro-polishing

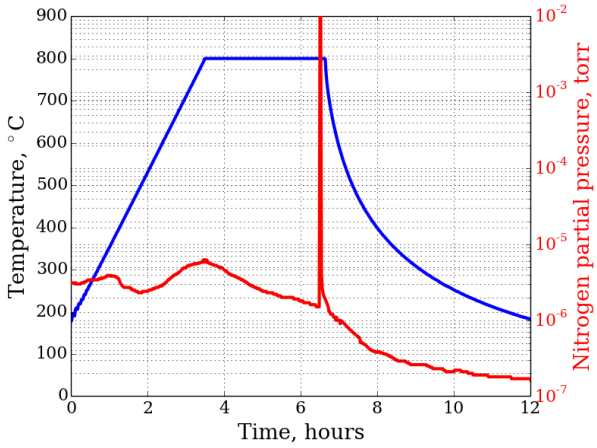

Figure 3.5: An example of high temperature bake and nitrogen treatment of SRF cavity. Temperature as a function of time is shown in blue line. Nitrogen pressure inside the cavity as a function of time is shown in red line.

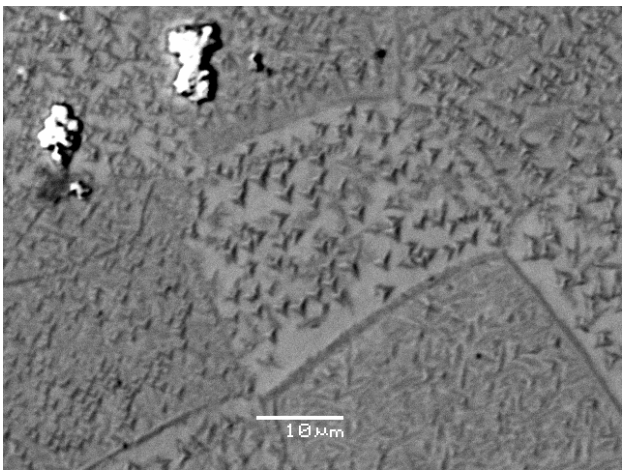

Figure 3.6: An image of the surface of niobium sample after the nitrogen treatment at 800°C (same as SRF cavity treatment). Niobium nitride formation can be observed on the surface of the sample.

allows to avoid normal conducting fractions in the walls of the cavity.

Typically, even more material removed from the surface with electro-polishing. Only first few nanometers (about 40 nm) of the material surface affect the surface resistance, that is why the purpose of the removal is to reach certain concentration of nitrogen right at the surface of niobium cavity.

3.4 Model description

Nitrogen doping procedure described in Section 3.3 allows us to create a model describing nitrogen diffusion into the surface of niobium under the given assumptions. The primary purpose of the model is to predict nitrogen concentration at the surface of the cavity after applied treatment, but to answer this question quantitative understanding of the diffusion process is required. First let us summarize the nitrogen doping procedure described in Section 3.3. Treatment process consists of four steps.

1. Partial pressure of nitrogen gas inside the volume of the cavity is p. Temperature of the system is T. Treatment time is t_1. This stage can be approximated with the infinite

source diffusion model.

2. Nitrogen is pumped down from the volume of the cavity, but cavity's temperature is still T. At this stage nitrogen diffused at first step changes its concentration profile. Treatment time is t_2. Finite source approximation can be applied.

3. Cool down from T to room temperature. This step can be approximated with finite source diffusion model with changing temperature.

4. Surface layer removal with electro-polishing.

For the given approximation it is assumed, that nitrogen partial pressure changes (from zero to p and back) infinitely fast in the volume of the cavity and stays constant after the change. Nitrogen partial pressure when it is pumped down is exactly zero (compare to Figure 3.5). Temperatures of the cavity and the gas inside are the same and don't change with time except the cool down step. Niobium nitrides do not form on the surface or inside the material. Even this assumption does not hold at considered doping temperature of 800°C (see Figure 3.6), perturbation to the model prediction is assumed to be small. Diffusion does not happen at room temperature. The latter assumption is valid with good precision due to diffusion coefficient exponential dependence on temperature.

To construct the estimation for the surface concentration of nitrogen after described treatment, the diffusion equation has to be solved for each stage of the treatment taken into account corresponding border and initial conditions:

$$\frac{\partial C(x,t)}{\partial t} = D\frac{\partial^2 C(x,t)}{\partial x^2}, \tag{3.2}$$

where $C(x,t)$ is the nitrogen concentration inside niobium as function of depth x and time t, D is the diffusion coefficient. The diffusion coefficient dependence on temperature is described as

$$D = D_0 \exp\left(-\frac{E_A}{RT}\right), \tag{3.3}$$

where E_A is activation energy, D_0 is constant, R is gas constant. Activation energy and D_0 depend on the source and material of the diffusion. For the given range of temperature the literature values of the parameters are $D_0 \approx 0.86$ m^2/s and $E_A \approx 146$ kJ. Gas constant $R \approx 8.31$ J/K.

The combination of Sieverts' law and Henry's law determines the border condition for the first stage:

$$C(0,t) = C_0 \exp\left(\frac{C_1}{T}\right), \tag{3.4}$$

i. e. surface concentration of nitrogen during infinite source diffusion. Coefficient C_0 is proportional to the square root of the partial pressure of nitrogen: $C_0 = A_0\sqrt{p}$. A_0 and C_1 are constants with unknown values. Analytical solution of the diffusion Equation (3.2) with the initial condition $C(x,0) = 0$ for $x > 0$ and the border conditions (3.4) and $C(\infty,t) = 0$ is

$$C(x,t) = C(0,t) \cdot \operatorname{erfc}\left[\frac{x}{2\sqrt{D(T)t}}\right]. \tag{3.5}$$

Thus, at the end of the first stage of the treatment, nitrogen concentration profile is described by the following formula:

$$N_1(x) = A_0\sqrt{p}\exp\left(\frac{C_1}{T}\right) \cdot \operatorname{erfc}\left[\frac{x}{2\sqrt{D(T)t}}\right]. \tag{3.6}$$

and shown on Figure 3.7a for $T = 800°$C and $t_1 = 20$ minutes.

The initial condition for the second step of the treatment is given by (3.6). The border condition is $C(\infty,t) = 0$ and $C(x,t) = 0$ for $x < 0$. Besides, there is a condition on conservation of total amount of nitrogen diffused into niobium at the first stage:

$$\int_0^\infty C(x,t)\mathrm{d}x = \int_0^\infty N_1(x)\mathrm{d}x. \tag{3.7}$$

Given problem without limitation $C(x,t) = 0$ for $x < 0$ can be interpreted as a composition of Fokker–Planck equations with zero drift and diffusion coefficient independent on position

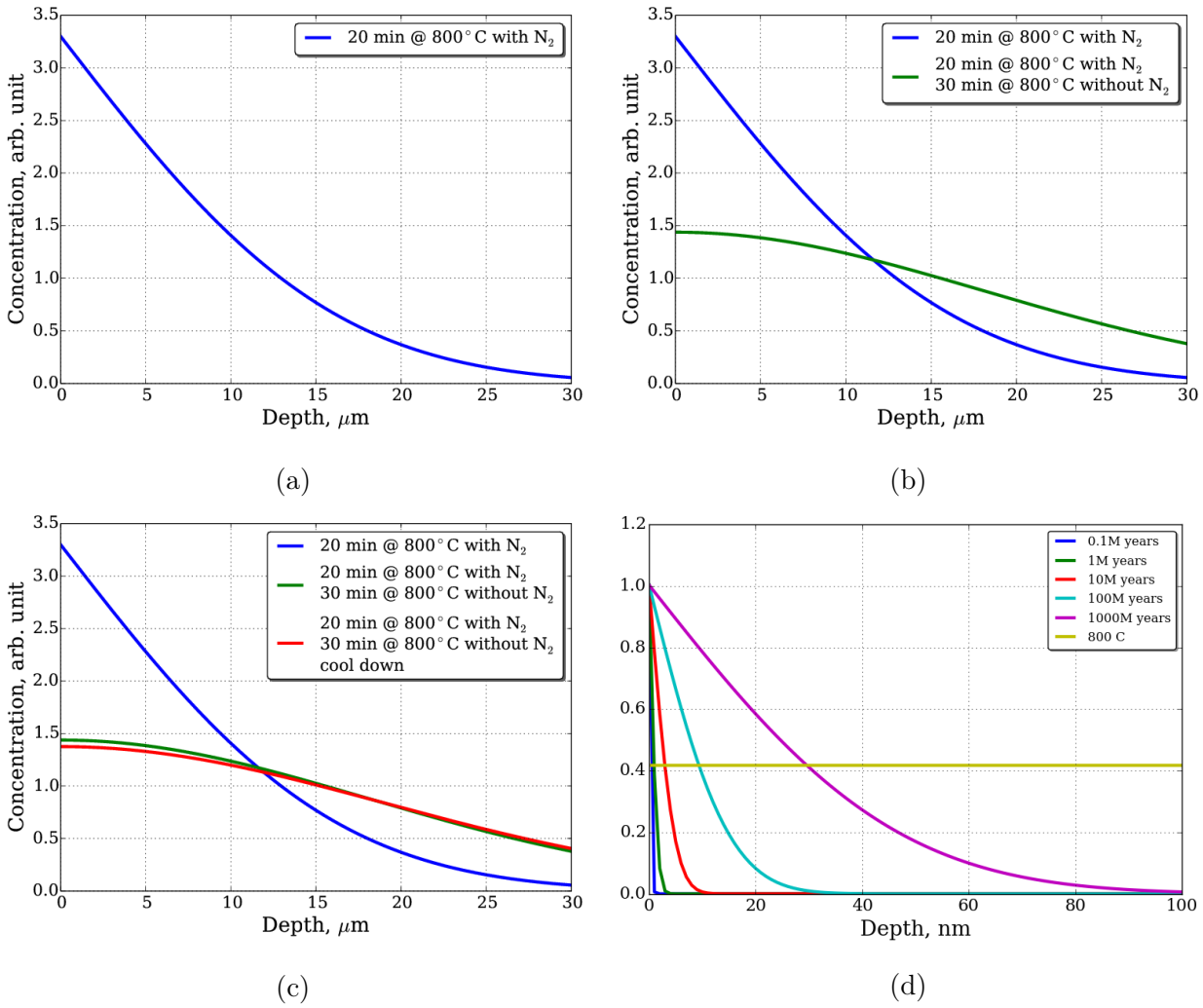

Figure 3.7: Nitrogen concentration profiles during diffusion into niobium after infinite source diffusion for 20 minutes (a), finite source diffusion for 30 minutes (b), cool down to room temperature according to Figure 3.5 (c), and infinite source diffusion at room temperature for a variety of huge periods of time from 100,000 years to 1 billion years (d). The purpose of the last plot is to demonstrate that diffusion at low temperatures can be neglected.

and time (or Wiener process with diffusion coefficient D instead of $1/2$). To do so initial condition (3.6) should be represented as

$$N_1(x) = \int_0^\infty N_1(\xi)\delta(\xi)\mathrm{d}\xi. \tag{3.8}$$

The solution of Fokker–Planck equation states that if initial diffusion source is located in one point ($N_1(\xi)\delta(\xi)\mathrm{d}\xi$), then concentration profile after time t looks like

$$\mathrm{d}\tilde{C}(x,t;\xi) = \frac{N_1(\xi)\mathrm{d}\xi}{2\sqrt{\pi Dt}} \exp\left[-\frac{(x-\xi)^2}{4Dt}\right], \tag{3.9}$$

To take into account the limitation $C(x,t) = 0$ for $x < 0$, the surface of niobium can be considered as a mirror reflecting the distribution of nitrogen according to the Fokker–Planck equation. Thus, the solution of the diffusion equation for the conditions of the second stage of the treatment is given by Fokker–Plank equation solution with both initial concentration profile and its reflection in the mirror.

$$\begin{aligned} \mathrm{d}C(x,t;\xi) &= \frac{N_1(\xi)\mathrm{d}\xi}{2\sqrt{\pi D(T)t}} \exp\left[-\frac{(x-\xi)^2}{4D(T)t}\right] + \frac{N_1(\xi)\mathrm{d}\xi}{2\sqrt{\pi D(T)t}} \exp\left[-\frac{(x+\xi)^2}{4D(T)t}\right] = \\ &= \frac{C_0 e^{C_1/T}}{2\sqrt{\pi D(T)t}} \mathrm{erfc}\left[\frac{\xi}{2\sqrt{D(T)t}}\right] \left\{\exp\left[-\frac{(x-\xi)^2}{4D(T)t}\right] + \exp\left[-\frac{(x+\xi)^2}{4D(T)t}\right]\right\} \mathrm{d}\xi. \end{aligned} \tag{3.10}$$

Total concentration profile during the second step can be found by integration of Equation (3.10):

$$\begin{aligned} C(x,t) &= \int \mathrm{d}C(x,t;\xi) = \\ &= \frac{C_0 e^{C_1/T}}{2\sqrt{\pi D(T)t}} \int_0^\infty \mathrm{erfc}\left[\frac{\xi}{2\sqrt{D(T)t}}\right] \left\{\exp\left[-\frac{(x-\xi)^2}{4D(T)t}\right] + \exp\left[-\frac{(x+\xi)^2}{4D(T)t}\right]\right\} \mathrm{d}\xi. \end{aligned} \tag{3.11}$$

After substitutions

$$\begin{aligned} u &= \frac{\xi}{2\sqrt{D(T)t}}, \\ v &= \frac{x}{2\sqrt{D(T)t}} \end{aligned} \tag{3.12}$$

the integral can be simplified to

$$C(x,t) = \frac{C_0 e^{C_1/T}}{\sqrt{\pi}} \int_0^\infty \operatorname{erfc}(\alpha u) \left[e^{-(u-v)^2} + e^{-(u+v)^2} \right] \mathrm{d}u, \tag{3.13}$$

where

$$\alpha = \sqrt{\frac{t}{t_1}}. \tag{3.14}$$

Thus, concentration profile on nitrogen after the second step of the treatment is

$$N_2(x) = \frac{A_0}{\sqrt{\pi}} \cdot \sqrt{p} \cdot \exp\left(\frac{C_1}{T}\right) \cdot J\left[\sqrt{\frac{t_2}{t_1}}, \frac{x}{2\sqrt{D(T)t_2}}\right] \tag{3.15}$$

with

$$J(\alpha, v) = \int_0^\infty \operatorname{erfc}(\alpha u) \left[e^{-(u-v)^2} + e^{-(u+v)^2} \right] \mathrm{d}u. \tag{3.16}$$

Both concentration profiles after the first and after the second step of the diffusion (with t_2=30 minutes) are shown on Figure 3.7b.

A necessary step in the diffusion process is the furnace cool down from the bake temperature $T = 800°\mathrm{C}$ to room temperature of $T_\mathrm{r} \approx 25°\mathrm{C}$ (see Figure 3.5). To describe this step quantitatively one can divide the cool down by multiple short time sub-processes of length $\mathrm{d}t$. During each of these sub-processes temperature changes by $\mathrm{d}T(t)$. If $\mathrm{d}t$ is very small, then $\mathrm{d}T(t) \ll T$ and during each of the sub-processes can be considered constant and concentration profile change can be described by the following equation (similar to (3.10)):

$$\mathrm{d}^2 C(x,t;\xi,\mathrm{d}t) = \frac{C(\xi, t-\mathrm{d}t)\mathrm{d}\xi}{2\sqrt{\pi D(T(t))\mathrm{d}t}} \left\{ \exp\left[-\frac{(x-\xi)^2}{4D(T(t))\mathrm{d}t} \right] + \exp\left[-\frac{(x+\xi)^2}{4D(T(t))\mathrm{d}t} \right] \right\}, \tag{3.17}$$

where $C(\xi, t-\mathrm{d}t)$ is concentration profile after previous sub-process. Numerical calculations of the concentration profile after cool down along with the profiles after the first and second steps of diffusion are shown in Figure 3.7c.

Note that we did not specify the room temperature precisely. The reason is that according to Equation (3.3) the diffusion coefficient decays exponentially when temperature decreases. The significance of the diffusion coefficient reduction is demonstrated in Figure 3.7d. It shows how the nitrogen concentration profile would look like after the first step of diffusion at room temperature ($T_r = 25°C$ is selected) after a variety of huge periods of time: from 100,000 years to 1 billion years. The concentration profile of nitrogen diffused at 800°C is also shown on the graph for the comparison. The depth scale is in nm for this plot in contrast to plots in Figures 3.7a–3.7c. According to Equation (3.4) the surface concentration of nitrogen is higher for room temperature, but it would take over 100,000 years for nitrogen to penetrate further than 1 nm inside the walls.

3.5 Comparison with secondary ion mass spectrometry results

3.5.1 Secondary ion mass spectrometry

Secondary ion mass spectrometry (SIMS) is a technique used to analyze the composition of solid surfaces by sputtering the surface of the sample with a focused primary ion beam and collecting and analyzing ejected secondary ions. The mass to charge ratios of these secondary ions are measured with a mass spectrometer to determine the elemental, isotopic, or molecular composition of the surface to a depth of a few μm. SIMS is the most sensitive surface analysis technique, with elemental detection limits ranging from parts per million to parts per billion.

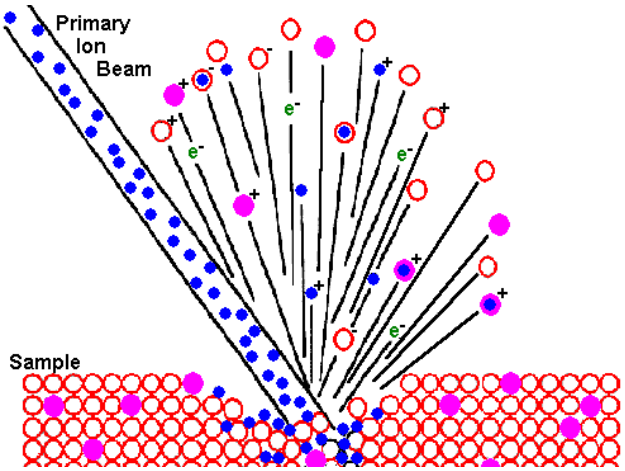

Figure 3.8: Representation of secondary ion mass spectrometry measurements.

3.5.2 Comparison with diffusion model

A set of square shaped samples made of the same niobium as SRF cavities was treated with standard surface preparation procedure. After that each sample was placed in the vacuum furnace next to the actual cavity for the nitrogen doping (Figure 3.9). To test the model a variety of doping procedures was performed. The diffusion happened at different temperatures with different time parameters t_1 and t_2. To avoid possible errors during diffusion process, two samples were treated with each recipe.

Figure 3.9: Small square niobium sample placed inside the vacuum furnace next to the SRF cavity for nitrogen doping.

After the doping, all niobium samples undergone SIMS measurements. Nitrogen concentration as a function of depth was measured. Again, to avoid possible errors, the concentration profile was measured in two spots at each sample. Concentration profiles were fitted with Equation (3.15) using known time parameters and temperature. A_0 and C_1 served as fitting parameters.

The results of SIMS measurements along with model calculations shown in Figure 3.10. Samples #1 and #2 correspond to the nitrogen doping at 500°C (Figure 3.10a). Samples #3 and #4 correspond to the nitrogen doping at 400°C (Figure 3.10b). As there are two spots measured with SIMS for each sample, there are four nitrogen concentration profiles presented at each plot.

First of all, it is necessary to notice that all concentration profile curves coincide with very good precision at each plot. This means that diffusion procedure is reproducible.

There are three parts in the shape of the concentration profile curve:

- abrupt decrease in the first about 100 nm;
- monotonic decrease for a few μm;
- constant after a certain value of depth.

First part represents possible nitrides formation on the surface of niobium and increased surface concentration (3.4) due to slow diffusion during the cool down. The last part is caused by the depth limit in SIMS measurements. When measured spot at the sample surface is deep (Figure 3.8), the primary ion beam hits the walls of the spot. Thus SIMS measures some average concentration instead of the concentration at specific depth. The middle part of the curve is actual nitrogen concentration profile, presented model predicts.

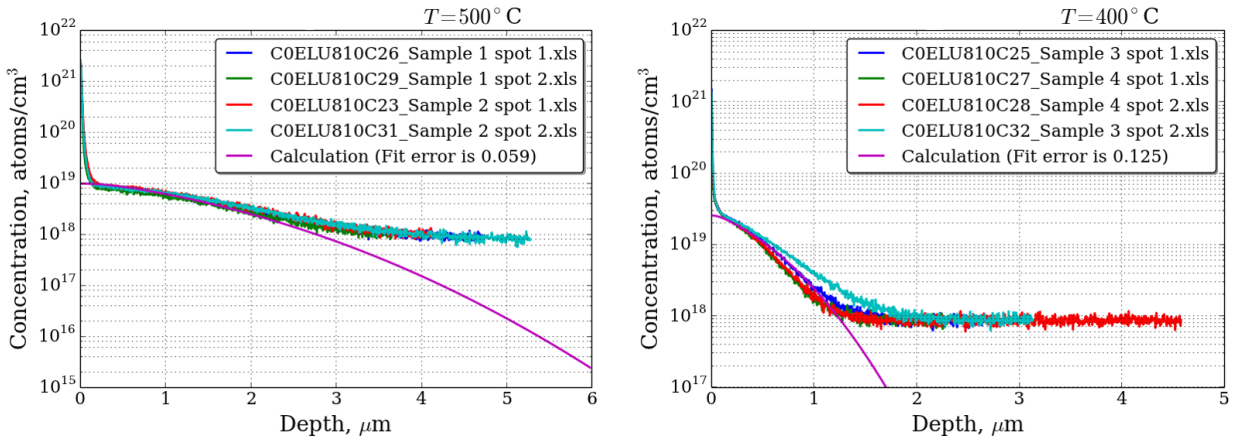

(a) Samples #1 and #2: $T = 500°$C. (b) Samples #3 and #4: $T = 400°$C.

Figure 3.10: Concentration profiles of nitrogen diffused into niobium samples at 400°C and 500°C measured with SIMS and calculated with presented diffusion model (purple line).

The purple line in Figures 3.10 are the results of the model calculations. The middle part of the curves is described very well with the model. This result demonstrate that the model can be used for controlled quality factor optimization with nitrogen doping.

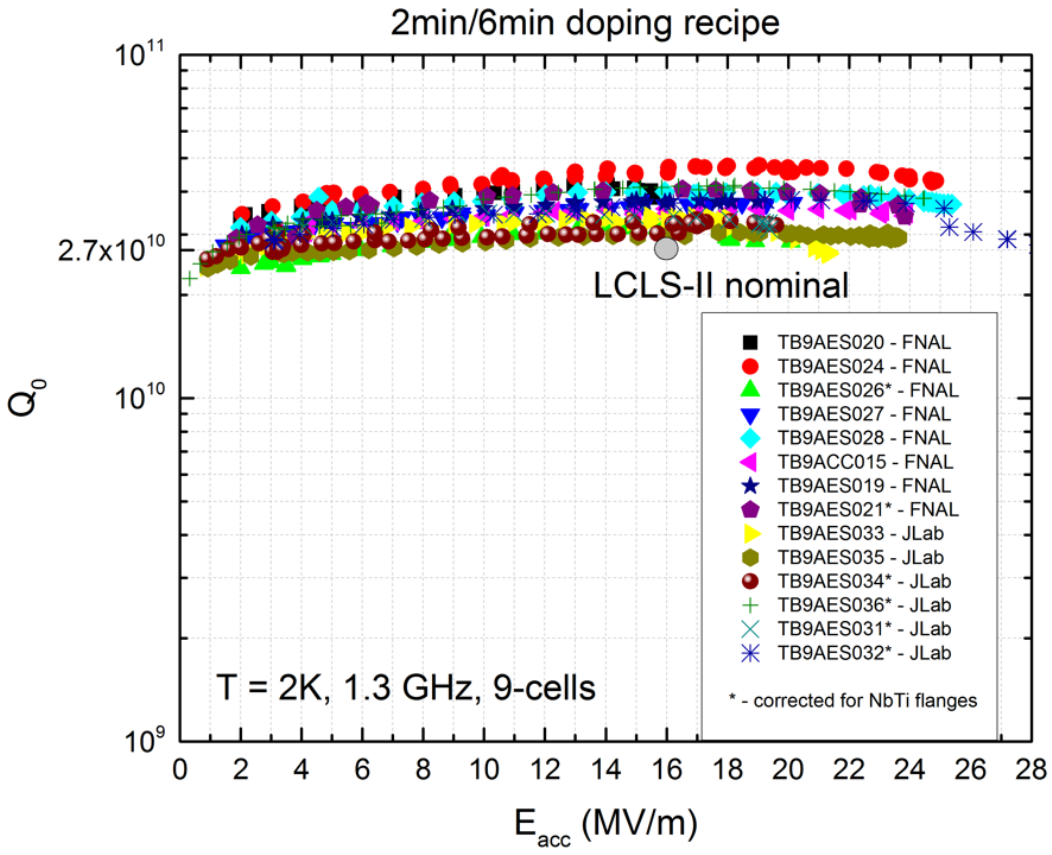

Figure 3.11: Excitation curves for 16 nine-cell SRF cavities treated with nitrogen doping qualified for two LCLS–II prototype cryo-modules. The curves are measured with standard phase-lock technique at 2 K. The average quality factor at $E_{\rm acc}$ =16 MV/m is $3.6 \cdot 10^{10}$. The average value of $E_{\rm acc}^{\rm max}$ is 22.2 MV/m. The median value of $E_{\rm acc}^{\rm max}$ is 22.8 MV/m.

3.6 Application to quality factor optimization

A variety of doping recipes were designed, implemented and tested based on the model described in Section 3.4. Two-step diffusion prevailed over one-step diffusion process as it created flatter and deeper nitrogen concentration profile. This improved robustness of the recipe results and quench field. The suggested recipe is the two-step nitrogen doping procedure: infinite source diffusion for $t_1 = 2$ minutes and limited source diffusion for $t_2 = 6$ minutes at 800°C. After doping, 5 μm of the surface is removed with electro-polishing. Starting 2014 nine-cell nitrogen doped cavities have been produced. At this moment 16

cavities satisfy the LCLS–II requirements and qualify for two prototype cryo-modules. The excitation curves for these cavities are shown in Figure 3.11.

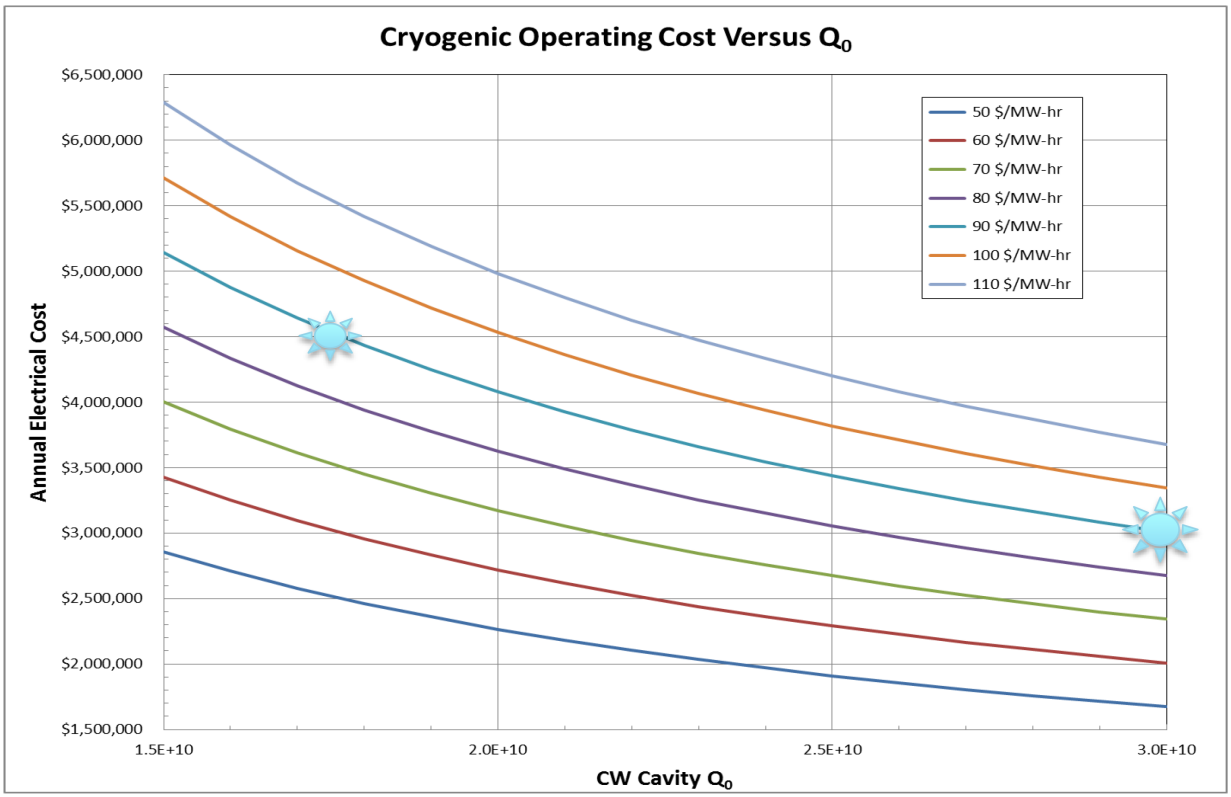

Figure 3.12: The effect of quality factor improvement on annual operating cost of cryogenic system for proposed LCLS–II machine.

The effect of quality factor improvement on annual operating cost of cryogenic system for proposed LCLS–II machine is shown in Figure 3.12. Higher quality factor value of $3 \cdot 10^{10}$ compared to $1.7 \cdot 10^{10}$ translates into about \$1.5 million savings per year in operating cost. Capital cost savings go in thresholds of several tens of millions of US Dollars for LCLS–II.

CHAPTER 4

LOW ENERGY MUON SPIN ROTATION MEASUREMENTS OF MAGNETIC FIELD PENETRATION INTO SUPERCONDUCTOR

4.1 LE-μSR technique

Low energy muon spin rotation (LE-μSR) is a unique technique to perform precise microscopic measurements of the magnetic field profile $B(z)$ inside superconductors. It recently has become available at the μE4 beam line at PSI. LE-μSR unmatched sensitivity was demonstrated on thick niobium films in the clean limit. A clear evidence for a nonlocal electromagnetic response was found, which is beyond the reach of any other existing technique. Besides, ideally suitable depth range of 0–130 nm and spot size of about 1 cm, makes LE-μSR an ideal probe to address the problem of understanding the difference in microscopic superconducting properties of niobium affected by different treatments.

The Meissner–Ochsenfeld effect [16], stating that at low frequencies and magnitudes of external magnetic field a superconductor expels or excludes any magnetic flux from its core, is a fundamental property of a superconductor. However, the magnetic field penetrates at the surface of the superconductor. The magnetic penetration depth is a typical length scale on which the field penetrates. A good approximation of the magnetic field dependence on depth for a large scale of superconductors is exponential one. It is derived for a semi-infinite superconductor in the London limit [14]. The approximation does not always hold for impurity doped type I superconductor. It was demonstrated by Pippard on a set of microwave experiments in [31].

In analogy with the anomalous skin effect Pippard introduced the concept of nonlocal response of the superconductor, i. e., the screening current trying to expel the magnetic field must be averaged over some spatial region of the order of ξ called the coherence length. The

physical interpretation of ξ is, that it is the length over which the superconducting wave function can be considered as rigid, i. e., roughly speaking the size of a Cooper pair. The nonlocal electrodynamic response leads to various modifications of the London theory, one being that the magnetic penetration profile $B(z)$ is no longer exponential and even changes its sign beneath the surface of the superconductor. All these findings were confirmed by the microscopic BCS theory [1]. Although these theoretical predictions have been known for half a century, only very recently has a "direct" measurement of the functional dependence of $B(z)$ been demonstrated using LE-μSR. For example, the results providing a direct and quantifiable measure of nonlocal effects in investigated materials and allowing the extraction of physical parameters such as the magnetic field penetration depth and the coherence length ξ are published in [38] and [39].

For SRF technology purpose the superconducting properties within 130 nm from the surface can be directly revealed with LE-μSR. This is achieved by measuring the magnetic field inside the superconductor as a function of depth.

4.2 Theoretical background

An external electromagnetic field acts on the ground state of a superconductor as a perturbation. Within standard perturbation expansion one can show [35] that the following nonlocal relation between the current density $\vec{j}$ and the magnetic field vector $\vec{B}$ holds:

$$j_\alpha = \sum_\beta \int K_{\alpha\beta}(\vec{\rho}) A_\beta(\vec{r}') \mathrm{d}\vec{r}', \tag{4.1}$$

where $\vec{\rho} = \vec{r} - \vec{r}'$, $K_{\alpha\beta}(\vec{\rho})$ is called the integral kernel:

$$K_{\alpha\beta}(\vec{\rho}) = R_{\alpha\beta}(\vec{\rho}) - \frac{e^2 n_S}{m^*} \delta(\vec{\rho}) \delta_{\alpha\beta}, \tag{4.2}$$

where e is the charge, n_S is the super-current density, and m^* is the effective mass of the charge carrier. The vector potential $\vec{A}(\vec{r})$ needs to be properly gauged in order that Equation (4.1) is physically meaningful. $R_{\alpha\beta}(\vec{\rho})$ describes the paramagnetic response, whereas the second term in the bracket reflects the diamagnetic one. If the ground state wave function of the superconductor were "rigid" with respect to all perturbations (rather than only those which lead to transverse excitations) $R_{\alpha\beta}$ would be identically zero and Equation (4.1) would reduce to the second London equation:

$$j_\alpha(\vec{r}) = -\frac{1}{\mu_0}\frac{1}{\lambda_L^2}A_\alpha(\vec{r}) \tag{4.3}$$

with London depth penetration depth

$$\lambda_L = \sqrt{\frac{m^*}{\mu_0 e^2 n_S}}, \tag{4.4}$$

where μ_0 is the permeability of the vacuum. This, along with the Maxwell equation

$$\nabla\vec{B} = \mu_0\vec{j}, \tag{4.5}$$

results for a semi-infinite sample, in the penetration profile

$$B(z) = B_{\text{ext}} \exp\left(-\frac{z}{\lambda_L}\right), \tag{4.6}$$

where z is the depth perpendicular to the surface and B_{ext} is the externally applied magnetic field strength.

In situations when the paramagnetic term $R_{\alpha\beta}(\vec{\rho})$ in Equation (4.1) cannot be neglected one arrives at the more complicated formula:

$$B(z) = B_{\text{ext}}\frac{2}{\pi}\int \frac{q}{q^2 + \mu_0 K(q\xi, T, l)}\sin(qz)\mathrm{d}q. \tag{4.7}$$

$K(q\xi, T, l)$ is the Fourier transformed kernel from the Equation (4.1) including the electron mean free path l. Since only the one-dimensional case will be considered everything is expressed in scalar form.

Starting from a possible analogy between the anomalous skin effect and the Meissner–Ochsenfeld effect, Pippard arrived at the formula for the kernel

$$\mu_0 K_P(q\xi, T, l) = \frac{1}{\lambda^2(T)} \frac{\xi_P(T,l)}{\xi_P(0,l)} \left\{ \frac{3}{2} \frac{1}{x^3} \left[\left(1 + x^2\right) \arctan(x) - x \right] \right\} \tag{4.8}$$

with $x = q\xi_P(T,l)$, and the Pippard coherence length $\xi_P(T,l)$. The temperature dependence of $\xi_P(T,l)$ could be explained only later in BCS theory and is

$$\frac{1}{\xi_P(T,l)} = \frac{J(0,T)}{\xi_P(0)} + \frac{1}{l} \tag{4.9}$$

with

$$J(0,T) = \left[\frac{\lambda(T)}{\lambda(0)} \right]^2 \frac{\Delta(T)}{\Delta(0)} \tanh \left[\frac{\Delta(T)}{2k_\mathrm{B}T} \right], \tag{4.10}$$

where $\Delta(T)$ is the superconducting energy gap and k_B is the Boltzmann constant.

4.3 Experimental setup

The LE-μSR technique uses beams of 100% spin-polarized positive muons (μ^+), which serve as sensitive local magnetic probes when implanted inside a sample. At the μE4 beam line at PSI, a high intensity surface muon beam with an energy of about 4 MeV is moderated to ultra-low epithermal energies (about 15 eV) in a cryogenically condensed solid argon film deposited on a 10 K–cold argon foil. These epithermal muons are subsequently accelerated by electrostatic fields to energies up to 30 keV, corresponding to implantation depths of up to about 140 nm in niobium.

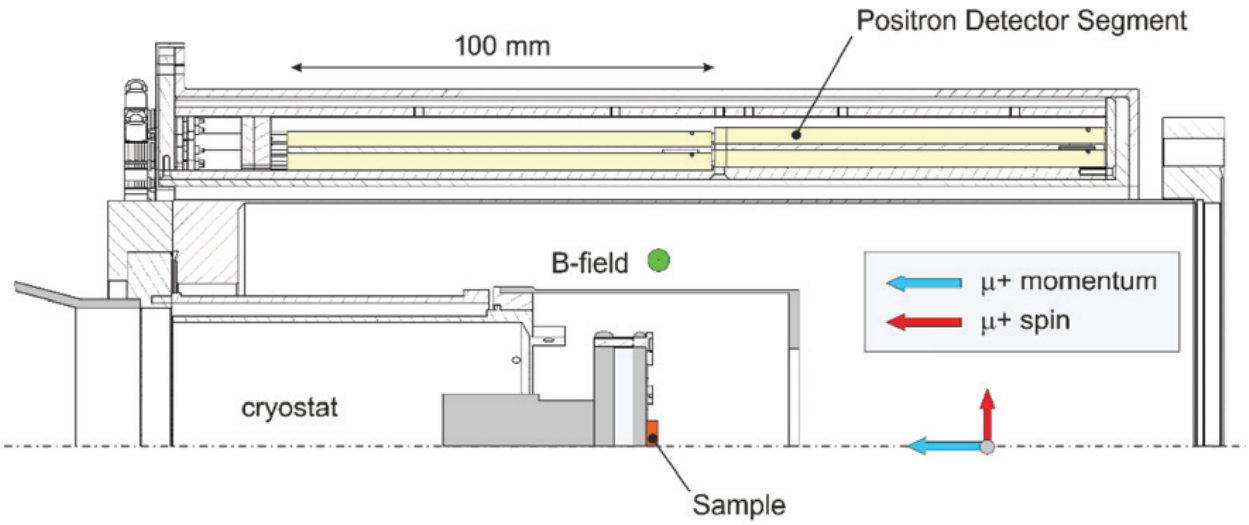

Figure 4.1: The schematic of the LE-μSR experiment.

The schematic of the experimental arrangement are shown in Figure 4.1. Measured muon flux distribution on the sample is shown in Figure 4.2. Upon implantation, the muon precesses in the local magnetic field at its stopping site. The precession frequency is proportional to the magnetic field and is measured by detecting the anisotropic muon decay (lifetime $\tau_\mu = 2.2$ μs): the decay positrons are preferentially emitted in the direction of the μ^+ spin, which allows to monitor the time evolution of the muon spin by registering the positrons in detectors surrounding the sample (see Figure 4.1). The number of positron events at each of the detectors is described by the following form:

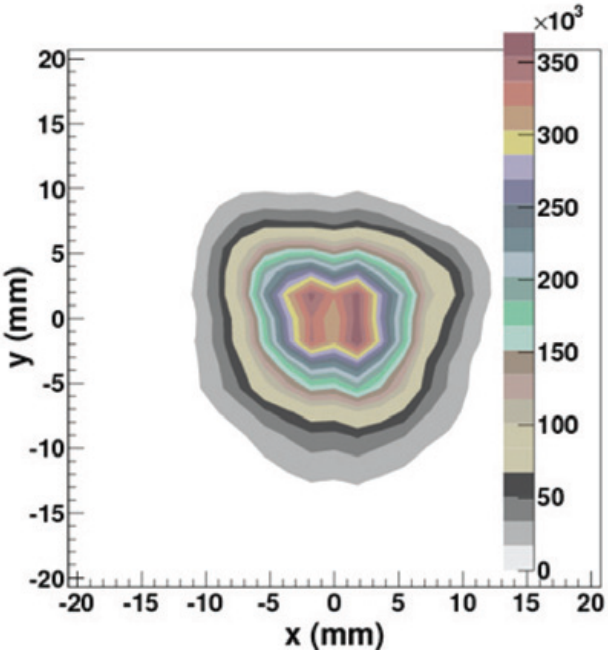

Figure 4.2: Measured muon flux distribution. Beam spot at the sample position.

$$N(t) = N_0 e^{-t/\tau_\mu} [1 + A(t)] + N_{\text{bkg}}, \tag{4.11}$$

where $A(t) = A_0 P(t)$ describes the time evolution of the muon ensemble polarization $P(t)$, and A_0 is the experimental decay asymmetry. N_{bkg} is a time-independent uncorrelated background. The assymetry $A(t)$ is given by averaging over the muon stopping distribution $n(z, E)$

$$A(t) = A_0 \exp\left[-\frac{(\sigma t)^2}{2}\right] \int n(z, E) \cos\left[\gamma B(z) t + \phi\right] \mathrm{d}z, \tag{4.12}$$

where $\gamma = 2\pi \times 135.42$ MHz/T is the muon gyromagnetic ratio, ϕ is the detector phase, and σ is a Gaussian depolarization rate, reflecting the dipolar broadening due to nuclear spins.

4.4 Measurement procedure

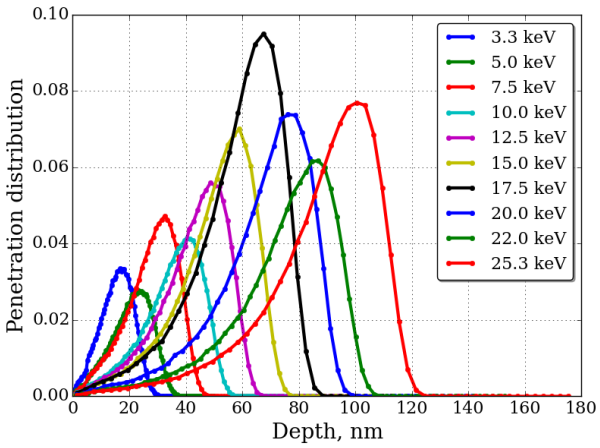

Figure 4.3: Implantation profiles.

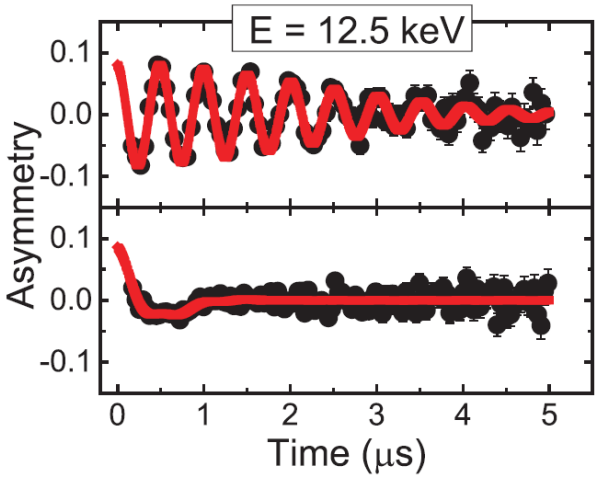

Figure 4.4: Asymmetry example.

The experimental procedure was to perform zero-field cooling to temperature of 3 K and then apply a magnetic field B_a parallel to the sample surface and transverse to the muon spin (see Figure 4.1). The magnitude of magnetic field B_a was confirmed in each case by performing a run in a normal conducting state at temperature 10 K above the transition temperature of niobium ($T_c \approx 9.25$ K) where the Meissner effect is absent. Muon implantation energies between 3.3 and 25.3 keV were used. Corresponding implantation profiles simulated using the computer code TRIM.SP are shown in Figure 4.3. For the simulations, niobium oxide (Nb_2O_5) of 5 nm thickness was assumed as the topmost layer.

Several millions decay positrons were collected for each muon energy. Examples of asymmetry signals $A(t)$ obtained on the same sample at $B_a = 15$ mT and $E = 12.5$ keV in the normal conducting and superconducting states are shown in Figure 4.4. The Meissner effect becomes manifested in the reduction of the precession frequency and the heavily damped $A(t)$ caused by the broad field distribution in the stopping range of the muons.

For the studies niobium SRF cavities of TESLA elliptical shape were used. Residual resistivity ration of niobium is $RRR \sim 300$. After manufacturing cavities were electro-polished for removal of about 120 μm material using a standard solution of HF:H_2SO_4:HPO_3.

4.5 Data analysis

All data were analyzed using the program musrfit. A simple Gaussian fit model is typically used for the data analysis. This model is well-established, that is why it was used for comparison of presented results with previously published ones. However, previous studies on thick niobium films in the clean limit showed that a very good description of the experimental data is provided by the Pippard non-local model with the renormalization of $\lambda_L \to \lambda_L/\sqrt{Z}$ and of the coherence length $\xi_0 \to \xi_0 Z$ where $Z \approx 2.1$. Since earlier SRF cavity experiments showed that electro-polished niobium are also in the clean limit, a similar behavior is expected for our samples.

The Gaussian approximation states

$$A(t) = A_0 \exp\left[-\frac{(\sigma_{\mathrm{SC}} t)^2}{2}\right] \cos\left(\gamma_\mu B_{\mathrm{G}} t + \phi\right), \tag{4.13}$$

where B_{G} is in very good approximation equal to $\bar{B}$ which is given by

$$\bar{B} = \int_0^\infty B(z) n(z, E) \mathrm{d}z. \tag{4.14}$$

The screened magnetic field B_{G} as a function of the mean muon stopping depth

$$\bar{z} = \int_0^\infty z n(z, E) \mathrm{d}z. \tag{4.15}$$

measured in [33] is presented in Figure 4.5.

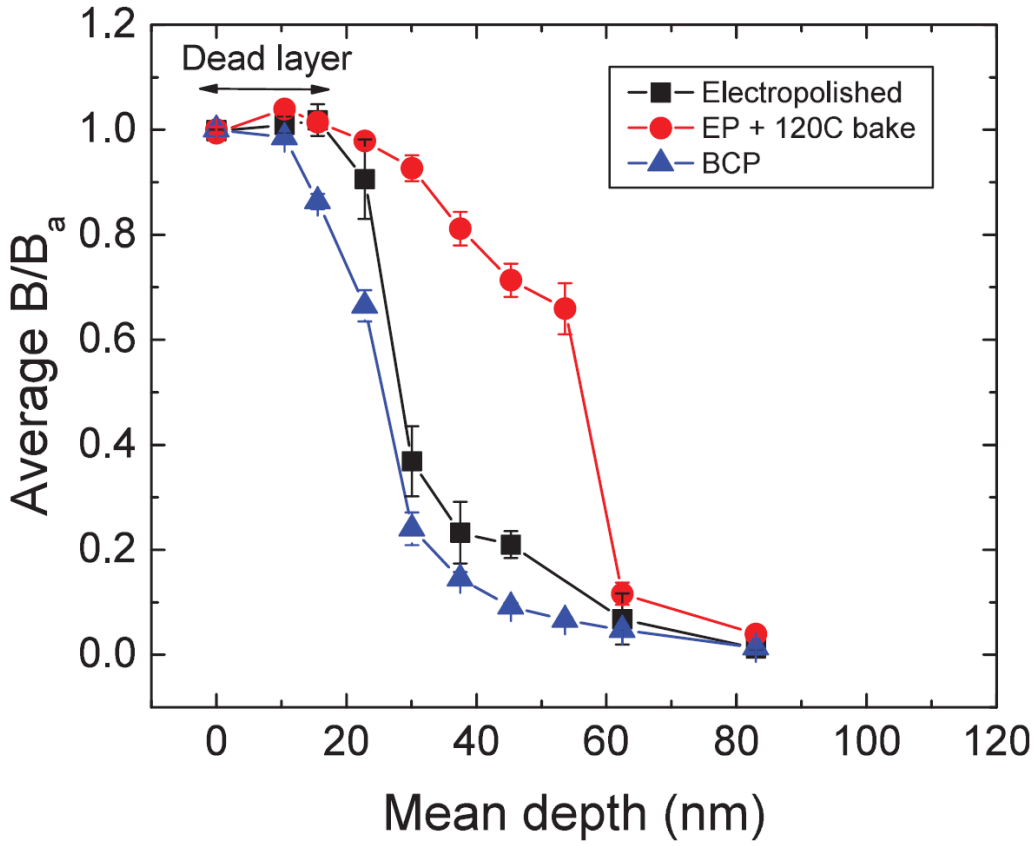

Figure 4.5: Magnetic field profiles $\bar{B}(\bar{z})$ at external field of $B_a = 25$ mT using the Gaussian model.

In the present work the Pippard approximation described in Section 4.2 was applied to the same niobium sample undergone bulk electro-polishing followed by the low temperature bake. Measured average magnetic field as a function of depth is presented in Figure 4.6. The same measurement was also performed for the niobium sample after the nitrogen doping. The result demonstrates smaller penetration depth of magnetic field for this sample, i. e. similar behavior to the electro-polished sample without bake.

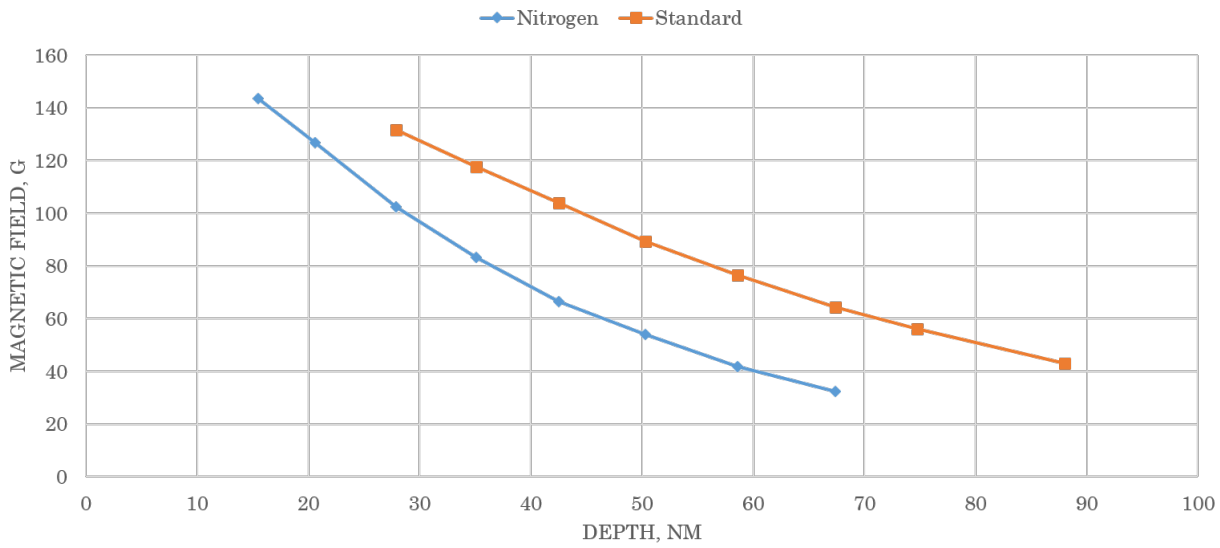

Figure 4.6: Magnetic field penetration profile calculated using the Pippard approximation.

4.6 Measurement results

Literature value of electron mean free path ($\ell = 400$ nm) for pure niobium sample is confirmed. Measured magnetic field penetration depth $\lambda_{\mathrm{L}} = 44.42 \pm 0.17$ nm is close to the bulk magnetometer measurements results of $\lambda_{\mathrm{L}} = 46 \pm 2$ nm.

For the niobium sample undergone the nitrogen doping, magnetic field penetration depth is extracted from the fitting function is $\lambda_{\mathrm{L}} = 36.6 \pm 0.4$ nm for external magnetic field of $B_a = 15$ mT and $\lambda_{\mathrm{L}} = 37.8 \pm 0.4$ nm for external magnetic field of $B_a = 25$ mT. This allows to conclude that nitrogen doping does not change the London penetration depth λ_{L} of magnetic field.

The effect of nitrogen doping results in the change of mean free path. Compare to the pure niobium mean free path of 400 nm, after the nitrogen doping measured mean free path is $\ell = 42.6 \pm 0.1$ nm. It is independent on depth. For low temperature baked sample mean free path is depth-dependent and is in range from 2 to 16 nm.

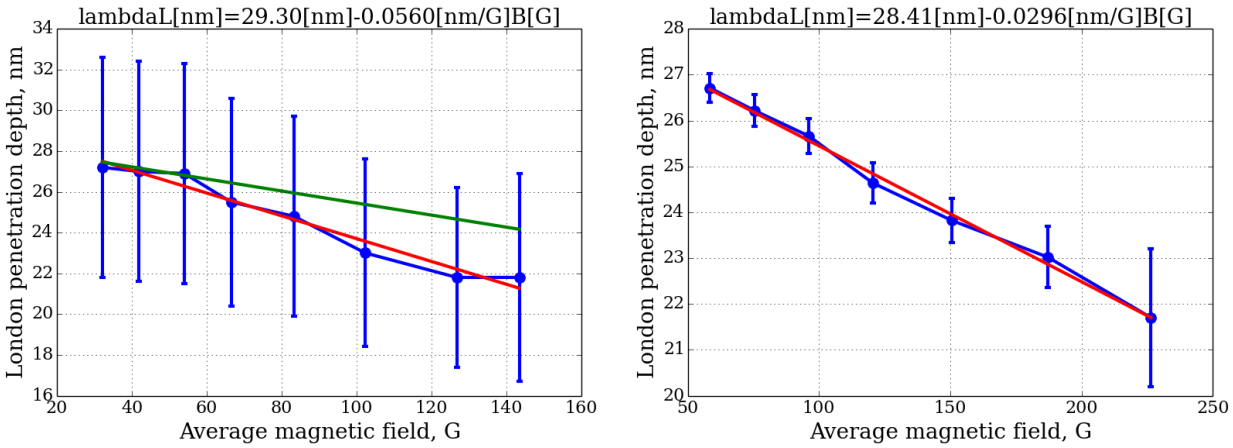

(a) $B_a = 15$ mT. (b) $B_a = 25$ mT.

Figure 4.7: London penetration depth as a function of local magnetic field for applied magnetic field values of 15 mT (a) and 25 mT (b). The approximation of λ_L dependence of magnetic field for the measurements with 25 mT external field is shown on the plot with measurements for 15 mT external field in green line.

4.7 Test of λ_L dependence of local magnetic field.

A hypothesis of λ_L dependence on local magnetic field was tested. The same niobium sample with nitrogen atom diffused into the surface undergone LE-μSR measurements with different external magnetic field: 15 and 25 mT. For each magnetic field value muon implantation energies from 3.3 to 25.3 keV were used. Global fit in the form of the Pippard approximation was applied to the data. In contrast to presented above and in previous publications measurements, fitting parameter λ_L was considered muon energy dependent. Muon penetration depth depends on its energy as shown in Figure 4.3. Magnetic field decays penetrating inside the superconductor (see Figures 4.5 and 4.6), which allows to consider parameter λ_L local magnetic field dependent.

Extracted from the fit values of λ_L as a function of local magnetic field for both external magnetic field values are presented in Figure 4.7. Figure 4.7b shows the results for $B_a = 25$ mT. These results have better measurement precision compare to the results for applied field $B_a = 15$ mT due to higher magnetic field. Given data suggests linear dependence of

λ_{L} on local magnetic field and can be fitted with function

$$\lambda_{\mathrm{L}}\ [\mathrm{nm}] = 28.41 - 0.03 \cdot B\ [\mathrm{G}]. \tag{4.16}$$

The fit line is shown in red.

The data collected for the measurement with 15 mT applied magnetic field is more noisy (see Figure 4.7a), but still can be fitted with a linear function

$$\lambda_{\mathrm{L}}\ [\mathrm{nm}] = 29.30 - 0.06 \cdot B\ [\mathrm{G}]. \tag{4.17}$$

The fit line is shown in red. The slopes of two linear fits (4.16) and (4.17) differ by a factor of two, but if linear fit from the measurement at $B_a = 25$ mT (4.16) is plotted on top of the measurements at $B_a = 15$ mT (the green line in Figure 4.7a) it happens to be within the error bars. Similarly a linear approximation with zero or even positive slope can be found within the error bars.

Thus, the measurements at external magnetic field of 25 mT supports the hypothesis of parameter λ_{L} dependence on local magnetic field and indicates the linear dependence with negative slope. However, the measurements at lower external magnetic field of 15 mT does not contradict this suggestion, but does not indicate any significant dependence of London penetration depth on local magnetic field. Based on these two measurements it can be concluded that possible proportionality coefficient between λ_{L} and B is limited by the following condition:

$$\left|\frac{\mathrm{d}\lambda_{\mathrm{L}}}{\mathrm{d}B}\right| < 0.1\ \frac{\mathrm{nm}}{\mathrm{G}}, \tag{4.18}$$

which is not significant at considered range of magnetic field values.

CHAPTER 5

MAGNETOMETER MEASUREMENTS OF CRITICAL MAGNETIC FIELDS

5.1 Introduction

The Meissner–Ochsenfeld effect states that a superconductor expels magnetic flux from its core when external magnetic field $\vec{H}$ is applied. This is valid at low frequency and magnitude of applied magnetic field. Magnetic field $\vec{B}$ inside the superconductor can be expressed as the following:

$$\vec{B} = \mu_0 \left[\vec{H} + \vec{M}(H) \right], \tag{5.1}$$

where μ_0 is the vacuum permeability and $\vec{M}$ is the magnetization of the material. Magnetic susceptibility χ is a function of the magnitude of the applied field:

$$\vec{M}(H) = \chi(H)\vec{H}. \tag{5.2}$$

Equation (5.1) can be rewritten as

$$\vec{B} = \mu\vec{H}, \tag{5.3}$$

where $\mu = \mu_0 [1 + \chi(H)]$.

In Meissner state type–II superconductor expels magnetic flux completely. Therefore, magnetic field $\vec{B} = \vec{0}$ and as follows from Equation (5.1) $\vec{M}(H) = -\vec{H}$, when $H < H_{c1}$ (see Figure 5.1). H_{c1} is called lower critical magnetic field. When the magnitude of applied magnetic field $\vec{H}$ is slightly above the lower critical field, magnetic flux starts penetrating the superconductor. This state of superconductor is called a vortex state. When applied field is higher than H_{c2} (the upper critical magnetic field), the material looses superconducting properties.

A common experimental procedure used to characterize the magnetic susceptibility is to

apply external DC magnetic field to the sample and measure the induced field within the sample.

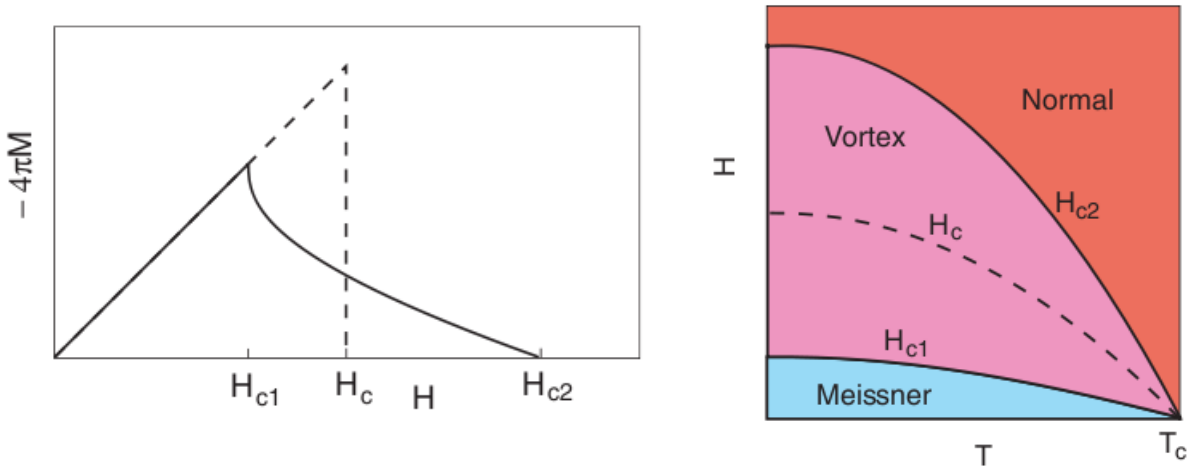

(a) (b)

Figure 5.1: Theoretical dependence of the magnetization on the applied magnetic field for type II superconductor (a) and its state diagram (b).

However, when the magnitude of applied magnetic field is in the range between H_{c2} and H_{c3}, only a thin surface sheath is superconducting while the bulk is in the normal conducting state. H_{c3} is called a surface critical magnetic field.

AC magnetic susceptibility χ needs to be defined to explain the meaning of surface critical magnetic field. There is an alternative way to measure the magnetic susceptibility of a material which is to superimpose a small time varying or AC excitation $H_1 \cos(\omega t)$ on top of the DC external field H_0 and measure the AC response of the material. The dissipation caused by rearranging the magnetic domains gives rise to a complex magnetic susceptibility $\chi = \chi' - i\chi''$. The real part of the susceptibility is proportional to the component of the magnetization that is induced in-phase with the applied modulation while the imaginary part is proportional to the $\pi/2$ out of phase or quadrature component of the magnetization. It is this latter part which is directly proportional to the dissipation in the material.

The DC field H_0 can be slowly varied while keeping the magnitude of the modulation H_1 constant. The time varying AC excitation $\delta H = H_1 \cos(\omega t)$ will produce a small time

varying response $\delta B = B_1 \cos(\omega t + \theta)$. The response need not have the same phase as the drive. In fact, if the material possess a non-zero imaginary susceptibility, θ will also be nonzero. At a given H_0, the AC response at frequency ω measures the derivative of the B–H curve (see Equation (5.3)):

$$B_0 + \delta B = \left[\mu(H_0) + \left(\frac{\partial \mu}{\partial H} \right)_{H_0} \delta H + \frac{1}{2} \left(\frac{\partial^2 \mu}{\partial H^2} \right)_{H_0} (\delta H)^2 + ... \right] (H_0 + \delta H), \tag{5.4}$$

When external magnetic field variation $\delta H \to 0$, the term linear in δH is much larger than the higher order terms. Furthermore, if μ variation over the range of δH is assumed small, the following is valid:

$$\delta B = \mu(H_0)\, \delta H, \tag{5.5}$$

$$\mu(H_0) = \left. \frac{\mathrm{d}B}{\mathrm{d}H} \right|_{H=H_0}. \tag{5.6}$$

5.2 Experimental procedure

Magnetic measurements on niobium samples are a useful tool to investigate the effect of nitrogen doping on niobium critical fields. The experimental studies on the magnetization and susceptibility of niobium samples presented in the thesis have been carried out with the aim to gain an understanding of superconducting properties change by nitrogen doping.

The samples for the magnetization and susceptibility measurements are cylinders with diameter of 2.85 mm and a height of 7.0 mm, which are cut from $RRR \sim 300$ fine grain niobium sheets used for SRF cavity production. Bulk electro-polishing of about 120 μm removal was done on all samples. After that, one of the samples was baked for 48 hours at 120°C in the vacuum (low temperature bake). Such surface preparation in SRF cavities typically leads to maximum accelerating fields (quench field) of about 40 MV/m and above. Two other samples are prepared using different nitrogen doping recipes, which found to deliver SRF cavities with optimal quality factor (over $2.7{\cdot}10^{10}$ and above at 2 K and 16 MV/m for nine-cell cavity). The procedure of surface treatment (after initial bulk electro-polishing)

is the following (detailed description can be found in Section 3.3):

- high temperature bake at 800°C for 3 hours in the vacuum;
- bake at 800°C for time t_1 with nitrogen gas in the chamber (diffusion of nitrogen into niobium happens);
- after diffusion bake at 800°C for time t_2 in vacuum (diffused nitrogen redistributes inside the niobium walls to produce desired nitrogen concentration profile);
- 5 μm surface layer removal by electro-polishing (nitrides formed at the surface removed, desired surface concentration of nitrogen is achieved).

Time parameters t_1 and t_2 are subject to optimization. Optimal in terms of quality factor recipes have the following parameters: $t_1 = 2$ min, $t_2 = 6$ min and $t_1 = 20$ min, $t_2 = 30$ min. Cavities prepared with the first recipe have quench fields of up to about 30 MV/m. Cavities prepared with the second recipe have quench fields of up to about 25 MV/m. One more presented sample had no extra treatment after bulk electro-polishing and represents standard cavity surface treatment.

Sample DC magnetization is measured with a commercial magnetometer (Quantum Design Physical Property Measurement System (PPMS)) at 2 K in external DC magnetic field between zero and 1 T. The same system is also used for AC susceptibility measurements. A frequency of 10 Hz and AC field amplitude of 0.2 mT allow good noise suppression and an acceptable measurement time. In all measurements external magnetic fields are aligned parallel to the symmetry axis of the cylindrical samples. The demagnetization factor was calculated according to the theoretical expression [2]

$$N_Z = 1 - \frac{1}{1 + \frac{d}{h}\left\{\frac{4}{3\pi} + \frac{2}{3\pi}\tanh\left[1.27\frac{h}{d}\ln\left(1 + \frac{d}{h}\right)\right]\right\}}, \tag{5.7}$$

where d is the diameter of the sample and h is its height. For the given samples $N_Z = 0.195$.

The magnetization and susceptibility data presented below have been corrected using this demagnetization factor.

5.3 Critical temperature

The superconducting transition temperature T_c is determined from the onset of the screening component χ' of the complex AC susceptibility

$$\chi = \chi' - i\chi'' \qquad (5.8)$$

measured at zero DC field as a function on temperature (Figure 5.2). Critical temperature of all measured samples is about 9.25 K.

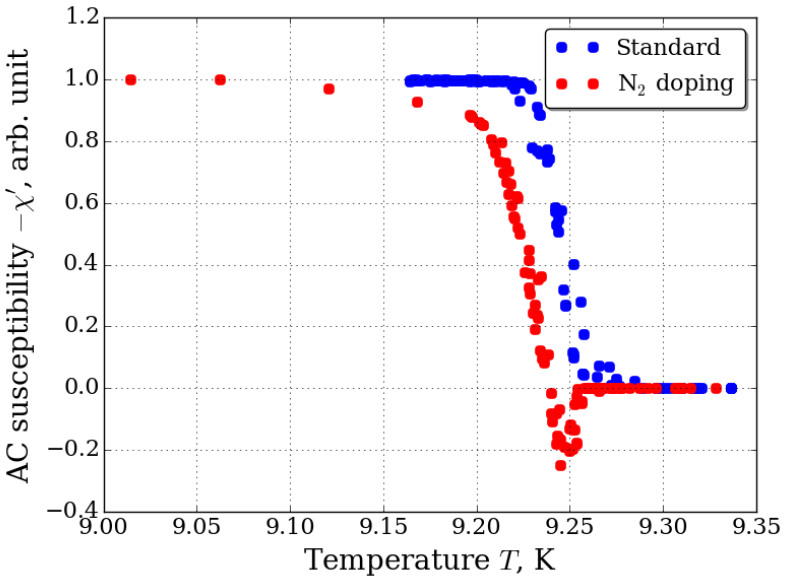

Figure 5.2: Real part of the linear AC susceptibility measured near zero-field transition temperature of the niobium samples. All considered samples have critical temperature about 9.25 K. The width of transition region depends on existence of normal conducting fractions at the surface of the superconductor.

Figure 5.2 shows screening component of the AC susceptibility as a function of temperature for baked sample and the sample treated with nitrogen before final electro-polishing. Transition zone for the latter sample is wider than for the baked sample. It means that niobium samples after nitrogen doping have a fraction in the surface with lower critical temperature.

Imaginary part of AC susceptibility χ'' in normal conducting state determined during this measurement. Its value used to determine critical surface field during the AC susceptibility measurements at 2 K.

5.4 Magnetization measurements

DC magnetization measurements result of the first three samples described in Section 5.2 is shown in Figure 5.3. Magnetization and external magnetic field corrected using demagnetization factor such that in Meissner state their sum is equal to zero. This fact represents magnetic field expulsion from the superconductor.

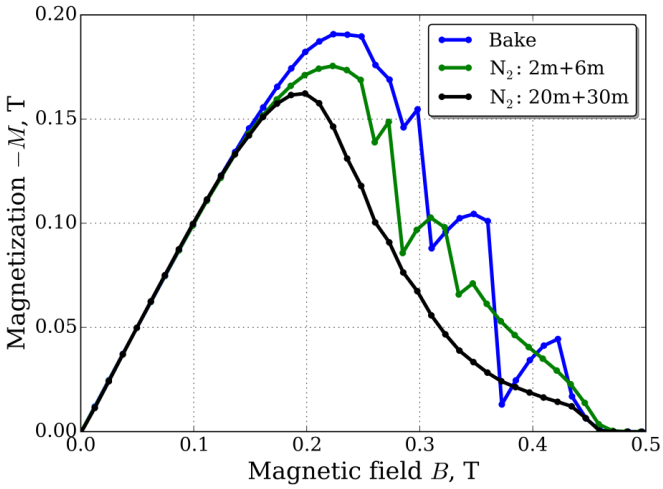

Figure 5.3: DC Magnetization of niobium samples as a function of external magnetic field at 2 K.

Penetration of magnetic field into the superconductor leads to the deviation of magnetization curve from a straight line. The deviation is greater when more magnetic flux penetrates the superconductor. Magnetization is equal to zero when external magnetic field is higher than upper critical field B_{c2}.

Figure 5.3 demonstrates that magnetic flux starts entering the superconductor at lower fields for nitrogen doped samples as compared to the low temperature baked one. Moreover, magnetic flux enters at lower fields for the sample exposed to nitrogen for 20 minutes as compared to the one exposed to nitrogen for 2 minutes only.

SRF cavities performance prepared according to these three recipes is presented in [9]. Low temperature baked cavities can reach quench fields of 35 MV/m and above. Cavities exposed to nitrogen for 2 minutes are found to have maximum quench fields of about 30 MV/m. Cavities prepared by the recipe assuming nitrogen exposure for 20 minutes can reach quench fields of 25 MV/m. Due to the cavity configuration, these values transform to 170 mT, 130 mT and 107 mT penetration magnetic field (i. e. external magnetic field when magnetic flux enters niobium), correspondingly. Further investigation is required to determine the exact relation between quench and amount of magnetic flux penetrated, but

obtained results allow ordering the samples by quench field based on magnetization curves.

There is no clear effect of nitrogen doping on the upper critical field, but it is found that nitrogen doping reduces the field of first flux penetration, likely a cause of the decrease of the quench field in N-doped SRF cavities.

5.5 Surface superconductivity

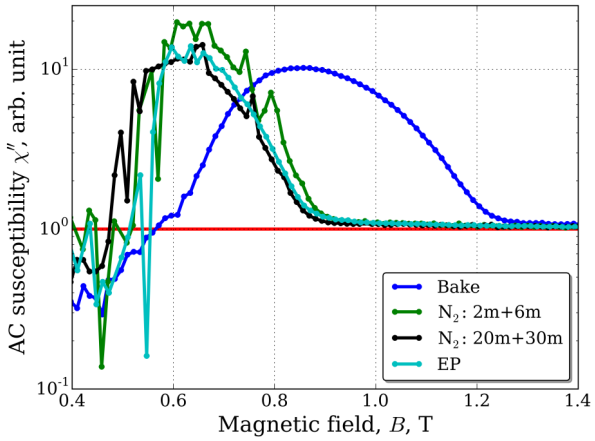

Figure 5.4: Field dependence of the imaginary part of AC susceptibility of niobium samples with different surface treatments. The data have been taken at 2 K, frequency is 10 Hz, AC field amplitude is 0.2 mT.

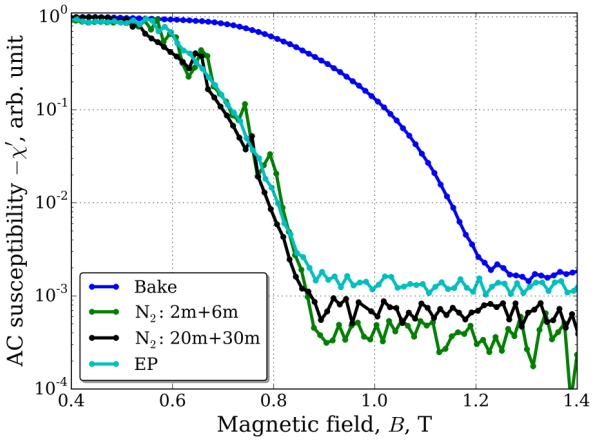

Figure 5.5: Field dependence of the real part of AC susceptibility of niobium samples with different surface treatments. The data have been taken at 2 K, frequency is 10 Hz, AC field amplitude is 0.2 mT.

Saint-James and de Gennes [34] discovered the nucleation of superconducting regions in a thin surface sheath at magnetic fields higher than the upper critical magnetic field. Surface superconductivity can be observed in the field range from upper critical field B_{c2} to critical surface field B_{c3}. Such behavior is observed in all considered samples. The value of critical surface field can be determined from the measurement of complex AC susceptibility as a function of external magnetic field.

Such measurement was done for all four samples described in Section 5.2: low temperature baked sample, two nitrogen doped samples and the electro-polished one. Imaginary and real parts of susceptibility measurements are shown in Figures 5.4 and 5.5 respectively.

When external magnetic field reaches the critical value B_{c3}, imaginary part of susceptibility becomes equal to its value in normal conducting state (measured in Section 5.3) and absolute value of real part of susceptibility abruptly drops down to zero.

Both real and imaginary parts are shown in arbitrary units, but they have different normalization. Imaginary part is divided by its value in normal conducting state, such that at external magnetic field higher than B_{c3} normalized value is one. Real part of susceptibility is normalized such that its maximum absolute value is one.

One can see that electro-polished and nitrogen doped samples demonstrate similar behavior, while low temperature baked sample behaves differently. Critical surface field for the sample undergone low temperature bake is significantly higher than for the other samples. It means that unlike low temperature bake, nitrogen doping does not significantly change microscopic parameters of the superconductor surface, such as an electron mean free path.

As shown in [3] the ratio r_{32} between surface critical field and upper critical field depends on the surface preparation but not on the temperature. From presented measurements for low temperature baked sample $r_{32} = 2.6$, which is in agreement with the results presented in [3]. The ratio for other samples $r_{32} = 2.0$ is also in a good agreement with measurements of [3] for electro-polished samples.

5.6 Results

Measurements of magnetization curves and complex AC susceptibility for the niobium samples with different surface treatments including nitrogen doping are presented.

Significant effect of nitrogen doping on the field of first flux penetration into the superconductor is observed. The decreased values of this field are likely the cause of the decreased quench field of SRF cavities produced according to the investigated recipes.

There is no significant effect of nitrogen doping on the critical field B_{c3} observed, which suggests that microscopic parameters such as London penetration depth λ_{L} are not as strongly affected as in the case of the low temperature bake.

CHAPTER 6

HIGH ORDER MODE IMPACT ANALYSIS

6.1 Introduction

As described in Chapter 2.2.2 only one fundamental mode is intentionally excited in a SRF cavity by RF power supply. But a bunch of charged particles passing through the cavity excites all eigenmodes. All modes in the cavity which are not fundamental are called high order modes (HOM) in spite of several of them have lower frequencies compare to the fundamental one. Excitation of the fundamental accelerating mode is compensated, but excitation of HOMs causes the beam power losses.

Along with monopole HOMs the bunch of charged particles excites dipole HOMs. Beam power loss on excitation of dipole modes is negligible compare to the excitation of the monopole ones, but existence of excited dipole HOMs in the cavity leads to effective emittance dilution and in extreme cases may cause beam break-up (BBU).

Significance of HOM impact on beam dynamics depends on a particle beam structure, cavity and accelerator design, and quality factors of HOMs. First parameters usually dictated by the accelerator purpose, but the latter one can be suppressed by HOM dampers. It was discovered at Spallation Neutron Source (SNS) [26], an accelerator-based neutron source facility, that installed HOM dampers may disturb beam dynamics at higher degree compare to HOMs. That is why it is important to estimate the effect of HOMs on beam dynamics to design a particle accelerator. The primary reason for the estimation is to make a conclusion whether HOM dampers are necessary in the design of the accelerator.

The analysis of HOM impact on particle beam dynamics is done for LCLS–II.

6.2 HOM spectrum of ILC cavities

To estimate the effect of HOMs on beam dynamics, it is necessary to calculate the eigenmodes of the cavity. Magnetic field of these modes on the surface of the cavity is necessary to calculate too. Required information can be calculated with CLANS, RF simulation code used for HOM spectrum calculation. Module "clans2" is used for dipole HOM spectrum calculations. The code calculates HOM frequencies and effective impedances: R/Q for monopole (TM_{01}) modes, $R^{(1)}/Q$ for dipole (TE_{11}) modes. The accelerator definition of HOM effective impedance is used for monopole modes:

$$\frac{R}{Q} = \frac{UU^*}{\omega W_0}, \tag{6.1}$$

where U is HOM voltage, ω is its circular frequency, and W_0 is stored energy in the mode. The following definition of the dipole mode effective impedance is used:

$$\frac{R^{(1)}}{Q} = \frac{1}{\omega W_0} \left| \int (\nabla_\perp E_z)|_{x=x_0} \, e^{i\omega z/v} \mathrm{d}z \right|^2, \tag{6.2}$$

where v is beam speed. The integral is taken along the line parallel to the cavity axis at the distance x_0 from the axis.

TESLA-type 9-cell 1.3 GHz elliptical cavity was used in the analysis. Its parameters are described in Section 2.2.2. HOMs can be characterized as trapped or propagating. Trapped HOM field is located within one cavity, while propagating modes transfer energy along the linac. For an infinitely long waveguide with circular cross-section of radius r, cutoff frequency can be defined as the lowest frequency for which a mode propagates in the waveguide. The cutoff frequency is found with the characteristic equation of the Helmholtz equation for electromagnetic waves, which is derived from the electromagnetic wave equation by setting the longitudinal wave number equal to zero and solving for the frequency. For the monopole modes in the infinitely long waveguide with circular cross-section cutoff frequency is given

by

$$f_{\text{cutoff}}^{\text{TM}_{01}} = 2\pi c\frac{\chi_{01}}{r} \approx 2\pi c\frac{2.4048}{r}, \tag{6.3}$$

where χ_{01} is the first root of $J_0(r)$, the Bessel function of the first kind of order 0. For the dipole modes in the same waveguide cutoff frequency is given by

$$f_{\text{cutoff}}^{\text{TE}_{11}} = 2\pi c\frac{\chi_{11}}{r} \approx 2\pi c\frac{1.8412}{r}, \tag{6.4}$$

where χ_{11} is the first root of $J_1(r)$, the Bessel function of the first kind of order 1. For the chain of RF cavities this definition is not valid precisely. The beam pipes between the cavities have finite lengths, which allows even more modes with frequency below the cutoff to propagate.

In spite of the propagating modes are not trapped inside one cavity, they might form a standing wave in the system with multiple cavities. In this case they produce the same effect as the trapped ones, but with smaller quality factor. Probability to meet the conditions for propagating modes to be trapped might not be high, but to address a conservative approach to estimate the upper limit of the HOM effect, both trapped and propagating modes are considered in the analysis.

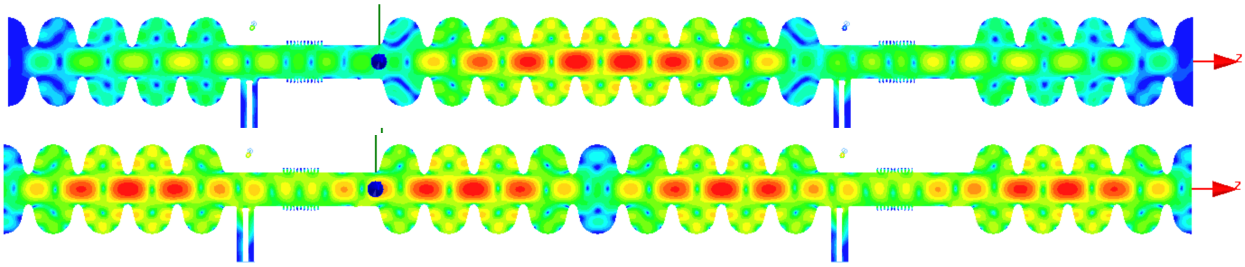

Figure 6.1: Electric field distribution for the mode #1 (top) and #2 (bottom) in the fourth monopole passband of the 1.3 GHz TESLA-type cavity. Mode #1 frequency is 3.3976 GHz, effective impedance R/Q is 0.025 Ω. Mode #2 frequency is 3.4073 GHz, effective impedance R/Q is 0.36 Ω.

For each propagating according to the above conditions mode even within the same passband propagation manner is different. For example, modes #1 and #2 from fourth

passband have less than 10 MHz difference in frequency, but their electric field maps in the chain of cavities differ significantly (see Figure 6.1). Sometimes one mode from a passband can be propagating, but another one is trapped. For instance, monopole mode #7 from the seventh passband is propagating to the beam pipe, while mode #8 is trapped inside each cavity (see Figure 6.2).

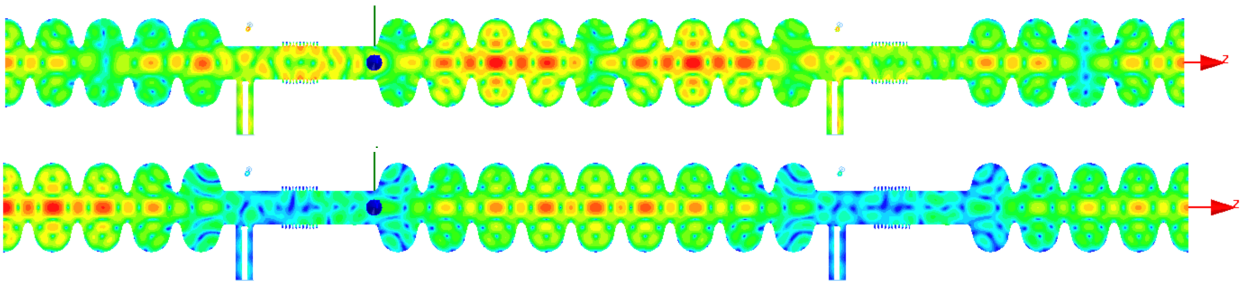

Figure 6.2: Electric field distribution for the mode #7 (top) and #8 (bottom) in the seventh monopole passband of the 1.3 GHz TESLA-type cavity. Mode #7 frequency is 4.7051 GHz, effective impedance R/Q is 0.66 Ω. Mode #8 frequency is 4.7209 GHz, effective impedance R/Q is 5.8 Ω.

Usually modes with higher frequency tend to be propagating, but each mode from eights passband of TESLA-type 1.3 GHz cavity is trapped in a chain of three SRF cavities. Modes parameters are presented in Table 6.1. Electric field maps are shown in Figure 6.3. In rarer cases, propagating modes can be trapped in the beam pipe. The analysis of the effect of these modes is presented in [37], but electric field maps are presented in this work in Figure 6.4. The parameters of these modes are listed in Table 6.2.

Typically only modes with frequencies below cutoff value are considered. The whole HOM spectrum is considered in the given analysis. This makes the analysis unique in considering the effect from propagating modes and vanishes the dependence on inaccuracy of cutoff frequency definitions (6.3) and (6.4). Effective impedance of propagating mode which is trapped depends on location where it is trapped. To analyze this dependence, effective impedance of each mode was calculated at different trapping conditions. It is assumed that the mode is trapped in the region symmetric to the center of the cavity, the extra length of the region is a parameter. The extra length represents how far into the beam pipe the

Table 6.1: Mode parameters of eights monopole passband of the TESLA-type 1.3 GHz cavity (Figure 6.3).

Mode number	Frequency, GHz	Effective impedance R/Q, Ω	Quality factor Q
1	4.8704	0.041	$3.4 \cdot 10^4$
2	4.8722	0.1	$7.7 \cdot 10^4$
3	4.8750	0.028	$7.5 \cdot 10^4$
4	4.8787	0.2	$1.6 \cdot 10^5$
5	4.8829	0.4	$1.1 \cdot 10^5$
6	4.8872	0.069	$1.2 \cdot 10^5$
7	4.8906	0.1	$4.5 \cdot 10^4$
8	4.8926	0.5	$3.8 \cdot 10^4$

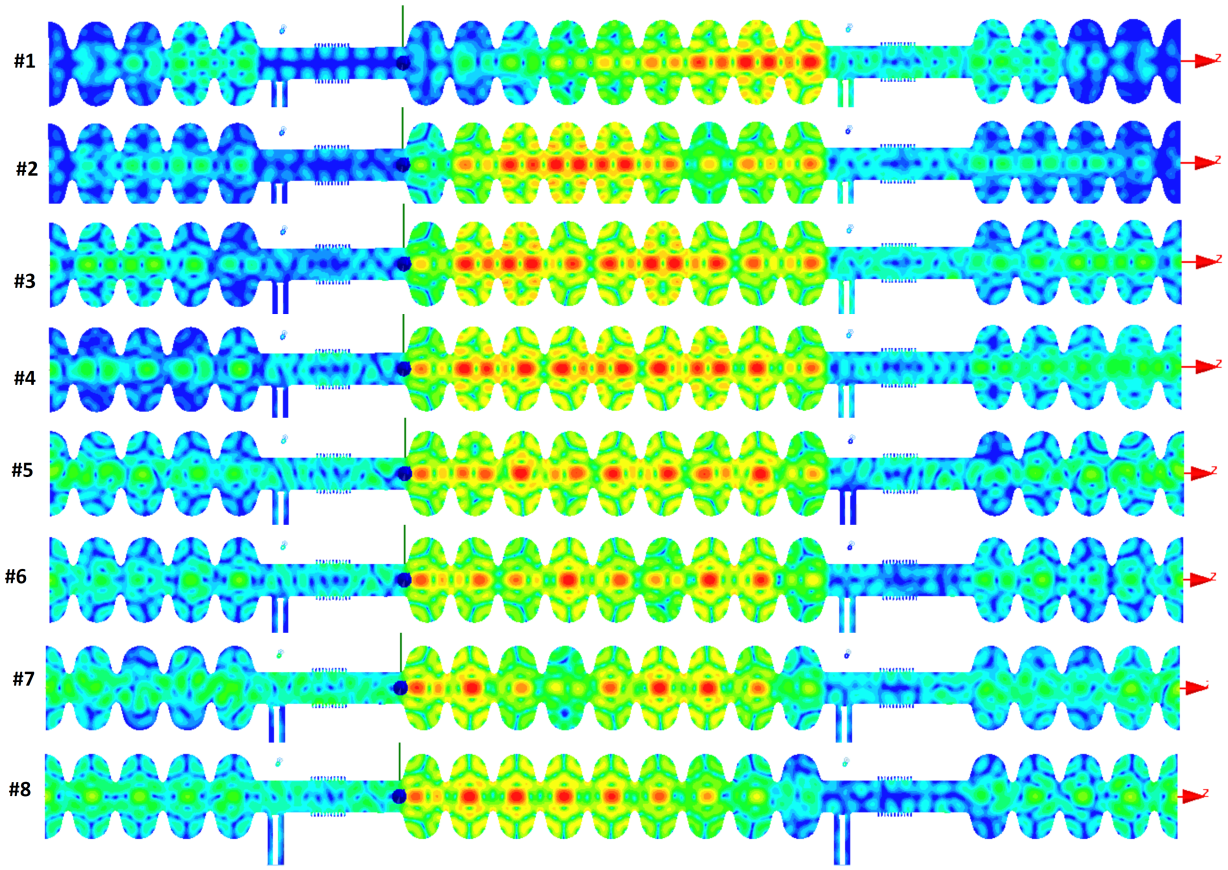

Figure 6.3: Electric field distribution for the modes in the eights monopole passband of the 1.3 GHz TESLA-type cavity. The parameters of the modes are presented in Table 6.1.

mode propagates. Effective impedance of trapped modes does not change with total beam pipe variation (Figures 6.5a and 6.6a), while R/Q and $R^{(1)}/Q$ of propagating modes varies

Table 6.2: The parameters of the monopole modes of TESLA-type 1.3 GHz cavity trapped in the beam pipe at certain conditions (Figure 6.4).

Mode number	Frequency, GHz	Effective impedance R/Q, Ω	Quality factor Q
1	2.734	1.0	$1.8 \cdot 10^3$
2	2.994	2.7	$4.3 \cdot 10^3$
3	3.096	1.0	$1.7 \cdot 10^4$
4	3.202	3.5	$4.8 \cdot 10^3$
5	3.367	0.57	$1.4 \cdot 10^4$
6	3.647	1.3	$1.1 \cdot 10^4$
7	3.693	1.3	$3.2 \cdot 10^3$
8	4.300	0.003	$8.3 \cdot 10^3$
9	4.445	1.4	$5.2 \cdot 10^3$
10	4.811	3.5	$8.7 \cdot 10^3$

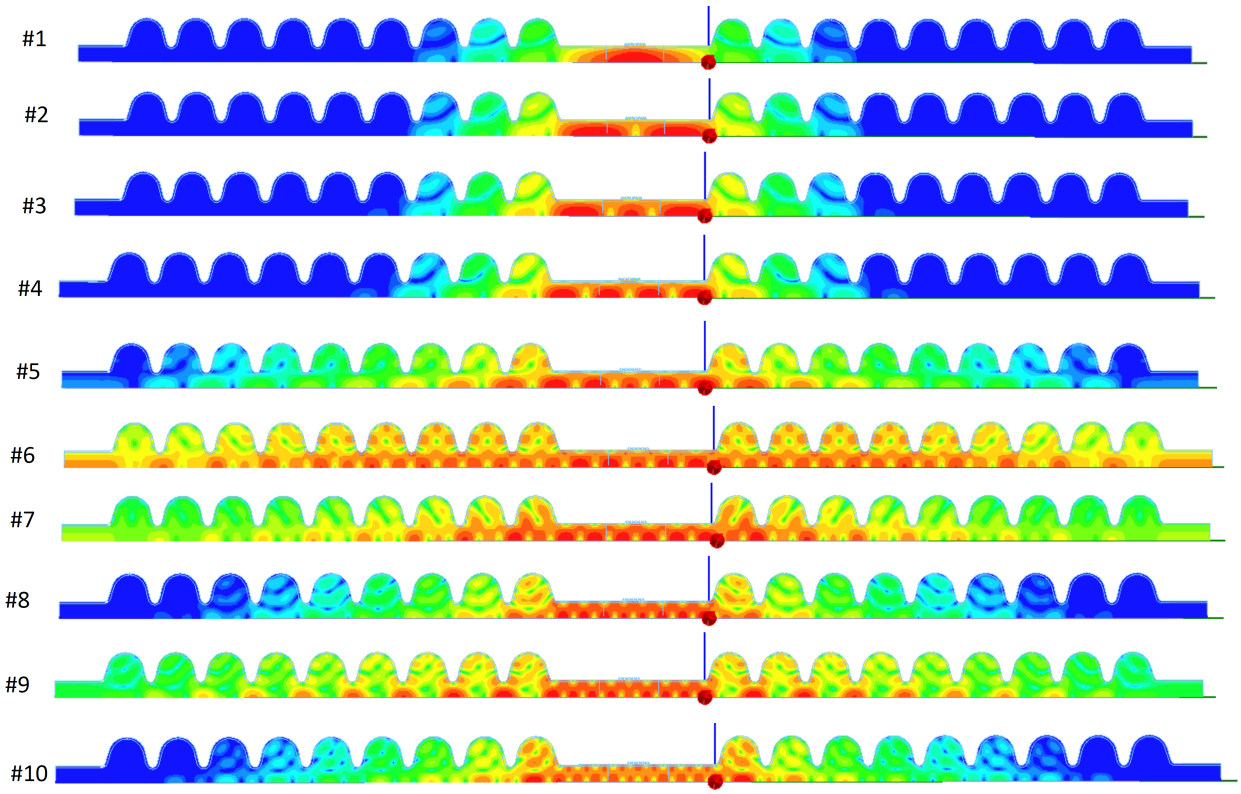

Figure 6.4: Electric field distribution for the monopole modes of the 1.3 GHz TESLA-type cavity trapped in the beam pipe. The parameters of the mode can be found in Table 6.2.

significantly (Figures 6.5b and 6.6b). Figure 6.5 demonstrates R/Q dependence on mode localization for monopole HOM from first passband (trapped modes) and fourth passband

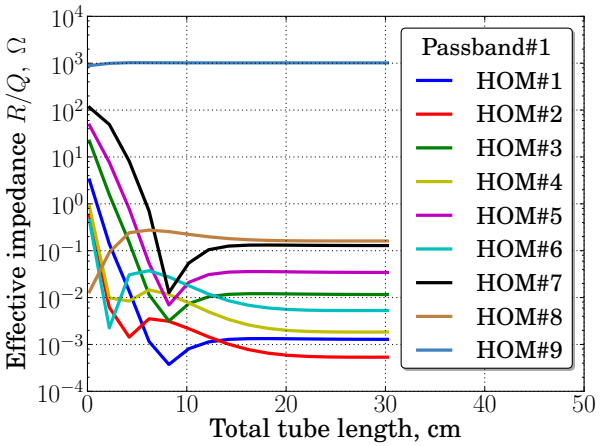

(a) Passband #1: trapped HOMs.

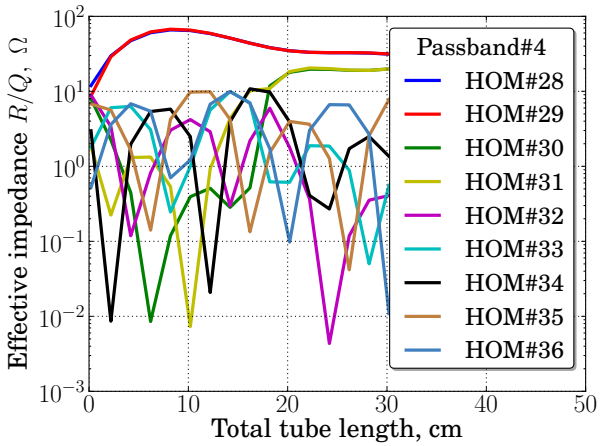

(b) Pasband #4: propagating HOMs.

Figure 6.5: Effective impedance R/Q of monopole modes as a function of location where the modes are trapped.

(propagating modes). Figure 6.6 demonstrates $R^{(1)}/Q$ dependence on mode localization for dipole HOM from first passband (trapped modes) and fourth passband (propagating modes).

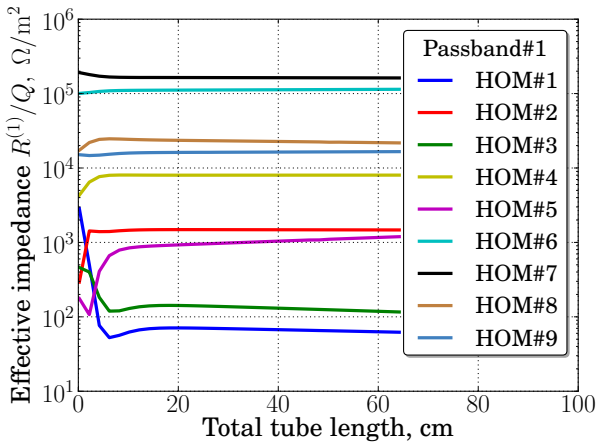

(a) Passband #1: trapped HOMs.

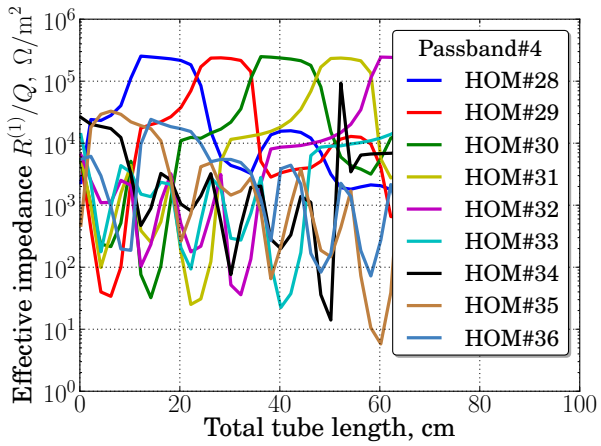

(b) Pasband #4: propagating HOMs.

Figure 6.6: Effective impedance $R^{(1)}/Q$ of dipole modes as a function of location where the modes are trapped.

It is assumed that propagating HOMs are trapped at the worst trapping conditions, i. e. effective impedances have their maximum values. Monopole and dipole HOM spectra calculated under this assumption and shown on Figures 6.7a and 6.8a correspondingly. HOM density as a function of HOM frequency for monopole and dipole modes are shown on

these Figures as well. For both types of modes, the spectrum density increases with HOM frequency linearly, but the effective impedance tends to decrease exponentially.

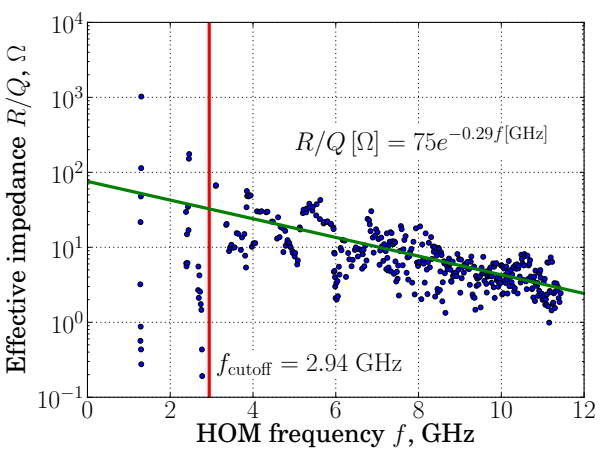

(a) HOM spectrum.

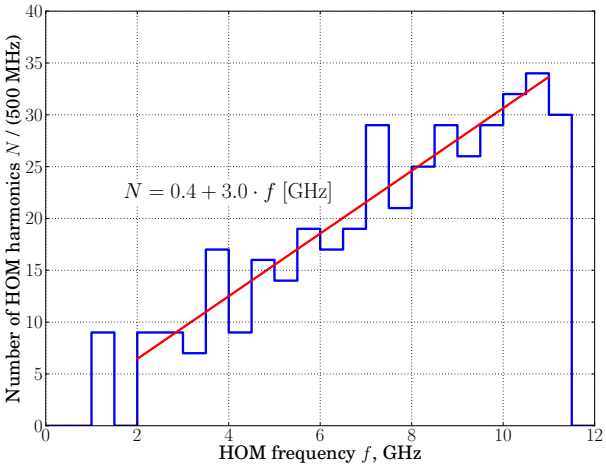

(b) HOM density.

Figure 6.7: Monopole HOM spectrum and density.

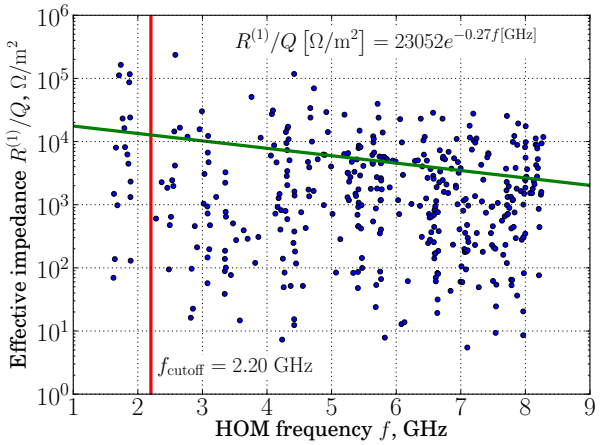

(a) HOM spectrum.

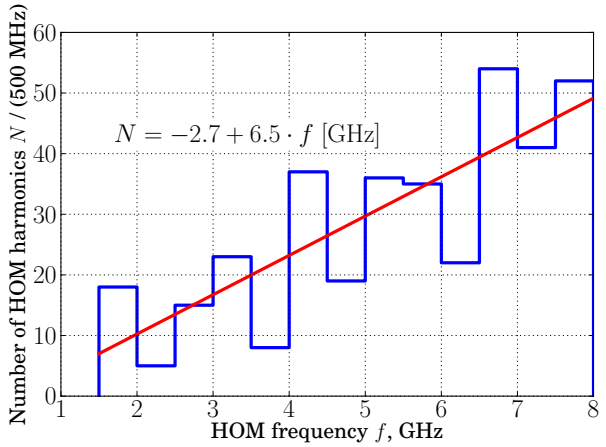

(b) HOM density.

Figure 6.8: Dipole HOM spectrum and density.

Besides, it should be noticed that HOM frequency of trapped modes is constant, while frequency of propagating modes changes significantly with trapping location (see Figure 6.9).

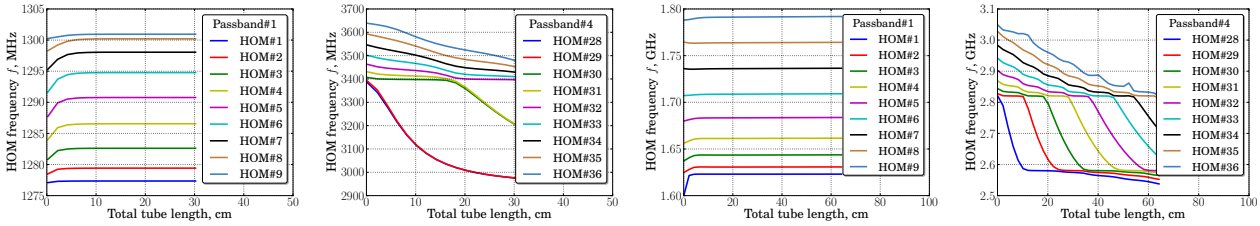

(a) Mono passband #1. (b) Mono passband #4. (c) Dipole passband #1. (d) Dipole passband #4.

Figure 6.9: HOM frequency as a function of HOM localization for monopole and dipole trapped and propagating modes.

6.3 Model assumptions

The model for estimation of resonance excitation of HOMs and BBU effect has been developed in [42]. This model was applied for the Project X CW SRF linac design and estimation of HOM effects in SNS.

As it was mentioned above, the basic feature of the model is a conservative approach to estimate the upper limit of the effect related to HOM. TESLA-type 9-cell cavities with HOM couplers and absorbers providing loaded quality factor $Q_L < 10^7$ are assumed. HOM spectrum calculated in Section 6.2 is used: both trapped and propagating modes are calculated, the worst trapping conditions for propagating modes are assumed. Random variation of HOM frequencies from cavity to cavity with RMS value of $\sigma_f = 1$ MHz is assumed if other is not specified. An idealized beam spectrum (Figure 6.10) is used without time and charge jitter. The charge of the bunches is 300 pC. The bunches follow with frequency of 1 MHz. Bunch size is assumed to be 80 fs ($80 \cdot 10^{-15}$ s). Charge distribution within the bunch is uniform.

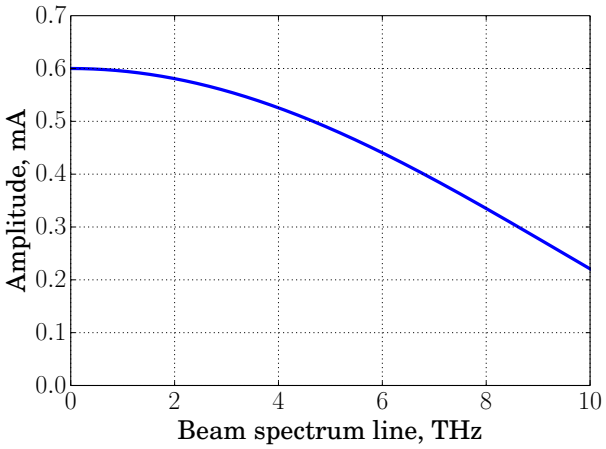

Figure 6.10: Beam spectrum.

6.4 Coherent losses due to HOMs

6.4.1 Calculations

Before starting the calculations, certain notation need to be introduced. $\tilde{I}_n$ is a harmonic of alternating current, $\vec{J}_n$ is density of current of this harmonic, ω_n is its circular frequency. Circular frequencies of cavity eigenmodes are ω_m and ω_p. Q_m and Q_p are quality factors of the modes. $\left\{\vec{E}_m, \vec{H}_m\right\}$ are normalized eigenmodes, $\vec{E}_{nm}$ and $\vec{H}_{nm}$ are electric and magnetic fields of the modes on a certain current harmonic. $\vec{E}^{(n)}$ and $\vec{H}^{(n)}$ are total electric and magnetic fields in the cavity on a certain current harmonic. W_m is normalized value of stored energy, W_{nm} is energy stored by the mode due to a certain current harmonic. U_m is normalized induced voltage, U_{nm} is induced voltage of the mode due to a certain current harmonic.

As demonstrated in [], the fields in the cavity with electric current of density $\vec{J}_n$ at circular frequency ω_n and eigenmodes $\left\{\vec{E}_m, \vec{H}_m\right\}$ can be expressed as the following:

$$\vec{E}^{(n)} = \sum_m \vec{E}_{nm} = \sum_m A_m \vec{E}_m, \qquad \vec{H}^{(n)} = \sum_m \vec{H}_{nm} = \sum_m B_m \vec{H}_m, \tag{6.5}$$

where

$$\begin{aligned} A_m &= \frac{-\omega_n}{i\left(\omega_n^2 - \omega_m^2 - i\frac{\omega_n\omega_m}{Q_m}\right)} \cdot \frac{\oint_V \vec{J}_n \vec{E}_m^* \mathrm{d}V}{\oint_V \vec{H}_m \vec{H}_m^* \mathrm{d}V}, \\ B_m &= \frac{-\omega_m}{i\left(\omega_n^2 - \omega_m^2 - i\frac{\omega_n\omega_m}{Q_m}\right)} \cdot \frac{\oint_V \vec{J}_n \vec{E}_m^* \mathrm{d}V}{\oint_V \vec{H}_m \vec{H}_m^* \mathrm{d}V}. \end{aligned} \tag{6.6}$$

Now let us consider each term in the sums (6.5) separately. In the case of thin beam,

electric field $\vec{E}_m$ can be considered constant in the cross-section of the beam, then

$$\begin{aligned}\oint_V \vec{J}_n \vec{E}_m^* \mathrm{d}V = \int_L \vec{E}_m^* \oint_S \vec{J}_n \mathrm{d}S\mathrm{d}l = \int_L \vec{E}_m^* \vec{\tilde{I}}_n \mathrm{d}l = \\ = \tilde{I}_n \int_{-\infty}^{+\infty} E_{mz}^*(x,y,z) \exp\left[i\left(\frac{kz}{\beta}+\phi\right)\right] \mathrm{d}z = -\tilde{I}_n U_m^*,\end{aligned} \tag{6.7}$$

where phase ϕ is optimal, such as U_m^* is a real number.

Energy stored by the mode can be expressed as

$$\oint_V \vec{H}_m \vec{H}_m^* \mathrm{d}V = 2W_m. \tag{6.8}$$

That is why fields coefficients (6.6) can be written as

$$\begin{aligned}A_m &= \frac{\omega_n}{i\left(\omega_n^2 - \omega_m^2 - i\frac{\omega_n\omega_m}{Q_m}\right)} \cdot \frac{\tilde{I}_n}{2} \cdot \frac{U_m^*}{W_m}, \\ B_m &= \frac{\omega_m}{i\left(\omega_n^2 - \omega_m^2 - i\frac{\omega_n\omega_m}{Q_m}\right)} \cdot \frac{\tilde{I}_n}{2} \cdot \frac{U_m^*}{W_m}.\end{aligned} \tag{6.9}$$

Taking into account the equation $\vec{E}_{nm} = A_m \vec{E}_m$ and integrating it along the beam through the cavity one can write the formula for the voltage, which the beam excites on the cavity at eigenmode $\vec{E}_m$:

$$U_{nm} = A_m U_m = \frac{\omega_n}{i\left(\omega_n^2 - \omega_m^2 - i\frac{\omega_n\omega_m}{Q_m}\right)} \cdot \frac{\tilde{I}_n}{2} \cdot \frac{U_m U_m^*}{W_m}. \tag{6.10}$$

Using the accelerator definition of the mode impedance

$$\left(\frac{R}{Q}\right)_m = \frac{U_m U_m^*}{\omega_m W_m} = \frac{U_{nm} U_{nm}^*}{\omega_m W_{nm}}, \tag{6.11}$$

one can rewrite the formula (6.10) as the following:

$$U_{nm} = \frac{\omega_n \omega_m}{i\left(\omega_n^2 - \omega_m^2 - i\frac{\omega_n \omega_m}{Q_m}\right)} \cdot \frac{\tilde{I}_n}{2} \cdot \left(\frac{R}{Q}\right)_m, \tag{6.12}$$

and then get the ratio

$$\frac{|U_{nm}|}{|U_m|} = \sqrt{\frac{W_{nm}}{W_m}} = \sqrt{\frac{U_{nm}^2}{\omega_m (R/Q)_m W_m}}. \tag{6.13}$$

Any magnetic field vector $\vec{H}_{nm}$ can be expressed as

$$\vec{H}_{nm} = \left|\vec{H}_{nm}\right| e^{i \arg\left(\vec{H}_{nm}\right)} \vec{a}, \tag{6.14}$$

where $\vec{a}$ is a unit vector. The magnitude of magnetic field can be expressed using (6.5) as the following:

$$\left|\vec{H}_{nm}\right| = \left|B_m \vec{H}_m\right| = \left|\frac{\omega_m}{\omega_n^2 - \omega_m^2 - i\frac{\omega_n \omega_m}{Q_m}} \cdot \frac{\tilde{I}_n}{2} \cdot \frac{U_m^*}{W_m} \cdot \vec{H}_m\right|. \tag{6.15}$$

It follows from Equation (6.10) that

$$\left|\frac{\omega_m}{\omega_n^2 - \omega_m^2 - i\frac{\omega_n \omega_m}{Q_m}} \cdot \frac{\tilde{I}_n}{2} \cdot \frac{U_m^*}{W_m}\right| = \left|\frac{U_{nm}}{\omega_n U_m}\right|. \tag{6.16}$$

Then also taking into account Equation (6.13), one can write

$$\begin{aligned} \left|\vec{H}_{nm}\right| &= \left|\frac{\omega_m}{\omega_n} \cdot \frac{U_{nm}}{U_m} \cdot \vec{H}_m\right| = \frac{\omega_m}{\omega_n} \sqrt{\frac{U_{nm}^2}{\omega_m (R/Q)_m W_m}} \left|\vec{H}_m\right| = \\ &= \frac{1}{\sqrt{(R/Q)_m W_m}} \cdot \frac{\sqrt{\omega_m}}{\omega_n} \cdot |U_{nm}| \cdot \left|\vec{H}_m\right|. \end{aligned} \tag{6.17}$$

As U_m and U_m^* are real numbers

$$\arg\left(\vec{H}_{nm}\right) = \arg\left[\frac{1}{i\left(\omega_n^2 - \omega_m^2 - i\frac{\omega_n\omega_m}{Q_m}\right)}\right] = \arg\left(U_{nm}\right). \tag{6.18}$$

Finally,

$$\vec{a} = \frac{\vec{H}_m}{\left|\vec{H}_m\right|}. \tag{6.19}$$

Now one can write the equation for magnetic field using (6.14), (6.17), (6.18), and (6.19):

$$\begin{aligned}\vec{H}_{nm} &= \frac{1}{\sqrt{(R/Q)_m W_m}} \cdot \frac{\sqrt{\omega_m}}{\omega_n} \cdot |U_{nm}| \cdot \left|\vec{H}_m\right| \cdot e^{i\arg(U_{nm})} \cdot \frac{\vec{H}_m}{\left|\vec{H}_m\right|} \\ &= \frac{1}{\sqrt{(R/Q)_m W_m}} \cdot \frac{\sqrt{\omega_m}}{\omega_n} \cdot U_{nm}\vec{H}_m.\end{aligned} \tag{6.20}$$

Applying Equation (6.12) for HOM voltage to the magnetic field equation, one can get

$$\vec{H}_{nm} = \frac{\omega_m\sqrt{\omega_m}}{i\left(\omega_n^2 - \omega_m^2 - i\frac{\omega_n\omega_m}{Q_m}\right)} \cdot \frac{\tilde{I}_n}{2\sqrt{W_m}} \cdot \sqrt{\left(\frac{R}{Q}\right)_m} \cdot \vec{H}_m. \tag{6.21}$$

Note, that there is a factor $\sqrt{\omega_m}$ because of normalization on stored energy.

Assume that the beam spectrum is

$$\tilde{I}(\omega) = \sum_n \tilde{I}_n \delta\left(\omega - \omega_n\right), \tag{6.22}$$

where ω_n is current frequency. Monopole HOM spectrum is calculated for ILC cavities. Magnetic field on the surface of the cavity $H_m(z)$ for each mode is calculated for stored energy $W_m = W_0 = 1$ mJ using CLANS.

Let us separate the terms which depend on HOM frequency, longitudinal coordinate in the cavity, and the terms which do not depend on these parameters in Equation (6.21). After

doing this, one can write the magnetic field on the surface of the cavity as the following:

$$\begin{aligned} H_{nm}(z) &= -iH_m(z) \cdot \frac{\tilde{I}_n}{2\sqrt{W_0}} \cdot \sqrt{\left(\frac{R}{Q}\right)_m} \cdot \frac{\omega_m \sqrt{\omega_m}}{\omega_n^2 - \omega_m^2 - i\frac{\omega_n \omega_m}{Q_m}} = \\ &= -iC_{nm} f_{nm} H_m(z), \end{aligned} \tag{6.23}$$

where the following notation is used:

$$C_{nm} = \frac{\tilde{I}_n}{2\sqrt{W_0}} \sqrt{\left(\frac{R}{Q}\right)_m}, \qquad f_{nm} = \frac{\omega_m \sqrt{\omega_m}}{\omega_n^2 - \omega_m^2 - i\frac{\omega_n \omega_m}{Q_m}}. \tag{6.24}$$

One can see that only term f_{nm} depends on HOM frequency, and only term $H_m(z)$ depends on the longitudinal coordinate. Taking into account all modes (Equation (6.5)) and whole current spectrum (Equation (6.22)), the power of losses on HOM excitation can be expressed as

$$\begin{aligned} P &= \sum_n \frac{1}{2} R_n \oint \vec{H}^{(n)} \, \vec{H}^{(n)\,*} \, \mathrm{d}s = \\ &= \sum_n \frac{1}{2} R_n \oint \left(\sum_m -iC_{nm} f_{nm} H_m(z) \right) \left(\sum_p -iC_{np} f_{np} H_p(z) \right)^* \mathrm{d}s, \end{aligned} \tag{6.25}$$

where R_n is surface resistance. It consists of two terms: residual and BCS resistance:

$$R_n = R_{\text{residual}} + R_{\text{BCS}}^{(n)}. \tag{6.26}$$

For calculations in this chapter to get the upper estimate on HOM effects upper estimates of resistance components are used:

$$R_{\text{residual}} = 10 \text{ n}\Omega, \tag{6.27}$$

$$R_{\text{BCS}}^{(n)} \, [\Omega] = \frac{2 \cdot 10^{-4}}{T \, [\text{K}]} \left(\frac{f_n \, [\text{GHz}]}{1.5} \right)^2 \exp\left(-\frac{17.67}{T \, [\text{K}]} \right) \tag{6.28}$$

(see [36]), where f_n is the frequency of the beam spectrum line, T is the cavity temperature:

$$T = 2 \text{ K}. \tag{6.29}$$

Now as C_{nk} and f_{nk} do not depend on the longitudinal coordinate, one can rewrite the integral (6.25):

$$\begin{aligned} P &= \sum_n \frac{1}{2} R_n \oint \sum_m C_{nm} f_{nm} H_m(z) \cdot \sum_p C_{np} f_{np}^* H_p(z) \mathrm{d}s = \\ &= \sum_n \frac{1}{2} R_n \oint \sum_m \sum_p C_{nm} C_{np} f_{nm} f_{np}^* H_m(z) H_p(z) \mathrm{d}s = \\ &= \sum_n \frac{1}{2} R_n \sum_m \sum_p C_{nm} C_{np} f_{nm} f_{np}^* \oint H_m(z) H_p(z) \mathrm{d}s. \end{aligned} \tag{6.30}$$

Let us introduce the new notation to simplify the equation:

$$C_{nm} C_{np} = B_{nmp} = \left(\frac{\tilde{I}_n}{2} \right)^2 \frac{1}{W_0} \sqrt{\left(\frac{R}{Q} \right)_m \left(\frac{R}{Q} \right)_p}, \tag{6.31}$$

$$\oint H_m(z) H_p(z) \mathrm{d}s = A_{mp}, \tag{6.32}$$

then the equation for the power of losses looks like

$$\begin{aligned} P &= \sum_n \frac{1}{2} R_n \sum_m \sum_p B_{nmp} A_{mp} \cdot f_{nm} f_{np}^* = \sum_n \sum_m \sum_p \frac{1}{2} R_n B_{nmp} A_{mp} \cdot f_{nm} f_{np}^* = \\ &= \sum_n \sum_m \sum_p a_{nmp} f_{nm} f_{np}^*, \end{aligned} \tag{6.33}$$

where a new parameter introduced:

$$a_{nmp} = \frac{1}{2} R_n B_{nmp} A_{mp}. \tag{6.34}$$

This parameter depends on the beam spectrum, HOMs impedances and magnetic field of

eigenmodes on the surface of the cavity. Let us consider HOM frequency dependent term:

$$f_{nm}f_{np}^{*} = \frac{\omega_m^{3/2}\omega_p^{3/2}}{\left(\omega_n^2 - \omega_m^2 - i\frac{\omega_n\omega_m}{Q_m}\right)\left(\omega_n^2 - \omega_p^2 + i\frac{\omega_n\omega_p}{Q_p}\right)}. \tag{6.35}$$

If $m = p$, then

$$f_{nm}f_{np}^{*} = f_{nm}f_{nm}^{*} = \frac{\omega_m^3}{\left(\omega_n^2 - \omega_m^2\right)^2 + \frac{\omega_n^2\omega_m^2}{Q_m^2}}, \tag{6.36}$$

otherwise

$$\begin{aligned} f_{nm}f_{np}^{*} + f_{np}f_{nm}^{*} &= 2\mathrm{Re}\left(f_{nm}f_{np}^{*}\right) = \\ &= 2\mathrm{Re}\left[\frac{\omega_m^{3/2}\omega_p^{3/2}}{\left(\omega_n^2 - \omega_m^2 - i\frac{\omega_n\omega_m}{Q_m}\right)\left(\omega_n^2 - \omega_p^2 + i\frac{\omega_n\omega_p}{Q_p}\right)}\right]. \end{aligned} \tag{6.37}$$

Notice that $a_{nmp} = a_{npm}$, then the power of losses from Equation (6.33):

$$P = \sum_n\sum_m a_{nmm}f_{nm}f_{nm}^{*} + \sum_n\sum_m\sum_{p<m} 2a_{nmp}\mathrm{Re}\left(f_{nm}f_{np}^{*}\right). \tag{6.38}$$

Now let us go back to A_{mp} definition (Equation (6.32)). The SRF cavities for LCLS-II are axial symmetric, that is why the integration over the surface can be replaced with the integration over the length of the border of the cavity's axial cross-section by introducing

$$\mathrm{d}s = 2\pi r(l)\mathrm{d}l, \tag{6.39}$$

where l is a new integration variable, r is the distance from the surface of the cavity to its axis at a given point. Applying Equation (6.39) to Equation (6.32), one can write:

$$A_{mp} = \oint H_m(z)H_p(z)\mathrm{d}s = \int_0^L 2\pi r(l)H_m(l)H_p(l)\mathrm{d}l, \tag{6.40}$$

where L is the length of the border of the cavity's axial cross-section.

Finally, there is Equation (6.38) for the power of HOM losses calculation, and it is known how to calculate each term in this equation.

6.4.2 Estimations

Remember that the losses on excitation of the fundamental mode are compensated, that is why there are no terms

$$\sum_n a_{n\mu\mu} f_{n\mu} f^*_{n\mu} \tag{6.41}$$

in the Equation (6.38), where μ is the consecutive number of the fundamental mode. Thus, the Equation (6.38) can be rewritten as the following:

$$\begin{aligned} P &= \sum_n \sum_{m\neq\mu} a_{nmm} f_{nm} f^*_{nm} + \sum_n \sum_{m\neq\mu} \sum p < m 2 a_{nmp} \mathrm{Re}\left(f_{nm} f^*_{np}\right) = \\ &= \sum_n \sum_{m\neq\mu} a_{nmm} f_{nm} f^*_{nm} + \sum_n \sum_{m\neq\mu} \sum_{\substack{p<m \\ p\neq\mu}} 2 a_{nmp} \mathrm{Re}\left(f_{nm} f^*_{np}\right) + \\ &+ \sum_n \sum_{m\neq\mu} 2 a_{nm0} \mathrm{Re}\left(f_{nm} f^*_{n0}\right). \end{aligned} \tag{6.42}$$

Let us introduce new parameters:

$$\begin{aligned} P_2 &= \sum_n \sum_{m\neq\mu} a_{nmm} f_{nm} f^*_{nm}, \\ P_1 &= \sum_n \sum_{m\neq\mu} \sum_{\substack{p<m \\ p\neq\mu}} 2 a_{nmp} \mathrm{Re}\left(f_{nm} f^*_{np}\right), \\ P_0 &= \sum_n \sum_{m\neq\mu} 2 a_{nm0} \mathrm{Re}\left(f_{nm} f^*_{n0}\right). \end{aligned} \tag{6.43}$$

Parameter P_2 includes diagonal terms only. It represents the value of losses due to an HOM itself. P_0 includes cross-terms with the fundamental mode. P_1 includes the rest of cross-terms. These are integrals of product of eigen-functions of different modes. It is clear that $P = P_2 + P_1 + P_0$, but calculation of the term P_1 is CPU-time consuming. That is why

initially the research on comparison of each term values was performed using the design of Project X linac.

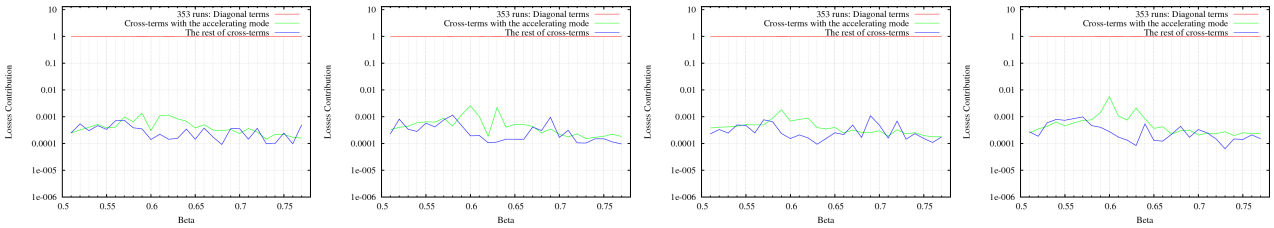

Figure 6.11: Losses contribution from terms P_2, P_1, P_0 at LE650 section of Project X linac as a function of particle's speed. Quality factor values are 10^7, 10^8, 10^9 and 10^{10} for each plot correspondingly.

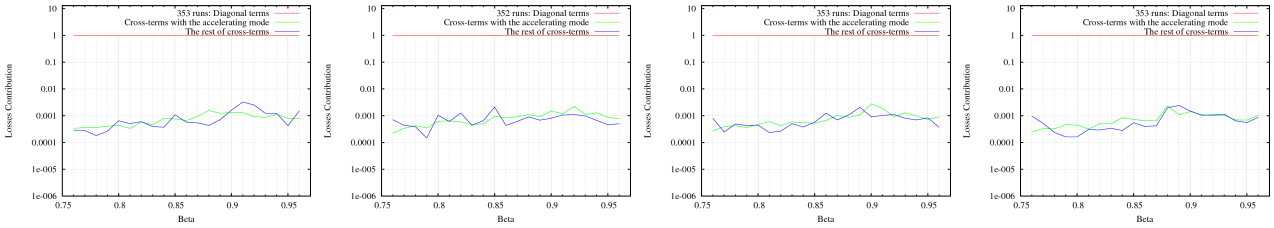

Figure 6.12: Losses contribution from terms P_2, P_1, P_0 at HE650 section of Project X linac as a function of particle's speed. Quality factor values are 10^7, 10^8, 10^9 and 10^{10} for each plot correspondingly.

Losses contributions are defined as

$$\delta_i = \frac{P_i}{P}, \qquad i = 0, 1, 2. \tag{6.44}$$

Results for sections LE650 and HE650 and values of HOM quality factor of 10^7, 10^8, 10^9 and 10^{10} are shown in Figures 6.11 and 6.12. About 350 different sets of HOMs were simulated for each value of beta. Losses contributions are calculated for each set. Maximum values of contributions by cross-terms with the fundamental mode and the rest of cross-terms are shown on the figures in green and blue lines. For diagonal terms minimum values is calculated. It is shown on the figures in red lines.

It is clear that even the maximum value of losses contribution by cross-terms is always less than 0.01, and the minimum value of δ_2 is equal to 1 with very good accuracy. It means

that $P_2 \gg P_1$ and $P_2 \gg P_0$, that is why the power of losses can be calculated as

$$P = P_2 + P_1 + P_0 \approx P_2 = \sum_n \sum_{m \neq \mu} a_{nmm} f_{nm} f_{nm}^* \tag{6.45}$$

with the error of less than 1%.

6.4.3 Analysis

HOMs with high loaded quality factor Q_L may be coherently excited by CW bunched beam. If HOM is excited on frequency close to the resonance one, the effect may be significantly higher than the incoherent losses. That is why this effect is called resonance excitation.

Bunche repetition rate of 1 MHz results in the dense beam spectrum (Figure 6.10) containing lines close to each HOM: each HOM is not further from a beam spectrum line than 500 kHz.

Because of short electron bunches (80 ps), beam spectrum is very long (see Figure 6.10). Some HOMs are absorbed by HOM dampers, but some of them are propagating. In the periodic structure of SRF cavities the certain conditions may be realized when HOMs with frequency above the beam pipe cutoff (6.3) will be trapped inside cavities. These two facts require to consider the effect from each part of the beam spectrum up to high frequencies to understand the impact from the propagating modes.

As shown in Sections 6.4.1 and 6.4.2, the loss power caused by mth HOM and nth beam spectrum line interaction can be calculated as

$$P_{mn} = \frac{1}{W_0} \frac{R_n}{2} \left(\frac{I_n}{2} \right)^2 \left(\frac{R}{Q} \right)_m A_m G_{mn}, \tag{6.46}$$

where W_0 is HOM stored energy, R_n is cavity surface resistance (6.26) corresponding to the beam spectrum line frequency f_n and cavity temperature $T = 2$ K, I_n is the beam spectrum line amplitude, $(R/Q)_m$ is effective impedance of HOM, A_m is the surface integral (6.40) of

HOM magnetic field:

$$A_m = A_{mm} = \oint_S |H_m|^2 \, \mathrm{d}s, \tag{6.47}$$

and G_{mn} is a resonance factor:

$$G_{mn} = \frac{1}{2\pi} \cdot \frac{f_m^3}{\left(f_m^2 - f_n^2\right)^2 + \left(\frac{f_m f_n}{Q_m}\right)^2}, \tag{6.48}$$

where f_m is HOM frequency, f_n is the beam spectrum line frequency, Q_m is HOM loaded quality factor. Total loss power per cavity can be calculated as the following:

$$P = \sum_m \sum_n P_{mn}. \tag{6.49}$$

Each HOM frequency f_m changes from cavity to cavity and can be considered as normal distributed random variable $f_m \sim N(f_m^*, \sigma_f^2)$, where f_m^* is HOM frequency for designed cavity geometry without error. Total loss power per cavity is also a random variable as it depends on f_m, $m = 1, 2, ...$

To find probability density function (pdf) of random variable P, a sample of HOM frequencies with known normal distribution was generated: $\{\{f_m\}_k\}_{k=1}^{k=K}$, where K is sample size. HOM frequency standard error is chosen to be independent of HOM frequency: $\sigma_f =$ 1 MHz. Sample size is about 10,000. For each set of $\{f_m\}_k$ from the sample total loss power $P_{mn}^{(k)}$ was calculated according to the above equations. Distribution of values $P_{mn}^{(k)}$ represents pdf of total loss power per cavity. HOM loaded quality factor was considered to be independent on HOM frequency and equals $Q_L = 10^7$. Total loss power distribution is shown in Figure 6.13.

All propagating modes are assumed to be trapped. This is an extreme situation, but even in this case the mean loss power is of the order of 1 mW per cavity when all monopole HOMs with frequency below 11 GHz are considered.

Even the expected loss power is low, it is important to estimate the probability for HOM

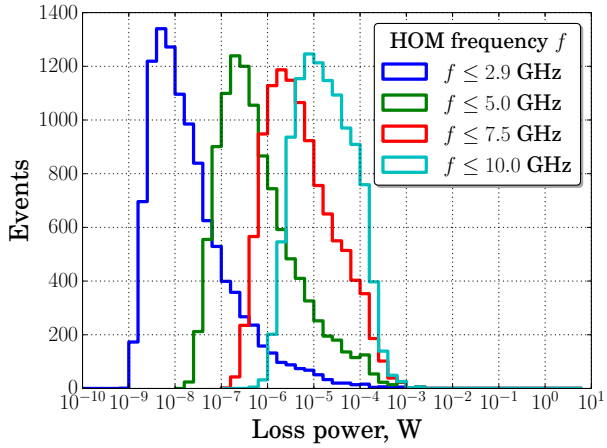

Figure 6.13: Distribution of loss power caused by HOMs in case of HOM frequency spread of 1 MHz and loaded quality factor of 10^7. 10,832 cavities with random HOM frequencies are generated. Distributions for four sets of HOM are presented: trapped modes, trapped and propagating modes with frequency below 5 GHz, 7.5 GHz and 10 GHz. Even taking into account all HOMs with frequency up to 10 GHz, there are no cases of cavity causing loss power over 0.1 W. All propagating modes are assumed to be trapped in worst possible conditions.

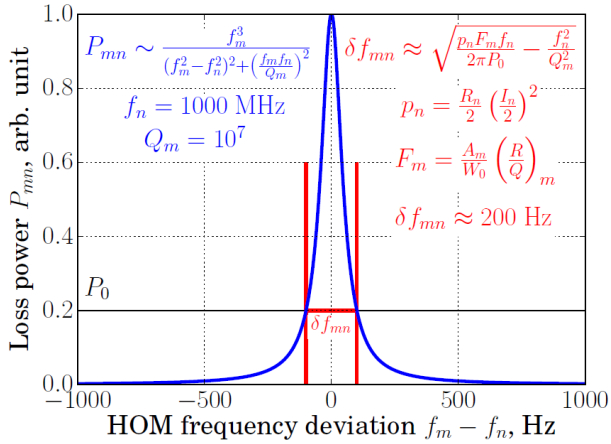

Figure 6.14: Loss power due to single HOM caused by single beam spectrum line as a function of HOM frequency. Theoretical example, not actual values used. Beam spectrum line frequency is $f_n = 1000$ MHz. HOM loaded quality factor $Q_L = 10^7$. Significant loss power threshold is chosen to be 20% of loss power maximum. HOM frequency dangerous interval size is $\delta f_{mn} = 200$ Hz. An example of δf_{mn} distribution is shown on Fig. 6.15.

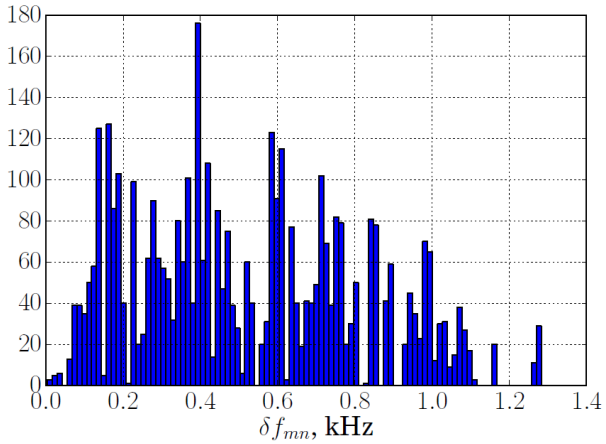

Figure 6.15: Distribution of frequency interval around each beam spectrum line δf_{mn} within which HOM would cause loss power over 10 mW.

to cause significant loss power. Let us consider an HOM with central frequency f_m excited by a beam spectrum line of frequency f_n. If HOM frequency is in a "dangerous" interval, loss power $P_{mn} > P_0$, where P_0 is significant loss power (Figure 6.14). As derived in [42], "dangerous" HOM frequency interval size is

$$\delta f_{mn} \approx \mathrm{Re}\sqrt{\frac{R_n}{4\pi}\left(\frac{I_n}{2}\right)^2 \frac{A_m}{W_0}\left(\frac{R}{Q}\right)_m \frac{f_n}{P_0} - \frac{f_n^2}{Q_m^2}}. \tag{6.50}$$

HOM frequency $f_m \sim N(f_m^*, \sigma_f^2)$, that is why probability for the given HOM to cause loss power over P_0 is

$$w_m = \sum_n \frac{\delta f_{mn}}{\sqrt{2\pi}\sigma_f} \cdot \exp\left[-\frac{(f_m^* - f_n)^2}{2\sigma_f^2}\right]. \tag{6.51}$$

Cumulative probability to cause loss power P_0 is probability that at lease one of the considered HOMs causes this value of loss power. It can be calculated as

$$w = 1 - \prod_m (1 - w_m). \tag{6.52}$$

Cumulative probability as a function of loss power is shown in Figure 6.16. One can see that this probability goes down to zero before $P_0 = 1$ W. As far as expected quality factors

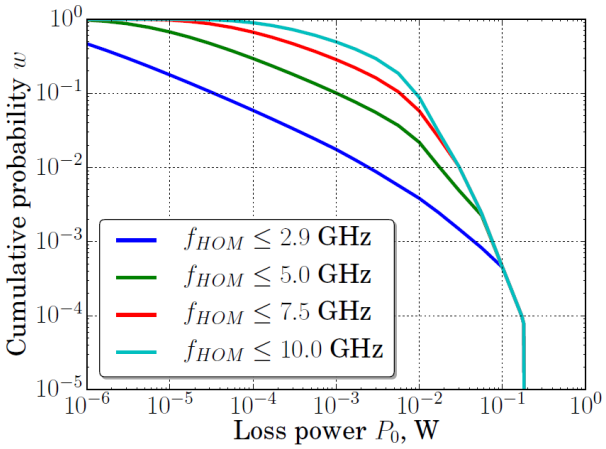

Figure 6.16: Cumulative probability to cause certain loss power as a function of loss power. HOM frequency spread is 1 MHz and loaded quality factor is 10^7. When more HOM included into consideration the probability goes up, but even in the case when all HOM with frequency up to 10 GHz are taken into account probability for at lease one mode to cause loss power over 0.2 W is zero. All propagating modes are assumed to be trapped in worst possible conditions.

are below 10^7, probability to have significant coherent HOM losses is extremely small.

Nevertheless, if this situation happens with a cavity it is shown in [42] that there is a technique which allows to shift HOM frequencies by the order of 100 kHz by detuning of the fundamental mode and tuning it back. Shift of 100 kHz is enough to move an HOM from a dangerous region (Figure 6.15), but small enough to not make it close to another beam spectrum line.

6.5 Cumulative HOM excitation

A bunch of charged particles passing through an SRF cavity excites dipole HOMs if displaced from the cavity axis. Excited HOMs with high quality factor store the energy long enough to affect the following bunches motion. Therefore each of the following bunches experience a transverse kick from HOM field and produce additional excitation of HOMs. As the result, the bunches change their angular components of motion, which causes effective transverse emittance dilution or may cause even beam break-up.

HOM voltage ΔU induced by a single bunch passing through a cavity can be calculated as

$$\Delta U = \frac{i}{2} c q_b \frac{R^{(1)}}{Q}(x - x^*), \tag{6.53}$$

where q_b is bunch charge, x is bunch position along x-axis, x^* is cavity misalignment along x-axis. When there are no bunches passing through the cavity, HOM voltage oscillates with time:

$$U(t) = U(0) \exp\left(i\omega_m t - \frac{\omega_m t}{2Q}\right), \tag{6.54}$$

where $\omega_m = 2\pi f_m$ is HOM circular frequency. Transverse kick on a bunch by HOM voltage U is

$$\Delta x' = \frac{e\mathrm{Re}\,(U)}{pc}. \tag{6.55}$$

HOM frequency itself does not affect the value of emittance dilution, but its difference with the closest beam spectrum line does. LCLS–II beam spectrum is regular (a line every 1 MHz), that is why distance from HOM to the closest beam spectrum line may vary from 0 (resonance case) to 500 kHz.

6.5.1 Emittance dilution

Simulation of the whole linac is performed to estimate BBU effect. Different HOM frequency spread from 1 Hz to 10 MHz is considered in this simulation. Note that actual HOM frequency spread is expected to be about 1 MHz, but the whole range of the spread is considered to demonstrate the dependence of the effect on the HOM frequency spread. For each value of the spread a set of linacs is simulated and effective transverse emittance dilution is calculated. Emittance dilution caused by HOM effects is taken into account. This emittance is compared to the designed bunch emittance. Relative effective transverse emittance is defined as a ratio of the actual effective transverse emittance to the design transverse emittance of the bunches.

Relative effective transverse emittance dilution due to a dipole HOM as a function of

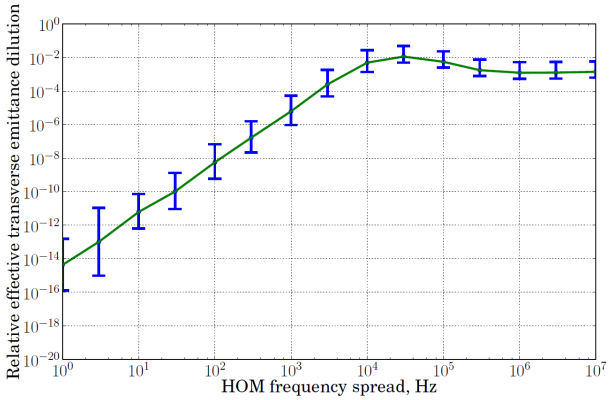

Figure 6.17: Relative effective transverse emittance dilution due to dipole HOM as a function of HOM frequency spread for the resonant case.

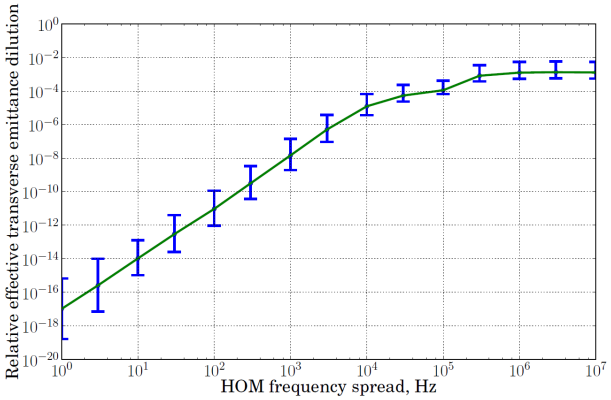

Figure 6.18: Relative effective transverse emittance dilution due to dipole HOM as a function of HOM frequency spread for the non-resonant case.

HOM frequency spread for two extreme cases (resonance and the farthest from the resonance) is shown in Figures 6.17 and 6.18 respectively. For the resonant case (Figure 6.17) emittance dilution goes to zero when HOM frequency spread goes to zero. This can be explained considering the extreme case when HOM frequency spread is zero. The first bunch passing through each cavity induces HOM voltage according to the Equation (6.53). HOM voltage oscillates according to the Equation (6.54) and as far as the case is resonant and HOM frequency spread is zero $\omega_m t = 2\pi n$, which means that when the next bunch is passing the cavity HOM frequency has imaginary value and does not provide any transverse kick to the bunch (see Equation (6.55)). Thus none of the bunches experience transverse motion disturbance due to HOM and emittance dilution is zero. The resonant case has a maximum of emittance dilution when frequency spread is equal to f_{HOM}/Q, which is 20 kHz for considered values. For the non-resonant case emittance dilution monotonic increase is explained by increase of probability for HOM frequency to be close enough to the beam spectrum line. There is a significant jump in emittance dilution at about 0.5 MHz related to the distance between the central HOM frequency and closest beam spectrum line.

One can see that even for the worst case scenario effective transverse emittance dilution due to dipole HOM is less than 10% of the initial transverse emittance. This scenario is

realized at HOM frequency spread of 20 kHz, which is far enough from the expected 1 MHz frequency spread. For actual value of HOM frequency spread expected relative emittance dilution is about 0.1%, which is negligible.

6.5.2 Transition effect

For electron beam deflection between two undulators in LCLS-II, the beam will shift to another RF bucket, thus RF deflector (operating at 325 MHz frequency) will shift the beam by 180 degrees (or 90 degrees if the beam will be sent to the damp line). Besides, single bunches periodically can be deflected for diagnostic purposes. In both cases beam phase suddenly changes. BBU transition effects due to sudden beam phase change is considered in this section.

Expected beam phase shift is 90 or 180 degrees of 325 MHz frequency (in case of shift to another RF bucket) and 360 degrees of 1 MHz frequency (in diagnostic case). As demonstrated in [41], HOM central frequency cannot be determined precisely (see Figure 6.9d), that is why effective HOM phase shift can have different values. The most significant effect is observed when HOM phase shift is 180 degrees of HOM frequency. Various HOM phase shift frequency is considered to estimate allowed frequency of diagnostic bunch extraction.

In the situation when there is no transition effect and all bunches follow each other with constant time interval of 1 μs transverse coordinate of each bunch at the exit of the linac is presented in Figure 6.19a. There is some transverse coordinate variation (up to 80 mum) in the first bunches, but after 5 ms it goes to zero. When there is a sudden change of HOM phase by 180 degrees, real and imaginary parts of induced HOM voltage are swapped (see Equation (6.54)). Thus, each of the following bunches experience unexpected transverse kick which results in additional bunch transverse coordinate variation as demonstrated on Figure 6.19b. The variation from transition effect can be even greater than variation in the first bunches (130 μm compare to 80 μm for considered case).

The results of the simulation of periodic transition effect is shown in Figure 6.19c for

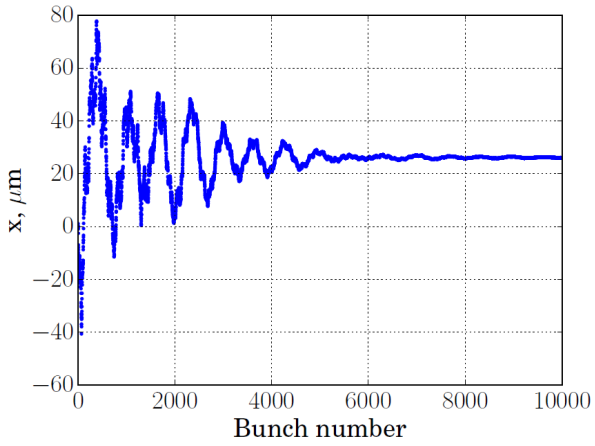

(a) HOM phase shift is off.

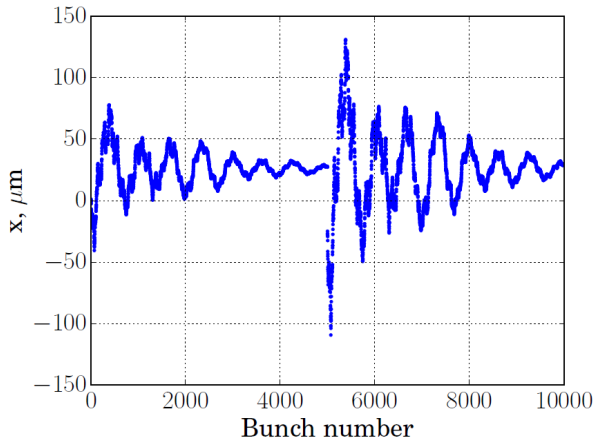

(b) Sudden HOM phase shift by 180°.

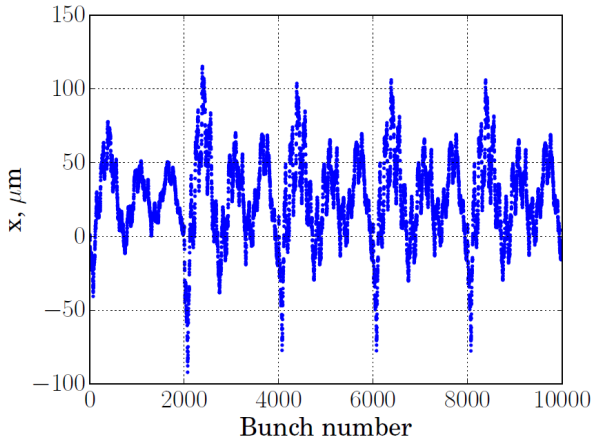

(c) Periodic 500 Hz HOM phase shift by 180°.

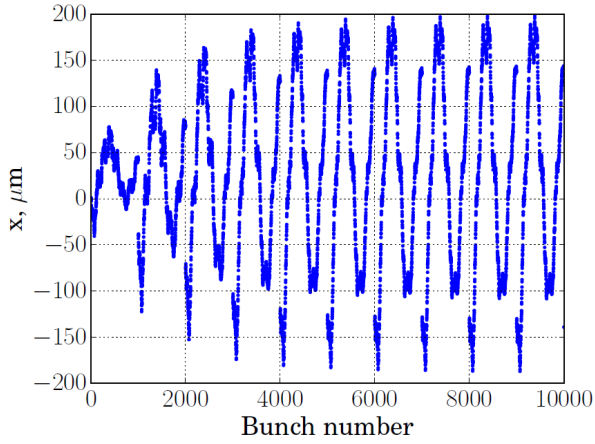

(d) Periodic 1 kHz HOM phase shift by 180°.

Figure 6.19: Transverse coordinate of electron bunches at the output of the linac.

500 Hz HOM phase shift and in Figure 6.19d for 1 kHz HOM phase shift. One can see that when the frequency of HOM phase shift is small enough, there is not correlation between transition effects from each shift and beam transverse coordinate variation does not accumulate (Figure 6.19c). When the frequency increases, variations from the shifts accumulate (Figure 6.19c), but after few periods transverse coordinate oscillation comes to a steady regime when amplitude does not change anymore.

It is found that BBU transition effect results is up to 200 μm bunch center position disturbance when HOM phase shift frequency is below 1 kHz. This value satisfies the requirements for LCLS-II beam dynamics.

CHAPTER 7

RESULTS AND CONCLUSION

The breakthrough discovery at Fermilab stated that SRF cavity fundamental mode quality factor can be significantly increased by nitrogen doping of the inside of the cavity walls after the standard treatment including high pressure water rinse, ethanol rinse, buffered chemical polishing, bulk electro-polishing for removal of about 120 μm of niobium using a standard solution of HF:H_2SO_4:HPO_3, and low temperature bake at 120°C for 48 hours. The result of the presented work allows to perform a controlled search for the optimal surface nitrogen concentration under the given constrains. To achieve this result a diffusion model of nitrogen gas into solid niobium was developed. This model was confirmed with secondary ion mass spectrometry (SIMS) measurements of nitrogen concentration profile in niobium samples undergone the same nitrogen doping treatment as actual SRF cavities. Certain doping procedure was determined to meet the model requirements, to be affordable and simple, and to be reproducible. All of the above allowed to search for the robust recipe to produce an SRF cavity with an optimal quality factor of the fundamental mode. Using the optimal recipe, a nine-cell cavity satisfies LCLS–II nominal requirement was produced. The reproducibility was demonstrated. The standard phase–lock procedure was used to determine the excitation curve of the cavity.

Low energy muon spin rotation (LE–μSR) measurements of magnetic field penetration into niobium samples undergone the standard SRF cavity treatment and nitrogen doping treatment allowed to measure microscopic parameters of superconductor such as electron mean free path and London magnetic field penetration depth λ_{L}. The value of λ_{L} measured for the niobium samples with the standard treatment, nitrogen doping and low temperature bake are in agreement with previously published results discovered using a different approach. There is no significant effect of nitrogen doping on magnetic field penetration depth λ_{L} found. There is no significant dependence of λ_{L} on magnetic field found.

In contrast, electron mean free path ℓ varies significantly for different treatments. The

value of ℓ for bulk niobium is about 400 nm. It was demonstrated that after low temperature bake ℓ drops down to about 2–16 nm. After the nitrogen doping of bulk niobium, electron mean free path is measured to be about 42 nm.

Magnetometer measurements with Physical Property Measurement System (PPMS) allowed to discover a nitrogen effect on critical magnetic fields of superconductor. It was demonstrated that upper critical magnetic field B_{c2} does not change after nitrogen doping compared to the other treatments. On the other hand, magnetic flux begins to penetrate inside the superconductor at lower external magnetic field values. This measurement explains the fact that SRF cavity undergone the nitrogen doping procedure has higher quality factor, but lower quench field.

The measurements of surface critical field B_{c3} for nitrogen samples treated with the standard procedure, low temperature bake and nitrogen doping demonstrated that nitrogen does not change microscopic parameters of the superconductor surface significantly. This is a confirmation of the result of LE-μSR measurement. The sample baked at 120° for 48 hours happened to have much higher value of B_{c3} among the considered samples. This also provides an improved microscopic understanding of the earlier observed effect of low temperature bake on high field Q-slope.

The effect of nitrogen doping on critical temperature of a niobium sample was measured. There is no effect on the value of critical temperature, but transition becomes wider after the doping. This result suggests the existence of the areas with suppressed critical temperature T_c inside the sample undergone nitrogen doping.

High order mode impact on beam dynamics in LCLS–II was analyzed. A conservative approach to estimate the upper limit of the effect was chosen. Both trapped and propagating HOMs were considered in the analysis, which makes it unique. Coherent (resonant) losses due to excitation of monopole HOMs were estimated. The value of losses depends on the HOM frequency value, which is random to some extension. The probability to cause significant losses was found to be negligible. Moreover, the technique to shift HOM frequency in case

of significant losses was found.

Cumulative effect caused by dipole HOMs excitation results in relative transverse emittance dilution. It was demonstrated that for the given specifications of dipole mode properties of SRF cavity, the emittance dilution is below 1% of original beam emittance. Transition effect of dipole HOMs was also analyzed. At given conditions on periodicity of HOM phase shift, the deviation of beam transverse coordinate from the orbit is found to be within 200 μm, which satisfies the specifications of LCLS–II.

CHAPTER 8

SUMMARY

The nitrogen diffusion into niobium is analyzed quantitatively. This leads to the introduction of the nitrogen-doping process that optimizes the quality factor for the fundamental mode. The robust, reproducible process is developed for the production of nine-cell superconducting radio frequency (SRF) cavities with an ultra-high qualify factor. In spite of achieved results, the increase of quality factor cannot be explained theoretically. Although there are a number of proposed models (references [11] and [43]), further studies of superconducting resonator physics are needed to identify a correct theoretical model.

The microscopic effects of nitrogen doping on superconducting properties of niobium are studied. These studies enable to explain the decrease of the quench field of SRF cavities after nitrogen doping. Measured microscopic parameters might be a part of future theoretical explanation of nitrogen doping effect, but it is obvious that the effect is also based on other parameters. Discovering the correlations between these parameters and nitrogen doping effect would help to complete a consistent theory in the future.

Both resonant and cumulative effects on the particle beam dynamics caused by the monopole and dipole high-order modes are found to be negligible for LCLS–II.

BIBLIOGRAPHY

[1] J. Bardeen, L. N. Cooper, and J. R. Schrieffer. *Physical Review*, 108:1175–1204, 1957.

[2] E. H. Brandt. Superconductors in realistic geometries: geometric edge barrier versus pinning. *Physica C*, 332:99, 2000.

[3] S. Casalbuoni, E. A. Knabbe, J. Kotzler, L. Lilje, L. von Sawilski, P. Schmuser, and B. Steffen. Surface superconductivity in niobium for superconducting RF cavities. *Nuclear Instruments and Methods in Physics Research A*, 538:45–64, 2005.

[4] The ILC Collaboration. *The International Linear Collider technical design report.* International Linear Collider, 2013.

[5] The LCLS Collaboration. *Linac Coherent Light Source (LCLS) conceptual design report.* SLAC National Accelerator Laboratory, Menlo Park, CA 94025, 2002.

[6] The LCLS-II Collaboration. *Linac Coherent Light Source II (LCLS–II) conceptual design report.* SLAC National Accelerator Laboratory, Menlo Park, CA 94025, 2011.

[7] R. B. Flippen. The radial velocity of magnetic field penetration in type ii superconductors. *Phys. Lett.*, 17(3), 1965.

[8] R. A. French. *Cryogenics*, 8:301, 1968.

[9] A. Grassellino. Performance of nitrogen doped cavities. In *Proceedings of International Particle Accelerator Conference 2015*. Richmond, Virginia, 2015.

[10] A. Grassellino, A. Romanenko, D. Sergatskov, O. Melnychuk, Y. Trenikhina, A. Crawford, A. Rowe, M. Wong, T. Khabiboulline, and F. Barkov. Nitrogen and argon doping of niobium for superconducting radio frequency cavities: a pathway to highly efficient accelerating structures. *Superconductor Science and Technology*, 26(10):102001, 2013.

[11] A. Gurevich. Reduction of dissipative nonlinear conductivity of superconductors by static and microwave magnetic fields. *Physics Review Letters*, 113:087001, 2014.

[12] T. Hays and H. Padamsee. Response of superconducting cavities to high peak power. In *Proceedings of the 1995 Particle Accelerator Conference and International Conference on High Energy Accelerators*, pages 1617–1619. Dallas, Texas, 1995.

[13] J. D. Jackson. *Classical Electrodynamics.* Wiley, New York, 1975.

[14] F. London and H. London. The electromagnetic equations of the supraconductor. *Proceedings of the Royal Society of London, Series A, Mathematical and Physical Sciences*, 149:71, 1935.

[15] J. Matricon and D. Saint-James. Superheating fields in superconductors. *Physics Letters*, 24 A:241–242, 1967.

[16] W. Meissner and R. Ochsenfeld. Ein neuer effekt bei eintritt der supraleitfähigkeit. *Die Naturwissenschaften*, 21:787, 1933.

[17] D. G. Myakishev and V. P. Yakovlev. An interactive code SUPERLANS for evaluation of RF–cavities and acceleration structures. In *Proceedings of IEEE Particle Accelerator Conference*, volume 5, pages 3002–3004. San Francisco, California, 1991.

[18] D. G. Myakishev and V. P. Yakovlev. The new possibilities of Superlans code for evaluation of axisymmetric cavities. In *Proceedings of 1995 Particle Accelerator Conference and International Conference on High-Energy Accelerators*, pages 2348–2350. Dallas, Texas, 1995.

[19] D. G. Myakishev and V. P. Yakovlev. CLANS2 — The code for evaluation of multipole modes in axisymmetric cavities with absorber ferrite. In *Proceedings of PAC99*, pages 2775–2776. New York, 1999.

[20] The official web site. CST — Computer Simulation Technology. `https://www.cst.com`.

[21] The official web site. European Organization for Nuclear Research (CERN). `http://home.web.cern.ch`.

[22] The official web site. European XFEL. `http://www.xfel.eu/en/`.

[23] The official web site. Fermi National Accelerator Laboratory. `http://www.fnal.gov`.

[24] The official web site. Large Hadron Collider. `http://home.web.cern.ch/topics/large-hadron-collider`.

[25] The official web site. SLAC National Accelerator Laboratory. `https://www6.slac.stanford.edu`.

[26] The official web site. Spallation Neutron Source. `http://neutrons.ornl.gov/sns`.

[27] The official web site. TESLA Technology Collaboration. `http://tesla-new.desy.de`.

[28] H. Padamsee. *RF Superconductivity: Volume II: Science, Technology and Applications*. Wiley-VCH Verlag GmbH and Co., KGaA, Weinheim, 2009.

[29] H. Padamsee, J. Knobloch, and T. Hays. *RF Superconductivity for Accelerators*. John Wiley and Sons, 1998.

[30] H. Piel. Superconducting cavities. In *S. Turner, editor, CERN Accelerator School: Superconductivity in Particle Accelerators*, pages 149–196. Hamburg, Germany, 1988.

[31] A. B. Pippard. An experimental and theoretical study of the relation between magnetic field and current in superconductor. *Proceedings of the Royal Society of London, Series A, Mathematical and Physical Sciences*, 216:547, 1953.

[32] S. Ramo and J. R. Whinnery. *Fields and Waves in Modern Radio*. Wiley and Sons, New York, 1959.

[33] A. Romanenko, A. Grassellino, F. Barkov, A. Suter, Z. Salman, and T. Prokscha. Strong meissner screening change in superconducting radio frequency cavities due to mild baking. *Applied Physics Letters*, 104(7):–, 2014.

[34] D. Saint-James and P. G. De Gennes. *Phys. Lett.*, 7:306–308, 1963.

[35] J. R. Schrieffer. *Theory of Superconductivity*. Addison–Wesley, San Francisco, CA, 1964.

[36] N. Solyak and V. Yakovlev. Assumptions about Q values in CW linac. Project X-doc-590-v1.

[37] A. Sukhanov, A. Vostrikov, T. Khabiboulline, A. Lunin, N. Solyak, and V. Yakovlev. Resonant excitation of high order modes in superconducting RF cavities of LCLS–II linac. LCLS-II TN-15-06.

[38] A. Suter, E. Morenzoni, N. Garifianov, R. Khasanov, E. Kirk, H. Luetkens, T. Prokscha, and M. Horisberger. Observation of nonexponential magnetic penetration profiles in the Meissner state: A manifestation of nonlocal effects in superconductors. *Physical Review B*, 72:024506, 2005.

[39] A. Suter, E. Morenzoni, R. Khasanov, H. Luetkens, T. Prokscha, and N. Garifianov. Direct observation of nonlocal effects in a superconductor. *Physical Review Letters*, 92:087001, 2004.

[40] M. Tinkham. *Introduction to Superconductivity*. Dover Publications, Inc., 1996.

[41] A. Vostrikov, A. Sukhanov, V. Yakovlev, and N. Solyak. Cumulative HOM excitation and transition effects in LCLS–II. *Physics Procedia*, 2015.

[42] A. Vostrikov, V. Yakovlev, N. Solyak, A. Lunin, A. Saini, T. Khabiboulline, and A. Sukhanov. High order modes in 650 MHz sections of the Project X linac. TD-11-008.

[43] B. P. Xiao, C. E. Reece, and M. J. Kelley. Superconducting surface impedance under radiofrequency field. *Physica C*, 490:26–31, 2013.